Measurement of $\sigma * BR(W + \gamma)$ and $\sigma * BR(Z + \gamma)$ in the Electron and Muon Channels in $\sqrt{s} = 1.8$ TeV $\bar{p}$-p Collisions

D. Benjamin[e], D. Errede[c], S. Errede[c], M. Lindgren[b], C. Luchini[c], T. Muller[b], D. Neuberger[b], M. Roach-Bellino[e], M. Shimojima[d], K. Sliwa[e], M. Timko[e], M. Vondracek[c], R.G. Wagner[a]

[a] *Argonne National Laboratory, Argonne, Illinois 60439*
[b] *University of California at Los Angeles, California 90024*
[c] *University of Illinois, Urbana, Illinois 61801*
[d] *University of Tsukuba, Tskukba, Ibaraki 305, Japan*
[e] *Tufts University, Medford, Massachusetts 02155*

May 14, 1993

Abstract

We have measured the cross sections $\times$ branching ratios for $W+\gamma$ and $Z+\gamma$ in the electron and muon channels using the inclusive e, μ W and Z data samples from the CDF '88-'89 collider run, with $4.05 \pm 0.28\ pb^{-1}$ ($3.54 \pm 0.24\ pb^{-1}$) electron (muon) data. For central photons with $E_T^\gamma > 5.0\ GeV$ and $\Delta R_{\ell\gamma} > 0.7$, we observe 8 (5) electron (muon) $W\gamma$ candidates and 2 (2) electron (muon) $Z\gamma$ candidates. From these events, we measure $\sigma * BR(W\gamma)$ and $\sigma * BR(Z\gamma)$ for the electron, muon and $e+\mu$ combined samples, and compare to the SM predictions:

$$\sigma * BR(W\gamma)_e = 17.0^{+13.8}_{-13.3}\ (stat+syst)\ pb \qquad \sigma * BR(W\gamma)_\mu = 19.4^{+19.2}_{-18.0}\ (stat+syst)\ pb$$
$$\sigma * BR(W\gamma)_{e+\mu} = 17.9^{+11.4}_{-10.7}\ (stat+syst)\ pb \qquad \sigma * BR(W\gamma)_{SM} = 19.0\ ^{+3.3}_{-0.9}\ (stat+syst)\ pb$$

$$\sigma * BR(Z\gamma)_e = 6.8\ ^{+5.9}_{-5.8}\ (stat+syst)\ pb \qquad \sigma * BR(Z\gamma)_\mu = 13.6^{+11.2}_{-10.1}\ (stat+syst)\ pb$$
$$\sigma * BR(Z\gamma)_{e+\mu} = 9.2\ ^{+5.6}_{-5.2}\ (stat+syst)\ pb \qquad \sigma * BR(Z\gamma)_{SM} = 4.7\ ^{+0.7}_{+0.2}\ (stat+syst)\ pb$$

We have also obtained three new results on cross section ratios, which for the combined $e+\mu$ results, along with the previous CDF measurement(s) of the W/Z cross section ratio provide new insight on the SM, and test possible anomalous couplings of the W and Z bosons:

$$\mathcal{R}(W\gamma/W)_{e+\mu} = 0.8^{+0.5}_{-0.5}\%\ (stat+syst) \qquad \mathcal{R}(Z\gamma/Z)_{e+\mu} = 4.3^{+2.5}_{-2.4}\%\ (stat+syst)$$
$$\mathcal{R}(W\gamma/Z\gamma)_{e+\mu} = 1.9^{+2.0}_{-1.4}\ (stat+syst) \qquad \mathcal{R}(W/Z)_{e+\mu} = 10.0^{+0.7}_{-0.7}\ (stat+syst)$$

From the $W\gamma$ and $Z\gamma$ cross section measurements, we obtain limits on anomalous $WW\gamma$ and $ZZ\gamma$ couplings of the W and Z bosons, providing constraints on possible internal (composite) structure for these gauge bosons. For $W\gamma$, from the combined $e+\mu$ result, we obtain limits on $WW\gamma$ anomalous coupling parameters $\Delta\kappa = \kappa - 1$ and λ of

$$\Delta\kappa = 0.0^{+5.4}_{-4.9}\ (stat+syst)\ \ (\lambda = 0) \qquad \lambda = 0.0^{+2.3}_{-2.4}\ (stat+syst)\ \ (\Delta\kappa = 0)$$

$$-6.6 < \Delta\kappa < +7.1\ \ (\lambda = 0,\ 95.0\%\ CL)$$
$$-3.2 < \lambda < +3.1\ \ (\Delta\kappa = 0,\ 95.0\%\ CL)$$

Since the $\Delta\kappa$ and λ parameters are related to the W boson magnetic dipole and electric quadrupole moments, and mean-squared charge radius by

$$\mu_W = \mu_W^\circ(2+\Delta\kappa+\lambda) \qquad Q_W = Q_W^\circ(1+\Delta\kappa-\lambda) \qquad < R_W >^2 = \lambda_W^2(1+\Delta\kappa+\lambda)$$

where λ_W is the (reduced) Compton wavelength of the W boson, we obtain limits on these additional electromagnetic properties of the W boson:

$$\mu_W/\mu_W^\circ \equiv g_W = 2.0^{+3.7}_{-3.6}\ (stat+syst)\ \ (Q_W/Q_W^\circ = 1)$$
$$Q_W/Q_W^\circ \equiv q_W = 1.0^{+5.6}_{-5.3}\ (stat+syst)\ \ (\mu_W/\mu_W^\circ = 2)$$
$$< R_W >^2/\lambda_W^2 \equiv r_W^2 = 1.0^{+3.7}_{-3.6}\ (stat+syst)\ \ (Q_W/Q_W^\circ = 1)$$

$$-4.8 < \mu_W/\mu_W^\circ - 2 \equiv g_W - 2 < +4.9\ \ (Q_W/Q_W^\circ = 1,\ 95.0\%\ CL)$$
$$-7.1 < Q_W/Q_W^\circ - 1 \equiv q_W - 1 < +7.4\ \ (\mu_W/\mu_W^\circ = 2,\ 95.0\%\ CL)$$
$$-4.8 < < R_W >^2/\lambda_W^2 - 1 \equiv r_W^2 - 1 < +4.9\ \ (Q_W/Q_W^\circ = 1,\ 95.0\%\ CL)$$

These results probe possible internal structure of the W boson at a distance scale of $\lambda_W \sim 2.5 \times 10^{-3}\ fm$, and are sensitive up to a compositeness scale $\Lambda \sim 1\ TeV$. For $Z\gamma$, from the combined $e+\mu$ result, we obtain limits on $ZZ\gamma$ anomalous coupling parameters h_{30}^Z and h_{40}^Z for three different choices of the compositeness scale Λ, with sensitivity to such anomalous couplings up to $\Lambda \sim 500\ GeV$. These results are also valid for anomalous $Z\gamma\gamma$ couplings.

1 Introduction

The Standard Model (SM) of electroweak interactions unifies the electromagnetic and weak interactions into a single interaction described by the gauge group $SU(2)_L \otimes U(1)_Y$. This theory predicts the existence of the $W^{\pm}$ vector bosons as carriers of the charged weak currents and two neutral vector bosons as carriers of the neutral currents, the γ and the Z^0. The measurement of W and Z production cross sections and decay properties in e.g. $\sqrt{s} = 1.8\ TeV$ $\bar{p}$-p collisions tests the strength and the nature of the couplings of gauge boson to matter fermions (quarks and leptons). The measurement of the $W^{\pm}\gamma$ and $Z^0\gamma$ di-boson production cross sections and final-state kinematics provides an experimental test of the predicted strength and nature of the trilinear gauge boson couplings between these particles and also simultaneously yields new information on static (transition) electromagnetic multipole moments of the W (Z) bosons[1, 2]. Additionally, composite models of W and Z bosons predict cross sections for $W\gamma$ and $Z\gamma$ production well above that for the Standard Model[3].

The nature of $W\gamma$ and $Z\gamma$ production is such that these processes are a sub-set of *inclusive* W and Z boson production. We therefore use the inclusive electron and muon W and Z data samples obtained from the CDF 1988-89 run as a starting point for this analysis. The inclusive W and Z data samples were used for extracting measurements of the inclusive W and Z cross sections in the electron and muon channels, and for measuring the W/Z cross section ratios. We use precisely the same trigger and event-selection criteria for electron and muon i.d., missing E_t ($\not\!\!E_T$) for defining the W and Z bosons in the $W\gamma$ and $Z\gamma$ event sub-samples as that used for the inclusive W and Z event samples, but *additionally* require the presence of an isolated, hard photon accompanying the W or Z boson in the event.

2 Theory of $W\gamma$ and $Z\gamma$ Production

The Feynman diagrams for $W\gamma$ and $Z\gamma$ production and decay are shown in figures 1 & 2. For $W\gamma$, the processes of interest are the trilinear gauge coupling diagrams, figs 1c & 1d. These diagrams are distinct only in the limit of a zero width W; the processes represented by figs 1a, 1b and 1e also produce events with a W and γ, though with different kinematics. The Feynman diagrams shown in figs 1a & 1b for the **u-** and **t-**channel processes are associated with initial-state radiation off of the incoming quark lines. The processes shown in fig 1c and 1e are known as radiative W decay (fig. 1e is the final state inner bremsstrahlung diagram). In the limit of a zero width W it is possible to distinquish these different processes by a measurement of the invariant mass of the $W\gamma$ system. However the W boson has a non-zero total width, $\Gamma_W = 2.1$ GeV, hence in the vicinity of the W mass, these processes are indistinguishable in the final state; their amplitudes must be added together coherently in order to produce a matrix element which preserves electromagnetic gauge invariance[4].

The most general effective Lagrangian[5] compatible with Lorentz and electromagnetic gauge invariance for the processes shown in Figs 1a-1e is

$$\begin{aligned}\mathcal{L}_{WW\gamma} &= -ie\Big[(W^{\dagger}_{\mu\nu}W^{\mu}A_{\nu} - W^{\dagger}_{\mu}A_{\nu}W^{\mu\nu}) \\ &\quad +\kappa W^{\dagger}_{\mu}W_{\nu}F^{\mu\nu} + \frac{\lambda}{M_W^2}W^{\dagger}_{\lambda\mu}W^{\mu}_{\nu}F^{\nu\lambda}\end{aligned}$$

$$+\kappa' W_\mu^\dagger W_\nu F'^{\mu\nu} + \frac{\lambda'}{M_W^2} W_{\lambda\mu}^\dagger W_\nu^\mu F'^{\nu\lambda}]$$

Where A^μ and W^μ are the photon and W^- fields, respectively, and $W_{\mu\nu} = \partial_\mu W_\nu - \partial_\nu W_\mu$, $F_{\mu\nu} = \partial_\mu A_\nu - \partial_\nu A_\mu$, $F'_{\mu\nu} = \frac{1}{2}\epsilon_{\mu\nu\rho\sigma} F^{\rho\sigma}$, e is the charge of the proton, and M_W is the W mass. The photon is taken to be on shell and both the virtual and on-shell W couple to essentially massless fermions allowing $\partial_\mu W^\mu = 0$. In the SM of electroweak interactions at the tree level $\kappa = 1$, $\lambda = 0$, $\kappa' = 0$, $\lambda' = 0$ are related to the classical parameters (with $\hbar = c = 1$)

$$\begin{aligned}
\mu_W &= \tfrac{e}{2M_W}(1+\kappa+\lambda) && \text{Magnetic Dipole Moment} \\
Q_W &= -\tfrac{e}{M_W^2}(\kappa-\lambda) && \text{Electric Quadrupole Moment} \\
d_W &= \tfrac{e}{2M_W}(\kappa'+\lambda') && \text{Electric Dipole Moment} \\
Q'_W &= -\tfrac{e}{M_W^2}(\kappa'-\lambda') && \text{Magnetic Quadrupole Moment} \\
< r >^2 &= \tfrac{1}{M_W^2}(\kappa+\lambda) && \text{Mean-Squared Charge Radius}
\end{aligned}$$

Note that for an arbitrary spin-S particle, $2S+1$ electromagnetic moments are allowed. Thus, the W vector boson is expected to have a magnetic dipole moment *and* an electric quadrupole moment in the Standard Model. The W electric dipole and magnetic quadrupole moments (the terms in the effective Lagrangian involving the κ' and λ' parameters) are $\mathcal{P}-$odd and violate $\mathcal{CP}$ (i.e. violate $\mathcal{T}$). Note also that the SM predictions for higher order corrections to κ, λ, etc, are expected to be of order α.

The $WW\gamma$ vertex function is given by[6]

$$\begin{aligned}
\Gamma^{\alpha\beta\mu}(q,\bar{q},P) &= f_1(q-\bar{q})^\mu g^{\alpha\beta} - \frac{f_2}{M_W^2}(q-\bar{q})^\mu P^\alpha P^\beta + f_3(P^\alpha g^{\mu\beta} - P^\beta g^{\mu\alpha}) \\
&\quad + i f_4(P^\alpha g^{\mu\beta} + P^\beta g^{\mu\alpha}) + i f_5 \epsilon^{\mu\alpha\beta\rho}(q-\bar{q})_\rho \\
&\quad - f_6 \epsilon^{\mu\alpha\beta\rho} P_\rho - \frac{f_7}{M_W^2}(q-\bar{q})^\mu \epsilon^{\alpha\beta\rho\sigma} P_\rho (q-\bar{q})_\sigma
\end{aligned}$$

Here, P and $\bar{q}$ are the four momenta of the incoming and outgoing W, and q is the four momentum of the final state photon. The seven form factors f_i are invariant and dimensionless functions of q^2, $\bar{q}^2$, and P^2. Their values at low energies are constrained by partial wave unitarity of the inelastic di-boson production amplitude in fermion antifermion annihilation at arbitrary center of mass energies[6] and for $W^\pm\gamma$ production are related to the parameters of the effective lagrangian by

$$\begin{aligned}
f_1 &= \mp\frac{1}{2}\left(1+\kappa+\frac{P^2}{M_W^2}\lambda\right) \\
f_2 &= \mp\lambda \\
f_3 &= -i f_4 = \mp\frac{1}{2}(1+\kappa+\lambda) \\
f_6 &= -i f_5 = \pm\frac{1}{2}(\kappa'+\lambda') \\
f_7 &= \pm\frac{1}{2}\lambda'
\end{aligned}$$

These momentum dependent form factors are of the generalized dipole form[4]:

$$a(P^2 = \hat{s},\ \bar{q}^2 = M_W^2,\ q^2 = 0) \ = \ \frac{a_0}{(1 + \hat{s}/\Lambda^2)^n}$$

where $a_0 \ = \ \Delta\kappa \ (= \kappa - 1)$, λ, κ', or λ'. The anomalous contributions to the $W\gamma$ helicity amplitudes grow like $\sqrt{\hat{s}}/M_W$ for κ, κ' and $\hat{s}/M_W^2$ for λ, λ'. The compositeness scale Λ represents the scale at which new physics becomes important in the weak boson sector, e.g. due to a composite structure of the W boson. The choice of the exponent $n = 2$ guarantees that unitarity is preserved. If the exponent is sufficiently above the minimum value of 1/2 (1), for κ, κ' (λ, λ') then one ensures that $W\gamma$ production is suppressed at energies $\sqrt{\hat{s}} >> \Lambda >> M_W$, where multiple weak boson or resonance phenomena are expected to dominate. The behavior of the form factors is such that they stay essentially constant for $\hat{s} << \Lambda^2$ and start to decrease only with the scale Λ is reached (or surpassed), in analogy to behavior associated with the well-known nucleon form factors.

Even though all the diagrams must be taken into account because of interference effects, in certain kinematic regions a subset of the diagrams provide most of the "interesting" signal. For the initial-state radiation processes, the radiation tends to be sharply peaked in angle along the incident quark/anti-quark directions. The vast majority of photons from the radiative W decay tend to be co-linear with the decay lepton. Both initial and final state radiation is sharply peaked at low energy, as is the radiation from $W\gamma$. However, the photons from $W\gamma$ production are not correlated with the lepton, and are not bounded by the mass of the W boson.

At large angles between the lepton and the photon the **u** and **t** channel diagrams cancel the **s** channel diagram, resulting in a "gauge zero" in the $W^{\pm}\gamma$ overall amplitude, and hence the $W\gamma$ cross section at $\cos\theta^* = \mp\frac{1}{3}$ [1] This gauge zero will be at least partially filled in by structure function effects, background processes, event mis-reconstruction, as well as by non-gauge theory values of κ, ($\kappa \neq 1$), λ, κ' and λ'[1]. Measurement of the depth of the dip in the cross section at $\cos\theta^* = \mp\frac{1}{3}$ and the shape of the $cos\theta^*$ distribution provides a sensitive measurement of the values of these parameters. Measurement of the $W\gamma$ cross section also constrains κ and λ, albeit in a less powerful manner.

For $Z\gamma$, since the Z boson is its own anti-particle (i.e. the Z, like the photon, is a Majorana particle) it cannot have any *static* electromagnetic multipole moments. Hence, the SM of electroweak interactions predicts no $ZZ\gamma$ (and also no $Z\gamma\gamma$) tri-linear gauge couplings at the tree-level. The Feynman diagrams for SM $Z\gamma$ production are shown in Figs. 2a, 2b and 2e, corresponding to initial state and final state radiation (inner bremsstrahlung). Non-SM Feynman diagrams for anomalous $Z\gamma$ couplings are shown in Figs. 2c and 2d. The SM initial and final-state radiation for $Z\gamma$ tends to produce photons sharply peaked in angles about the beam directions and the decay lepton directions, respectively.

Four different anomalous couplings are allowed by electromagnetic gauge invariance and Lorentz invariance. The most general anomalous $Z\gamma Z$ vertex function is given by[7]

$$\Gamma^{\alpha\beta\mu}_{Z\gamma Z}(q_1,\ q_2,\ P) \ = \ \left(\frac{P^2 - q_1^2}{M_Z^2}\right) \times$$

[1]The angle θ^* is defined as the angle between the photon and the incoming quark in the $W\gamma$ rest frame.

$$\left[h_1^Z\left(q_2^\mu g^{\alpha\beta}-q_2^\alpha g^{\mu\beta}\right)+\frac{h_2^Z}{M_Z^2}P^\alpha\left(P\cdot q_2 g^{\mu\beta}-q_2^\mu P^\beta\right)+h_3^Z\epsilon^{\mu\alpha\beta\rho}\,q_{2\rho}+\frac{h_4^Z}{M_Z^2}P^\alpha\epsilon^{\mu\beta\rho\sigma}P_\rho q_{2\sigma}\right]$$

where M_Z is the Z boson mass, P and q_1 are the incoming and outgoing Z boson four-momenta (Lorentz indicies μ and α respectively), and q_2 is the four-momentum of the outgoing (on-shell) photon (Lorentz index β). The most general $Z\gamma\gamma$ vertex function can be obtained from the $Z\gamma Z$ vertex function by replacing

$$\left(\frac{P^2-q_1^2}{M_Z^2}\right)\;\rightarrow\;\left(\frac{P^2}{M_Z^2}\right)\quad\text{and}\quad h_i^Z\;\rightarrow\;h_i^\gamma,\;\;i=1,...4$$

The overall $ZZ\gamma$ and $Z\gamma\gamma$ coupling strengths $g_{ZZ\gamma}$ and $g_{Z\gamma\gamma}$ are chosen to be e, where e is the proton charge. The overall factor of $P^2-q_1^2$ in the $Z\gamma Z$ vertex function is a consequence of Bose symmetry, whereas the factor of P^2 in the $Z\gamma\gamma$ vertex function is a consequence of electromagnetic gauge invariance; note that the $Z\gamma\gamma$ vertex function vanishes identically if both photons are on-shell.

The form factors h_i^Z and h_i^γ are dimensionless functions of q_1^2, q_2^2 and P^2. Similar to the form factors in the $WW\gamma$ vertex function, the values of h_i^Z and h_i^γ at low energies are constrained by S-matrix unitarity[5]. The $Z\gamma$ form factors h_i^V are of the form[5]:

$$h_i^V(P^2=\hat{s},\;q_1^2=M_Z^2,\;q_2^2=0)\;=\;\frac{h_{i0}^V}{(1+\hat{s}/\Lambda^2)^n}$$

The anomalous contributions to the $Z\gamma$ helicity amplitudes grow like $(\sqrt{\hat{s}}/M_Z)^3$ for $h_{1,3}^V$ and $(\sqrt{\hat{s}}/M_Z)^5$ for $h_{2,4}^V$. We shall assume that $n=3$ for $h_{1,3}^V$ and $n=4$ for $h_{2,4}^V$. These choices guarantee that unitarity is preserved and that terms proportional to $h_{20,40}^V$ have the same high energy behavior as those proportional to $h_{10,30}^V$. If these exponents are sufficiently above their minimum values of 3/2 and 5/2 for $h_{1,3}^V$ and $n=4$ for $h_{2,4}^V$, respectively then one ensures that $Z\gamma$ production is suppressed at energies $\sqrt{\hat{s}}>>\Lambda>>M_Z$, where multiple weak boson or resonance phenomena are expected to dominate.

Note that all couplings are $\mathcal{C}-$odd; h_{10}^V and h_{20}^V ($V=Z,\;\gamma$) violate $\mathcal{CP}$ (i.e. violate $\mathcal{T}$). Combinations of h_{30}^V and h_{40}^V correspond to the electric dipole and magnetic quadrupole transition moments for the $Z\gamma Z$ or $Z\gamma\gamma$ processes, whereas combinations of h_{10}^V and h_{20}^V correspond to the magnetic dipole and electric quadrupole transition moments for these processes. Within the context of the Standard Model, at the tree-level, all couplings h_i^V vanish. However, at the one-loop level, only the $\mathcal{CP}-$conserving couplings h_3^V and h_4^V are non-zero, but again, like the one-loop SM corrections to the κ and λ parameters for $W\gamma$, the higher- order SM contributions to $Z\gamma$ are also expected to be quite small, e.g. $h_{30}^Z\;\sim\;2\times10^{-4}$[8]. Large anomalous contributions to the κ and λ parameters for $W\gamma$, and e.g. h_{30}^Z and h_{40}^Z for $Z\gamma$ are possible if the W and Z bosons are composite objects, in analogy to e.g. the anomalous contributions to the magnetic dipole moments of the proton and neutron, where $\kappa_p\;=\;+1.79$ and $\kappa_n\;=\;-1.91$ due to the quark substructure of the nucleon.

As mentioned before, non-standard $WW\gamma$, $ZZ\gamma$ and $Z\gamma\gamma$ couplings are momentum dependent form factors which must vanish at large momentum transfer to guarantee that S-matrix unitarity is not violated[9]. Sensitivity limits for the anomalous couplings extracted from experimental data will thus depend on the the form factor scale Λ which characterizes the energy above which the form factor starts to decrease. Λ is generally assumed to be connected to some novel interactions operative at energies $\approx\Lambda$, and is expected to be at

least of order of a few hundred GeV. For $\bar{p}p$ interactions at 1.8 TeV, the dependence of the sensitivity limits on the scale Λ is rather mild for the $WW\gamma$ couplings. It is much stronger for h_i^Z and h_i^γ.

Because of the destructive interference between the diagram involving the $WW\gamma$ vertex and the **u** and **t** channel graphs for the SM $W\gamma$ process which results in the "gauge zero" and is not present for the SM $Z\gamma$ process, the SM $W\gamma$ and $Z\gamma$ cross section $\times$ branching ratios are predicted to be roughly comparable to each other ($\sim 20\ pb$ and $\sim\ 5\ pb$ respectively, for events passing the $P_T^\gamma > 5.0\ GeV$ and $\Delta R_{\ell-\gamma} > 0.7$ cuts), in contrast to the inclusive W and Z cross section $\times$ branching ratios of $\sim\ 2.2\ nb$ and $\sim\ 0.2\ nb$, respectively. Note also that for non-SM values of e.g. κ and λ, etc. or the h_i^V parameters, the $W\gamma$ and $Z\gamma$ cross sections vary quadratically with these parameters. Note further that due to interference effects and the different $\hat{s}-$dependencies of the various terms in the overall invariant amplitude $\mathcal{M}$, the minimum of the $W\gamma$ cross section does not occur at the SM values of κ and λ. This is also true for the $Z\gamma$ case.

3 Experimental Apparatus

The Tevatron $\bar{p}$-p collider at Fermilab operated at a center of mass energy of 1.8 TeV and a nominal luminosity of $10^{30}\text{cm}^{-2}\text{sec}^{-1}$ during the 1988-89 run. The CDF detector at the Tevatron is a multi-component detector that covers most of 4π solid angle. A perspective view of the CDF detector with coordinate axes indicated is shown in Figure 3, and a cut away view is shown in Figure 4.

The components of the CDF detector of most interest for this analysis are the beam-beam counters, the central tracking system, the central, plug and forward calorimetry, and the central muon system. The beam-beam counters (BBC) are a plane of counters located immediately in front of the forward/backward calorimeters, providing a minimum-bias trigger for the detector, and are also used as the primary luminosity monitor for CDF. The min-bias trigger requires at least one counter in each plane to fire within a 15 ns window centered on the beam crossing time.

The CDF central tracking system is composed of a vertex time projection chamber (VTPC) located immediately outside the beam pipe, a large volume central tracking chamber (CTC) contained within a 1.42 Tesla magnetic field. The VTPC is used to establish the position of the interaction vertex and to provide tracking information in the region $|\eta| \leq 3.5$[2]. The central tracking chamber encloses the VTPC and gives precise track momentum and charge-sign measurements in the region $|\eta| < 1.1$.

The calorimeters have fine segmentation in eta-phi and are organized into projective towers pointing towards the interaction region. The calorimeters cover all of phi, and extend to $|\eta| < 4.2$. Each calorimeter tower consists of an electromagnetic shower counter in front of a hadronic calorimeter element. In the central region ($|\eta| < 1.1$) the calorimeters are scintillator-based, while the plug and forward calorimeters are gas-based, using proportional tubes and cathode pad readouts. The calorimeters are used to identify electrons by energy deposition of an incident track nearly entirely in the EM portion of the calorimeter, and to augment muon identification by detection of their minimum ionizing energy deposition signature in the calorimeter, and also to identify photons by energy deposition in the EM

[2] η is defined by $\eta = -ln(\tan(\theta/2))$

portion of the calorimeter where no track is incident.

The central electromagnetic strip chambers (CES) are used to determine shower position and traverse development of an electromagnetic shower at shower maximum by measurement of the charge deposition on orthogonal strips and wires. In this analysis the strip information is used to separate single photons from the multiple photon background, as well as provide a precise z and ϕ position of the EM calorimeter cluster. Figure 5 is a schematic of the the material between the coil of the solenoid and the CES. Figure 6 shows the orientation of the cathode strips and anode wires in the CES.

The central muon chambers (CMU) consist of drift chambers modules located behind approximately 5 absorption lengths of lead and steel in the central calorimeters. The end view of the CMU chambers is shown in Figure 7 and the CMU chambers position within a wedge is shown in Figure 8. Each CMU wedge on either side of $\eta = 0$ cover the region $0.026 < |\eta| < 0.63$ and 15^0 in phi.

The inclusive electron W and Z data sets that are searched for the $(W \rightarrow e\nu_e) + \gamma$ and $(Z \rightarrow e^+e^-) + \gamma$ events were obtained with the inclusive central electron trigger, which is formed whenever a central EM cluster with $E_T > 12$ GeV is matched to a track with transverse momentum of $P_T > 9$ GeV/c, as found by the hardware track processor [10].

The inclusive muon W and Z data sets that are searched for the $(W \rightarrow \mu\nu_\mu) + \gamma$ and $(Z \rightarrow \mu^+\mu^-) + \gamma$ events were obtained with the inclusive central muon trigger, which is formed whenever prompt hits in the central muon chambers are matched to a track with transverse momentum of $P_T > 9$ GeV/c, as found by the hardware track processor [10].

4 The Inclusive e and μ W and Z Data Samples

The starting point for the $W\gamma$ and $Z\gamma$ analysis in the electron and muon channels is from the inclusive electron and muon W and Z data samples that were used for the electron and muon W and Z absolute cross section $\times$ branching ratio measurements and the electron and muon W/Z cross section ratios [11].

In the 1988-89 Tevatron collider run, CDF collected $\int \mathcal{L}_e dt = 4.05 \pm 0.28$ pb^{-1} of high P_t electron data and $\int \mathcal{L}_\mu dt = 3.54 \pm 0.24$ pb^{-1} of high P_t muon data[12]. The uncertainty in each of these integrated luminosities is 6.8%, due primarily to the uncertainty associated with that part of the total inelastic $\bar{p}$-p cross section observed by the Beam-Beam Counters (BBC), $\sigma_{BBC} = 46.8 \pm 3.2\ mb$

The electron W and Z samples were obtained from a common central electron sample (with common selection efficiencies and backgrounds), requiring that the candidate central electron cluster have the following properties:

- The event vertex be within $|Z_{\rm vertex}| < 60.0\ cm$ of nominal $Z = 0.0$ position.
- The electron cluster have $|\eta| < 1.1$, and be within the good fiducial region of the CEM calorimeter.
- A transverse energy of the central EM cluster of $E_T > 20.0\ GeV$
- Isolation $I \equiv (E_T^{\rm cone} - E_T^{\rm cluster})/E_T^{\rm cluster} < 0.1$, in an angular cone of size $\Delta R = \sqrt{\Delta\eta^2 + \Delta\phi^2} = 0.4$ centered on the EM cluster (location defined from CES shower centroid information).

- Had/EM $<$ 0.055 + 0.00045 * E, where E is the total energy of the EM cluster in GeV
- Using 11 channel clustering, the CES strip chi-square of a fit of test-beam electron shower profiles to the leading cluster profile in the strip view must each be $\chi^2_{\rm strip} < 15.0$
- Lateral shower-shape variable $L_{\rm shr} < 0.2$, which compares the observed lateral shower profile to test-beam electron lateral shower profile data.
- A single reconstructed 3-dimensional track associated with the EM cluster with $E/P < 1.5$ which matches to the CES position to within $|\Delta Z| < 3.0\ cm$ and $|\Delta r - \phi| < 1.5\ cm$

A total of 5012 events pass these requirements.

Electron W candidates are obtained from the common central electron sample by additionally requiring $\not\!\!E_T > 20\ GeV$. The W candidates must not be simultaneously consistent with being an electron Z candidate, as defined below. A total of 2664 events pass the electron W requirements.

Electron Z candidates are obtained from the common central electron sample by additionally requiring a second electromagnetic cluster located in a good fiducial region of either the central, plug or forward calorimeters, passing the following selection criteria:

- A transverse energy of the second cluster of $E_T > 10.0\ GeV$
- Isolation $I \equiv (E_T^{\rm cone} - E_T^{\rm cluster})/E_T^{\rm cluster} < 0.1$, in an angular cone of size $\Delta R = \sqrt{\Delta\eta^2 + \Delta\phi^2} = 0.4$ centered on the EM cluster (location defined from shower centroid information).
- Had/EM $<$ 0.10
- In the central region, a second EM cluster is required to have a 3-dimensional track associated with it, and $E/P < 2.0$
- In the plug region, a second EM cluster is required to have a 3×3 $\chi^2 < 20.0$ and a VTPC hit fraction Occ > 0.5 in a road centered on the PEM cluster.
- The dielectron pair mass lies between $70 < M_{ee} < 110\ GeV/c^2$

A total of 243 events pass the electron Z requirements.

The muon W and Z samples were obtained from a common central muon sample (with common selection efficiencies and backgrounds), requiring that the candidate central muon have the following properties:

- The event vertex be within $|Z_{\rm vertex}| < 60.0\ cm$ of nominal $Z = 0.0$
- A reconstructed central muon with a $P_t \geq 20\ GeV/c$, and in a good fiducial region of the central muon system.

- A match of the extrapolated CTC track to the reconstructed muon "stub" in the muon chambers to better than 2cm in the $r - \phi$ plane
- Less than 6 GeV of hadronic energy deposited in the calorimeter, and less than 2 of electromagnetic energy deposited in the calorimeter in the calorimeter towers traversed by the muon.
- Isolation $I \equiv (\Sigma_{0.4} E_t - E_t^\mu)/P_t^\mu \leq 0.10$, where E_t^μ is the transverse energy deposited in the calorimeter towers traversed by the muon, P_t^μ is the transverse momentum of the muon track, and $\Sigma_{0.4}$ is the sum of the transverse energy in a cone of $\Delta R \leq 0.4$ centered on the muon track.
- Cosmic rays were removed from the sample by using the central tracking chamber information to veto those events that were inconsistent with tracks coming from the event vertex.[13]

A total of 2011 events pass these requirements.

Muon W candidates are obtained from the common central muon sample by additionally requiring $\not\!\!E_T > 20\ GeV$. The W candidates must not be simultaneously consistent with being an muon Z candidate, as defined below. A total of 1436 events pass the muon W requirements.

Muon Z candidates are obtained from the common central muon sample by additionally requiring a second minimum ionizing track passing the following selection criteria:

- $|\eta| < 1.0$
- $P_t \geq 20\ GeV/c$
- Opposite charge sign to the first muon.
- The dimuon pair mass lies between $65 < M_{\mu\mu} < 115\ GeV/c^2$

A total of 106 events pass the muon Z requirements.

A common photon event selection was then additionally applied to each of these four inclusive data samples, to obtain the electron and muon $W\gamma$ and $Z\gamma$ sub-datasets. However, before proceding with making any photon cuts on the data samples, we re-clustered *all* data files with lower seed and sum E_T thresholds of $Seed = 1.0\ GeV$, $Sum = 1.5\ GeV$ in the EMCLST filter. Position-dependent energy response-map and energy scale corrections were applied to the data, the E_T of the cluster was calculated from the event vertex and *then* a cut of $E_T^{\rm ELES} > 5\ GeV$ was applied to the data. The default ELES clustering (of $Seed = 3.0\ GeV$, $Sum = 5.0\ GeV$) is inefficient at threshold, partially because of the fact that seed and sum are calculated with the *raw* energies, and also because E_T of the seed and sum are calculated from $z = 0$, rather than the actual event vertex. We studied the threshold effects using QFL MC-simulated photons, generated flat in energy from $0.5 < E_T < 12.5\ GeV$ in the central, plug and forward calorimeters, comparing results obtained with the default clustering, vs. that obtained with $Seed = 1.0\ GeV$, $Sum = 1.5\ GeV$. The default clustering efficiency for the CEM, PEM and FEM is shown in Figs. 9a-9b. It can be seen that based on this MC study, the default clustering for the CEM/PEM/FEM is not fully efficient until $E_T \sim 6.0/9.0/8.0\ GeV$ respectively.

For each of the four data sets, a photon candidate was comm[illegible] defined as

- A 1-3 tower cluster of electromagnetic energy deposited in the central calorimeter of at least $E_t \geq 5\ GeV$, after position response and CEM energy scale corrections, with a seed calorimeter tower energy of at least $E_t \geq 1\ GeV$

- The location of the CEM cluster was required to be in a good fiducial region of the central calorimeter, as defined by the position determined from CES shower centroid information.

- The distance between the W/Z decay lepton(s) and the photon, $\Delta R_{\ell\gamma}$, must be greater than 0.7. This cut is designed to suppress the contribution of the radiative decay diagrams to the signal. $\Delta R_{\ell\gamma} = 0.7$ corresponds to e.g. an opening angle of $\sim 40^o$ in the $r - \phi$ plane.

- The extra transverse energy deposited in a cone of $\Delta R = 0.4$ centered on the CEM cluster, but not including the EM cluster must be less than $ET4 < 2.0\ GeV$ and $ET4 < 1.0\ GeV$ (two distinct cuts).

- The extra summed transverse momentum due to charged tracks within a cone of $\Delta R = 0.4$ centered on the CEM cluster must be less than $\sum PT4 < 2.0\ GeV$ and $\sum PT4 < 1.0\ GeV$ (two distinct cuts). The tracks participating in the sum must have $|Z_{vtx} - Z_0| < 10\ cm$.

- No 3-D CTC tracks (originating from *any* vertex) pointing at the EM cluster (N3D=0).

- $Had/EM < 0.055 + 0.00045 * E$ where E is the total energy of the EM cluster in GeV.

- A lateral shower-shape for the CEM cluster of $L_{shr} < 0.5$

- Using 11 channel clustering, the CES strip and wire chi-squares of a fit of the testbeam electron shower profiles to the leading cluster profile in each of these views, must each be less than 20.0

- A cut of no 2^{nd} CES strip/wire clusters with $E_{CES\ 2^{nd}} > 1\ GeV$ (within the CEM cluster) was made to further suppress π^0 and multi-photon backgrounds.

5 Determination of Photon Efficiencies

The overall efficiency for CEM photons was determined from the product of efficiencies associated with the above-described CEM photon cuts. We determined the efficiency for the calorimeter isolation in a cone of $\Delta R = 0.4$ ($ET4$) in the central calorimeter ($|\eta| < 1.1$) for $ET4 < 2.0\ GeV$ and $ET4 < 1.0\ GeV$ from random cones in the inclusive W/Z data samples, where the cone of $\Delta R = 0.4$ was required to be more than $\Delta R = 0.7$ away from the W/Z decay lepton(s) We also determined the efficiency for the $ET4 < 2.0\ GeV$ and $ET4 < 1.0\ GeV$ calorimeter isolation cuts from random cones in Minimum Bias and Jet-20

data sample, where in this latter sample, random cones of $\Delta R = 0.4$ were thrown in Jet-20 events satisfying the following criteria:

- $|Z_{\rm vertex}| < 60\ cm$
- $\not\!\!E_T < 20.0\ GeV$, $\not\!\!E_T$ significance, $\sigma_{\not\!\!E_T} < 2.4$. These cuts were imposed for quality-control in Jet-20 events - suppressing badly mis-measured and/or junk events.
- At least three jets in a Jet-20 event
- QDJSCO-corrected jets.
- For the two leading jets (highest E_T) (after QDJSCO-corrections applied), require that at least one of the two leading jets be in the central ($|\eta_{\rm det}| < 1.1$) region of the detector, the other central or plug ($|\eta_{\rm det}| < 2.4$).
- For the two leading jets, require that each QDJSCO-corrected jet have $E_T^J > 15.0\ GeV$ and that $M_{JJ} > 40.0\ GeV/c^2$.

Two studies with random cones thrown in the Jet-20 data sample were done. In the first study (Jet-20a), random cones of $\Delta R = 0.4$ thrown in Jet-20 events passing the above criteria were required to be more than $\Delta R = 1.4$ away from *all* jets in the event, in order to stay clear of the default $\Delta R = 0.7$ jet-cone clustering radius in JETCLU. In the second study (Jet-20b), random cones of $\Delta R = 0.4$ thrown in Jet-20 events passing the above criteria were required to be more than $\Delta R = 1.4$ away from the two leading (i.e. trigger) jets in the event. The $ET4$ calorimeter isolation efficiencies for $ET4 < 2.0\ GeV$ and $ET4 < 1.0\ GeV$ were also determined from QFL Baur electron and muon $W\gamma$ and $Z\gamma$ MC simulated events, where the underlying event was simulated with the use of the ISAJET MC. The CEM photons in the QFL Baur MC data were required to be more than $\Delta R = 0.7$ away from the W/Z decay lepton(s).

The efficienc(ies) for the summed P_t in a cone of $\Delta R = 0.4$, ($\sum PT4$) downstream of the $ET4$ cut(s) for CEM photons were also determined from these same data samples. The efficiency for the "No 3D CTC Track" pointing at the CEM cluster (N3D=0) was also determined from these same data samples.

The efficiencies for $Had/EM < 0.055 + 0.00045 * E$, $L_{shr} < 0.5$, $\chi^2_{\rm strip} < 20.0$ and $\chi^2_{\rm wire} < 20.0$ and the no 2^{nd} CES strip/wire cluster $E_{CES\ 2^{nd}} > 1\ GeV$ cuts were determined from $5-50\ GeV$ CEM electron test beam data and also from the QFL Baur electron/muon $W\gamma\ /Z\gamma$ MC simulated data.

The efficiencies for these photon cuts for CEM photons, and the overall CEM photon efficiency, are summarized in Tables Ia-Ic. It can be seen that the photon efficiencies obtained from random cones thrown in the electron and muon inclusive W/Z data samples are in good agreement with one another. The results obtained from random cones thrown in the Minimum Bias data have systematically somewhat higher photon efficiency than that obtained from the inclusive W/Z data samples, as anticipated. The results from the Jet-20a random cone study (central cones thrown avoiding all jets in Jet-20 events) are systematically higher in efficiency by approximately 5% than that for the inclusive W/Z data samples. The results from the Jet-20b random cone study (central cones thrown avoiding only the two

leading/trigger jets) are systematically lower in efficiency by approximately 5% than that for the inclusive W_e or W_μ data samples.

The QFL $W\gamma$ MC efficiencies associated with the $\sum PT4$ cut(s) are systematically higher than e.g. the inclusive W/Z results. The ISAJET underlying event in the QFL MC simulation appears to be slightly less "noisy", in terms of charged particle multiplicities and e.g. track P_T spectra than that associated with the inclusive W/Z data samples. Note further that the QFL Had/EM efficiency is somewhat low, due to a (significant) disagreement between the e.g. QFL Had/EM distribution for low-energy $W\gamma$ /$Z\gamma$ MC photons (or simply QFL MC single photons) compared to the Had/EM distribution observed from electron test-beam data, and/or inclusive low-P_T electron data, gamma conversion pair data, etc.

Figures 10a-10d show the progression of cuts for the electron $W\gamma$ data sample. Figures 11a-11d show the progression of cuts for the Jet-20 QCD background data sample.

6 MC Determination of e and μ $W\gamma$ and $Z\gamma$ Signal

The Standard Model predictions for the number of expected electron and muon $W\gamma$ and $Z\gamma$ events for integrated luminosities of $\int \mathcal{L}_e dt = 4.05 \pm 0.28$ pb^{-1} for electrons and $\int \mathcal{L}_\mu dt = 3.54 \pm 0.24$ pb^{-1} for muons were obtained using two quasi-independent Monte Carlo methods. Both methods used the Baur $W\gamma$ and $Z\gamma$ Monte Carlo programs for generation of electron, muon and tau $W\gamma$ and $Z\gamma$ MC data samples[5]. The tau data samples were generated for determination of e.g. $W \rightarrow \tau \rightarrow e/\mu$ and $Z \rightarrow \tau^+\tau^- \rightarrow e/\mu$ backgrounds in the electron and muon $W\gamma$ and $Z\gamma$ samples. The Baur $W\gamma$ and $Z\gamma$ MC programs generate weighted events using the helicity-amplitude formalism, adding together the contributions of the Feynman graphs of figures 1 and 2, respectively. The kinematic phase space is done using the VEGAS adaptive multi-dimensional integration code[14]. The Baur $W\gamma$ and $Z\gamma$ MC programs were modified to use the (latest version) of the CERN PDFLIB structure functions (V3.10) [15], and include *all* parton-parton luminosities (and CKM matrix elements, for $W\gamma$). The cross section output from the Baur MC programs includes a $K-$factor of $1 + \frac{8\pi}{9}\alpha_s(M_V^2) \simeq 1.35$.

In the first method, large samples ($> 500K$ events each) of electron and muon $W\gamma$ and $Z\gamma$ Baur MC events were generated with as few kinematic cuts as possible, in order to obtain as much of the "total" $W\gamma$ and $Z\gamma$ cross sections, and in an effort to minimize potential biasing of results from "feed-down" effects due to finite detector resolution and smearing effects. The kinematic cuts used at the Baur MC event generator level for $W\gamma$ were no lepton P_T^ℓ or $\not\!\!E_T$ cut, $P_T^\gamma > 1.0\ GeV$, $\Delta R_{\ell-\gamma} > 0.3$, no lepton/neutrino pseudo-rapidity cuts, and $|\eta_\gamma| < 6.0$. For $Z\gamma$, the cuts used at the event generator level were lepton $P_T^\ell > 1.0\ GeV$, $P_T^\gamma > 1.0\ GeV$, $\Delta R_{\ell-\gamma} > 0.3$, lepton $|\eta_\ell| < 6.0$ and $|\eta_\gamma| < 6.0$. Four-vector information from the events passing these cuts generated with the Baur $W\gamma$ and/or $Z\gamma$ MC were written to unformatted files. We have studied the systematics of these MC results using many different structure-function choices, P_T- and Q^2-scale dependence (see below); the results presented in this note are nominally be based on the use of HMRS-B structure functions, i.e. the same structure functions for which the CDF electron and muon W and Z cross sections and electron and muon W/Z cross section ratio results were based upon, as a "nominal" structure function choice.

Two independent (and very detailed) "fast" $W\gamma$ /$Z\gamma$ MC detector simulation programs were developed, which were structured along lines similar to that of the "fast" W/Z MC

detector simulation programs that were used for the electron and muon W and Z cross sections and W/Z cross section ratio analyses[16]. The two versions of each program were extremely useful for cross-checking each other, especiallly in the early development stages of these programs.

The purpose(s) of the fast $W\gamma$ and $Z\gamma$ Monte Carlo detector simulation programs were to a.) determine geometric and kinematic acceptances, b.) obtain predicted cross sections for $W\gamma$ and $Z\gamma$, above the W and Z boson event selection cuts and above the $\Delta R_{\ell-\gamma} > 0.7$ and $E_T^\gamma > 5.0\ GeV$ photons cuts, and c.) to obtain predictions for the expected # of $W\gamma$ and $Z\gamma$ events in the CDF electron and muon $W\gamma$ and $Z\gamma$ data samples, inputting all relevant electron, muon and photon *efficiencies*. Since we are using precisely the same cuts for W and Z selection as was used in the determination of the inclusive electron and muon W and Z $\sigma * BR$ cross sections and W/Z cross section ratio analyses, we use all of the electron and muon efficiencies as determined by the inclusive W and Z analyses in the $W\gamma$ and $Z\gamma$ analyses. Our main task is therefore to determine CEM/PEM photon efficiencies and the geometric and kinematic acceptances relevant to each of our data samples.

The fast $W\gamma$ and $Z\gamma$ MC detector simulation programs read in the unformatted e or μ data files output from the Baur $W\gamma$ and $Z\gamma$ MC event generator programs, and then push each event through a fast (i.e. parametrized) detector simulation. Each Baur $W\gamma$ or $Z\gamma$ MC event is given a random P_T boost, according to use of a "nominal" P_T distribution, based on CDF measurements of the W and Z boson P_T distributions[17]. The $Z-$vertex for the event is obtained from a gaussian distribution, of $\sigma_Z = 30\ cm$. Electron and photon energies are smeared by the appropriate detector resolution for e.g. CEM, PEM, FEM, muon P_T's are smeared by (non-beam constrained) CTC track momentum resolution. For the W in $W\gamma$ events, the $\not\!\!E_T$ is smeared in the same way as was done in the fast W and Z Monte Carlo detector simulations, i.e. precisely the same way as was done in the electron and muon W mass analyses[18]. The jet recoiling from the $W\gamma$ P_T is degraded and smeared by a jet resolution parametrization; the contribution to the $\not\!\!E_T$ from the underlying event is kicked in x and y according to a random sampling of the scalar E_T distribution for inclusive W/Z events; the overall $\not\!\!E_T$ is computed from combined smeared electron E_T or muon P_T, smeared photon E_T, the degraded and smeared recoil jet and the underlying event.

The smeared electrons, muons and photons from Baur $W\gamma$ and $Z\gamma$ MC events are propagated from the event vertex through the solenoidal field to the calorimeter, muons are further propagated outwards to the muon chambers in the return field. Standard subroutines - a modified (standalone) version of FIDELE and FIDCMU are used for determining the fiduciality of electrons, photons and muons, respectively.

The $W\gamma$ and $Z\gamma$ cross sections above cuts, geometric and kinematic acceptances and the predicted # of CEM/PEM electron and muon $W\gamma$ and $Z\gamma$ events are determined using weighted events, following the procedure described in CDF-1732[19]. Typically $\sim 50K$ events pass all event selection cuts after detector simulation. Uncertainties on all derived quantities are obtained from (internal) use of the CONFIDENCE subroutine and/or additional (post-processor) MC simulation of numerical results and their uncertainties.

The experimental measurement of the $(W \to \ell\nu_\ell) + \gamma$ and $(Z \to \ell^+\ell^-) + \gamma$ cross sections is given by

$$\sigma_W \cdot B(W \to \ell\nu_\ell\gamma) = \frac{\mathcal{N}^{W\gamma}_{observed} - \sum \mathcal{N}^{W\gamma}_{background}}{A_{W\gamma} \cdot \epsilon_{W\gamma} \cdot \int \mathcal{L}_\ell dt}$$

$$\sigma_Z \cdot B(Z \to \ell^+\ell^-\gamma) = \frac{\mathcal{N}^{Z\gamma}_{observed} - \sum \mathcal{N}^{Z\gamma}_{background}}{A_{Z\gamma} \cdot \epsilon_{Z\gamma} \cdot \int \mathcal{L}_\ell dt}$$

where $\mathcal{N}^{W\gamma}_{observed}$ and $\mathcal{N}^{Z\gamma}_{observed}$ are the number of observed $W\gamma$ and $Z\gamma$ events in a particular decay channel (e or μ); $\sum \mathcal{N}^{W\gamma}_{background}$ and $\sum \mathcal{N}^{Z\gamma}_{background}$ are the number of (summed) background events expected in each of the data samples. The product terms $A_{W\gamma} \cdot \epsilon_{W\gamma}$ and $A_{Z\gamma} \cdot \epsilon_{Z\gamma}$ are the (overall) acceptance $\times$ efficiency factors for detecting the $W\gamma$ and $Z\gamma$ events, respectively. The integrated luminosity ($\int \mathcal{L}_\ell dt$) in the denominator then normalizes the number of events to our particular data samples.

The product acceptance $\times$ efficiency terms are in fact products of a number of acceptances $\times$ efficiencies:

$$A_{W\gamma} \cdot \epsilon_{W\gamma} = A_W \cdot A^{\gamma}_{\rm geom} \cdot \epsilon_{\rm lepton} \cdot \epsilon_{\rm photon} \cdot \epsilon_{\rm trigger} \cdot \epsilon_{\rm Analysis\ cuts}$$

The acceptance A_W is the combined muon fiducial, muon & $\not\!\!E_T$ kinematic acceptance for the W boson; the acceptance $A^{\gamma}_{\rm geom}$ is the combined geometric and kinematic acceptance of the photon to pass through e.g. the CEM calorimeter. The ϵ terms are (product) efficiencies for detecting e.g. the lepton or the photon once they have passed through their respective detectors. The term $\epsilon_{\rm lepton}$ is the efficiency for the CEM (CMU) system to record the electron (muon) in the event, whereas $\epsilon_{\rm photon}$ is the efficiency for the calorimeters to record the passage of the photon. The term $\epsilon_{\rm trigger}$ is the lepton trigger efficiency. The term $\epsilon_{\rm analysis\ cuts}$ is itself a product of efficiencies of the cuts used to make the data sample, e.g. electron/muon isolation. Tables 2a-2e summarize the acceptances determined from the fast MC detector simulation(s) and the electron and muon efficiencies.

The second method of determining e.g. the predicted number of electron and muon $W\gamma$ and $Z\gamma$ events is an explicit QFL simulation of electron and muon $W\gamma$ and $Z\gamma$ MC data. We start with the unformatted data files output from the Baur $W\gamma$ and $Z\gamma$ MC event generator, and then unweight the distributions according to the procedure described in CDF-1665[20]. The underlying event is simulated using ISAJET, tuning some of the parameters of ISAJET so that underlying event is in reasonable agreement with that observed in the inclusive electron and muon W and Z data samples. These data files are then put through QFL '88-'89 detector simulation and then through version 4.6 production. The QFL electron and muon $W\gamma$ and $Z\gamma$ events are then passed through the same analysis as the CDF inclusive electron and muon W and Z data samples.

Tables 3a-3b summarize the predicted number of SM $W\gamma$ and $Z\gamma$ events in the electron and muon channels, based on the fast $W\gamma$ and $Z\gamma$ MC detector simulations, and the Baur QFL/ISAJET $W\gamma$ simulation in the electron channel. In Table 3b, we also explicitly summarize for the $Z\gamma$ case the contribution (passing all event selection cuts) from Drell-Yan (DY) + $Z\gamma$. These results were also obtained with the use of the Baur $Z\gamma$ MC program and fast detector simulation program(s). The DY contribution can be seen to be small, but we explicitly correct for it in the F_{DY} term, as shown in Tables 2d-2e.

7 Determination of QCD Photon Backgrounds

The largest photon background in the $W\gamma$ and $Z\gamma$ signal samples is due to a combination of QCD jet-faking photon processes, and to a lesser extent, prompt isolated photons e.g. due

to initial/final-state radiation (quark QED bremsstrahlung). The photon background(s) due to QCD jet-faking photons in the inclusive electron and muon W and Z data samples were determined from use of the Jet-20 data sample and also use of the Vecbos $W/Z + 0, 1$ and $2-$jet MC data, using HERWIG (V5.6) to generate the underlying event and to fragment the jet(s) recoiling against the W/Z in the Vecbos $W/Z + n-$jet MC, and QFL for CDF detector simulation.

For the determination of the CEM QCD jet-faking photon background(s) from the Jet-20 data sample and the inclusive electron and muon W and Z data samples, we required the same event selection criteria as described above in the determination of photon efficiencies for e.g. the $ET4$, $\sum PT4$, etc. cuts. Note that the Jet-20 data was also re-clustered with ELES $Seed = 1.0\ GeV$ and $Sum = 1.5\ GeV$ in EMCLST in an identical manner to that done for the inclusive electron and muon W and Z data samples.

Events in the Jet-20 data sample were selected by requiring two leading jets with one central jet, the other jet central or plug, and requiring both jets to have (QDJSCO-corrected) $E_T^J > 15\ GeV$ and $M_{JJ} > 40\ GeV$. The physics motivation for this choice of jet selection was to obtain a sample of events which had approximately the same $\sqrt{\hat{s}}$ as that for the inclusive electron and muon W and Z data samples. Since most of the Jet-20 data are di-jet type events, the two-jet invariant mass distribution of the leading two jets is approximately that of the W and/or Z mass; the *extra* jets in these events are then likened to the jets in $W/Z+$jets data.

The CEM QCD jet-faking photon background in each of the four inclusive data samples was determined by summing up (separately) for each of the four inclusive W/Z data samples, E_T-bin-by-E_T-bin, the product of the number of QDJSCO-corrected central jets ($|\eta| < 1.1$) in a given E_T-bin (of width $= 2.5\ GeV$) that were above $E_T > 5.0\ GeV$ and were more than $\Delta R_{\ell-J} > 0.7$ away from the decay lepton(s) in each of the four inclusive data samples, times the number of ELES objects in the same E_T-bin of the re-clustered Jet-20 data above $E_T > 5.0\ GeV$ passing all of the above-described CEM photon cuts, that were more than $\Delta R_{TJ-ELES} > 1.4$ away from the two leading trigger jets in the Jet-20 data, divided by the number of QDJSCO-corrected extra (i.e. non-leading) central jets ($|\eta| < 1.4$) above $E_T > 5.0\ GeV$ in the same E_T-bin that were also more than $\Delta R_{TJ-XJ} > 1.4$ away from the two leading trigger jets in the Jet-20 data. In other words, the determination of the QCD jet-faking photon background in each of the four inclusive W/Z data samples, for (corrected) $E_T > 5.0\ GeV$ was obtained by:

$$N_{Bkgnd}^{Jet\ W_e} = \sum_i N_i^{Jet\ W_e}(|\eta_J| < 1.1, \Delta R_{\ell-J} > 0.7) \times \left(\frac{N_i^{Fid\ CEM\ J20}(\Delta R_{TJ-ELES} > 1.4)}{N_i^{Extra\ Jet\ J20}(\Delta R_{TJ-XJ} > 1.4)} \right)$$

$$N_{Bkgnd}^{Jet\ W_\mu} = \sum_i N_i^{Jet\ W_\mu}(|\eta_J| < 1.1, \Delta R_{\ell-J} > 0.7) \times \left(\frac{N_i^{Fid\ CEM\ J20}(\Delta R_{TJ-ELES} > 1.4)}{N_i^{Extra\ Jet\ J20}(\Delta R_{TJ-XJ} > 1.4)} \right)$$

$$N_{Bkgnd}^{Jet\ Z_e} = \sum_i N_i^{Jet\ Z_e}(|\eta_J| < 1.1, \Delta R_{\ell-J} > 0.7) \times \left(\frac{N_i^{Fid\ CEM\ J20}(\Delta R_{TJ-ELES} > 1.4)}{N_i^{Extra\ Jet\ J20}(\Delta R_{TJ-XJ} > 1.4)} \right)$$

$$N_{Bkgnd}^{Jet\ Z_\mu} = \sum_i N_i^{Jet\ Z_\mu}(|\eta_J| < 1.1, \Delta R_{\ell-J} > 0.7) \times \left(\frac{N_i^{Fid\ CEM\ J20}(\Delta R_{TJ-ELES} > 1.4)}{N_i^{Extra\ Jet\ J20}(\Delta R_{TJ-XJ} > 1.4)} \right)$$

The number of Jet-20 events passing the "trigger" jet requirements was 11726 events. A total of 431 Jet-20 central ELES objects had $E_T > 5\ GeV$ that were $\Delta R > 1.4$ away from a

jet. Of these, a total of 269 were fiducial CEM. A total of 20, 15, 12 and 11 events passed the entirety of the 2×2 matrix of $ET4 = 2,1\ GeV$ and $\sum PT4 = 2,1\ GeV$ photon cuts, for the 2-2, 2-1, 1-2 and 1-1 photon cuts, respectively. The number of jets in the inclusive W/Z event samples with central jets was 2041 (1099) for e (μ) $W-$data and 175 (69) for e (μ) $Z-$data.

An independent cross-check on the determination of the level of CEM QCD jet-faking photon background(s) for each of the four W/Z data samples was obtained with the use of the Vecbos $W/Z + n-$Jet MC. A properly normalized, luminosity-weighted sample of e/μ Vecbos/HERWIG $W/Z + 0,1$ and $2-$jet QFL MC data was passed through the same set of above-described $W\gamma\,/Z\gamma$ event selection cuts and to obtain predictions for the number of QCD jet-faking CEM photons in the central electron $W\gamma$ data sample.

The predicted number of CEM QCD jet-faking photon background events obtained via these two methods are summarized in Tables 4a-4b below for each of the four $W\gamma$ and $Z\gamma$data sets. The uncertainties quoted in the tables are statistical only (we discuss systematic uncertainties associated with the QCD jet-faking photon backgrounds in the next section).

Plots of the Jet-20 background determination for the electron $W\gamma$ sample for the $ET4 < 2$, $\sum PT4 < 2$ cut are shown in Fig. 12a. A comparison of the various jet E_T spectra for the four data samples are shown in Fig. 12b. The QCD Jet-20 γ fake rates for electron and muon $W\gamma\,/Z\gamma$ data samples are shown in Fig. 12c, for the $ET4 < 2$, $\sum PT4 < 2$ cut.

8 Additional Backgrounds in the $W\gamma$ and $Z\gamma$ Data Samples

If no additional event selection cuts other than those described above are used, $Z\gamma$ and inclusive $Z+$jet processes (where the QCD jet fakes a photon) can contribute to $W\gamma$ background (particularly in the muon channel) when one of the leptons from the $Z-$decay is not detected, resulting in the (one-legged) Z being mis-identified as a W. For electron/muon $W\gamma$ candidate events, contamination from one-legged $Z\gamma$ events is further suppressed in each sample by making a "no 2^{nd} track" cut for 3-D tracks with $P_T > 10\ GeV/c$ and requiring that if such 3-D tracks are found, that they must not be pointing at a *hadronic* jet (EM fraction < 0.8); if the 2^{nd} track is *not* pointing at a jet and has a pair-mass of $70 < M_{ee} < 110$ ($40 < M_{\mu\mu} < 140$) for electrons (muons) the event is rejected as a one-legged $Z\gamma$ candidate. For muons, the 2^{nd} track is also required to have a minimum-ionizing calorimeter signature). From studies using QFL $W\gamma$MC simulated data for electrons and muons, no signal events are lost by these 2^{nd} track-type cuts. The contributions to the $W\gamma$ background from these processes were estimated using inclusive Z data and the Baur $W\gamma$ and $Z\gamma$ Monte Carlos. These results are summarized in the Table 5a below, for the $ET4 = 2\ GeV$, $\sum PT4 = 2\ GeV$ choice of photon cut. We note here that one electron 1-legged $Z\gamma$ candidate was found in the electron $W\gamma$ data sample (~ 0.6 events expected), and two 1-legged $Z\gamma$ candidates were found in the muon $W\gamma$ data sample (~ 0.7 events expected).

The process $(W \to \tau\nu_\tau) + \gamma$ and $(W \to \tau\nu_\tau) +$ Jet can also contribute to the background in the electron and muon $W\gamma$ data samples when the τ decays to an electron or muon, respectively. The corresponding processes $(Z \to \tau^+\tau^-) + \gamma$ and $(Z \to \tau^+\tau^-)) +$ Jet can also contribute to the background in the electron and muon $Z\gamma$ data samples. As the Baur $W\gamma$ and $Z\gamma$ MC programs originally did not include tauonic decays of W/Z bosons, a set

of $\tau \rightarrow \nu_\tau \ell \bar{\nu}_\ell$ tau lepton decay subroutines were written, which included the proper tau decay polarization effects. The Baur MC event generators and fast $W\gamma$ and $Z\gamma$ MC detector simulation programs were modified to include tau decays. The tau decay contribution to the $W\gamma$ background in the electron and muon channels was found to be small, and is summarized in Table 5a below, for the $ET4 = 2\ GeV$, $\sum PT4 = 2\ GeV$ choice of photon cut. The tau decay contribution to the $Z\gamma$ background in the elctron and muon channels was found to be extremely small ($<<$ 1 *event*), and hence is neglected.

In Tables 5b-5e, we summarize the backgrounds for each of the four data samples. The first uncertainty in each table entry is the statistical uncertainty; the second uncertainty is the systematic uncertainty on the Jet-20 QCD determination of the QCD jet-faking photon background for that channel.

The *systematic* uncertainty on the QCD background for each of the four channels is (conservatively) defined as the difference between the QCD background as determined from the Jet-20 data minus the QCD background as determined from the Vecbos/HERWIG/QFL $W/Z + n-$jets MC simulations.

We spent a considerable amount of effort attempting to better understand the systematic under-predicting of the QCD background as obtained from the Vecbos/HERWIG/QFL $W/Z + n-$jets MC simulation relative to that from the Jet-20 QCD background determination. The original version of HERWIG that was used (V5.3) did not include initial/final-state photon bremm off of e.g. quarks. The latest version does, however we found that there was no observable/detectable increase in the background determination with quark bremm enabled in the MC. The reason for this is two-fold. First, the bremm code used in HERWIG is overly simplistic - it uses the effective radiator approximation, which is reasonable only for small angle (i.e. collinear) bremm. It is a poor approximation in the wide-angle regime, e.g. for $\Delta R_{q-\gamma} > 0.7$, well away from jets. Second, a simplistic estimate of the number of background $W\gamma\,/Z\gamma$ events with photons due to wide-angle $final-state$ quark bremm from charge $+2/3$ $(-1/3)$ u (d) quark "jets" fragmenting (via bremm) to a photon passing our photon cuts (N.B. initial-state quark bremm is part of the $W\gamma\ /Z\gamma$ *signal*!), scaling results obtained using Bob Wagner's radiative W/Z MC event generator + fast detector simulation, and also e.g. a radiative J/ψ decay MC event generator, indicate that the contribution from final-state quark-bremm processes in W/Z+jets is small, e.g. less than $<$ 0.3 events for the electron $W\gamma$ channel, and less so for the other three channels.

We also investigated the sensitivity of the Vecbos/HERWIG/QFL $W/Z + n-$jets MC simulations to the minimum jet E_T cutoff (at the parton level) in the Vecbos event generator, and found the QCD background predictions to be insensitive to this cutoff parameter. The lowest jet threshold recommended by Walter Giele (one of the authors of the Vecbos program) was $E_T^J > 8\ GeV$. We were able to successfully run the program with $E_T^J > 6\ GeV$ but no lower. Our Vecbos/HERWIG/QFL $W/Z + n-$jets MC simulation results are for the $E_T^J > 8\ GeV$ threshold.

In addition to the above, we also studied the possibility of a jet energy scale miscalibration in the Vecbos/HERWIG/QFL $W/Z+n-$jets MC simulation, for the regime of jet fragmentation which would give us QCD jet-faking photons, passing all of our photon cuts, including the $ET4$ and $\sum PT4$ cuts. We found e.g. for the electron Vecbos/HERWIG/QFL $W + n-$jets MC simulations, that increasing the "observed" photon E_T spectrum by a constant factor of $7 \pm 4\%$ brought the Vecbos/HERWIG/QFL $W + n-$jets MC simulations into good agreement with the Jet-20 background determination for this channel. However,

we also found that for the other three channels, which had much poorer statistics (both in the data and the MC), that an increase $15-25\%$ was required.

We note here that we also worried about the calibration of the CEM energy scale at $E_T^\gamma \sim 5\ GeV$. We conferred (as always) with Barry Wicklund on this point. From E/P studies he had done using low-energy electrons, the CEM energy scale at this energy was correct to within $\sim 1\%$[21]. This level of uncertainty has a negligible impact on the number of $W\gamma\ /Z\gamma$ events expected and/or predicted.

Due to limited statistics associated with both the Jet-20 QCD jet-faking photon background determination(s) and the the Vecbos/HERWIG/QFL $W/Z+n-$jets MC simulations for each of the four samples, we were unable to reliably ascertain that a single factor was the *sole* source of the systematic discrepancy between the QCD jet-faking photon background(s) as predicted by the Jet-20 data and the Vecbos/HERWIG/QFL $W/Z+n-$jets MC. Hence we retained the conservative definition of the systematic uncertainty on the QCD background, as defined above.

9 The $W\gamma$ and $Z\gamma$ Candidate Event Samples

The number of electron and muon $W\gamma$ and $Z\gamma$ candidates for the matrix of 4 different photon cuts are summarized in Tables 6a and 6b. Our "official" result is based on the $ET4 < 2$, $\sum PT4 < 2$ photon cut; the other three photon cuts were used only for the explicit purpose of investigating the stability of the signal as a function of varying the photon cut(s) that were used in this analysis. Tables 7a and 7b summarize run # and event # for each of the four candidate event samples. Table 7c summarizes run # and event # for one-legged $Z\gamma$ candidates (background in $W\gamma$ samples). Tables 8a-8d summarize some of the salient kinematical properties of each of the events in the four samples. Figures 13a-13c summarize some of the kinematic properties of electron/muon $W\gamma$ and $Z\gamma$ candidate event samples, overlaid with the MC expectations for the signal in each channel, normalized to the number of predicted MC events in each sample.

10 Determination of $\sigma * BR(W+\gamma)$ and $\sigma * BR(Z+\gamma)$ in the Electron and Muon Channels

The experimental results for the cross sections $\times$ branching ratios for $W\gamma$ and $Z\gamma$ in the electron/muon channels were determined from the use of

$$\sigma_W \cdot B(W \to \ell\nu_\ell\gamma) = \frac{\mathcal{N}^{W\gamma}_{observed} - \sum \mathcal{N}^{W\gamma}_{background}}{A_{W\gamma} \cdot \epsilon_{W\gamma} \cdot \int \mathcal{L}_\ell dt}$$

$$\sigma_Z \cdot B(Z \to \ell^+\ell^-\gamma) = \frac{\mathcal{N}^{Z\gamma}_{observed} - \sum \mathcal{N}^{Z\gamma}_{background}}{A_{Z\gamma} \cdot \epsilon_{Z\gamma} \cdot \int \mathcal{L}_\ell dt}$$

The number of observed candidates for each sample was input to a detailed MC simulation program which simulated 10^6 CDF experiments, Poisson-fluctuating the number of observed events, along with gaussian fluctuations of the integrated luminosities, and all $A \cdot \epsilon$ terms, as given in Tables 1-2. The backgrounds for each channel were gaussian-fluctuated and subtracted from the observed number of events on an "experiment-by-experiment" basis.

The experimental cross section $\sigma \cdot BR$ was calculated from a histogram (incremented once per experiment). The mean and $\pm$ 1 σ (double-sided) uncertainties on the mean value of $\sigma \cdot BR$ were obtained, as well as the 68.3%, 90.0%, and 95.0% single-sided C.L. upper limits to $\sigma \cdot BR$, using the PDG method of a bounded physical region[22]. Tables 9a-9b summarize the # signal events for $W\gamma$ and $Z\gamma$ electron and muon results. The first uncertainty is statistical only; the second uncertainty is the systematic uncertainty associated with the QCD photon background determination. The cross section results for each of the four channels are summarized in Tables 10a-10b for $W\gamma$ and $Z\gamma$. The first uncertainty is statistical only; the second uncertainty is the systematic uncertainty associated with the integrated luminosity, acceptances and efficiencies; the third uncertainty is the systematic uncertainty associated with the QCD photon background determination. Tables 11a-11b summarize the # signal events and cross section results for each of the four channels for the $ET4 < 2$, $\sum PT4 < 2$ photon cut.

11 Combining the e and μ Cross Sections

The method we used for combining the e and μ $\sigma * BR(W + \gamma)$ and e and μ $\sigma * BR(Z + \gamma)$ cross sections was again based on MC simulation methods, simulating 10^6 CDF experiments (we merged together the e and μ MC $\sigma * BR$ programs into one program and carefully take into account the correlations between the two data samples). The method involves the assumption that the electron and muon channels are measuring the same physical process (i.e. lepton universality holds: $\sigma * BR = \sigma * BR_e = \sigma * BR_\mu$) Then, as can be derived trivially, or e.g. via formal derivation from the joint likelihood $\mathcal{L}_{e+\mu} = \mathcal{L}_e \cdot \mathcal{L}_\mu$:

$$\sigma * BR(V + \gamma) = \frac{N_e^{signal} + N_\mu^{signal}}{\int \mathcal{L}_e dt \cdot A_e^{V\gamma} \cdot \epsilon_e^{V\gamma} + \int \mathcal{L}_\mu dt \cdot A_\mu^{V\gamma} \cdot \epsilon_\mu^{V\gamma}}$$

We have checked this method of combining cross sections with test distributions and also with analytic, weighted-average methods. All results agree extremely well with each other for these comparative tests.

Figures 14 and 15 show the electron, muon and $e + \mu$ combined $W\gamma$ and $Z\gamma$ $\sigma * BR$ probability distributions, respectively. For $W\gamma$, all probability distributions are smooth, due to the fact that the gaussian-distributed uncertainties associated with e.g. the QCD jet-faking photon and other background(s) smears out the quantization of the small-statistics Poisson fluctuations on 8, 5 and 13 observed e, μ and $e + \mu$ $W\gamma$ events. These $\sigma * BR$ probability distributions are nearly gaussian, but with a small high-side tail, due mainly to small-number Poisson statistics. The narrowing of the $\sigma * BR$ probability distribution for the $e + \mu$ combined cross section is readily apparent. For $Z\gamma$, the probability distributions clearly show the small-statistics Poisson nature of these results. For $Z\gamma$, the (fractional) level of QCD jet-faking photon backgrounds in the individual e and μ $Z\gamma$ data samples ($\sim$ 10%) is significantly less than that for the $W\gamma$ data samples ($\sim$ 40%). The cross section probability distributions are extremely finely binned, so that we may determine the $\pm$ 1 σ (68.3%) double-sided and 68.3%, 90.0% and 95.0% single-sided CL limits to the $\sigma * BR(V + \gamma)$ (using again the bounded physical region for the latter limits) for each cross section probability distribution. Table 12 summarizes the combined $e + \mu$ $W\gamma$ and $Z\gamma$ cross section results.

12 Additional $\sigma * BR(W+\gamma)$and $\sigma * BR(Z+\gamma)$Systematic Uncertainties

The systematic effects of varying the diboson $V+\gamma$ ($V = W/Z$) P_T-distribution, structure function (SF) choice and the Q^2-scale for the nominal SF (HMRS-B) were studied for each of the four channels. Since there are no experimental measurements of the diboson P_T spectrum, and no rigorous theoretical predictions of the $W/Z+\gamma$ P_T distributions (soon!), we approximated the $W/Z+\gamma$ P_T distributions by the measured CDF W/Z P_T distributions[17], which is reasonable for the photon P_T range we are sensitive to. For the nominal SF choice, for each of the four channels, the MC diboson P_T distributions were varied within the $\pm 1\sigma$ limits allowed by the fit to the $d\sigma/dP_T$ distribution, using the same method as the muon $\mathcal{R}$ analysis (see e.g. CDF-1504 and CDF-1629). The method involved using the fast MC detector simulation programs to obtain the MC $\sigma * BR(V+\gamma)$ and all kinematic/geometrical acceptances, requiring the MC events pass all event selection cuts, and including the efficiencies of these cuts in the fast MC detector simulation. The acceptance results for each P_T choice were then input to the *experimental* determination of the $\sigma * BR(V+\gamma)$ for each of the four decay channels. Thus, a total of four P_T distributions for each decay channel were investigated to obtain both MC and experimental results: (1) No P_T boost, (2) a "soft" P_T boost, (3) a nominal P_T boost and (4) a "hard" P_T boost. The "soft", nominal and "hard" boson P_T distributions are shown in Figure 16. Note that the "No" P_T boost study was included solely completeness' sake, and is *not* used in the determination of any of the systematic uncertainties. The results of these studies are shown in figures 17a-17c and summarized in Table 13a below. The systematic uncertainties for the combined $e+\mu$ results were obtained via the same method as used for combining the "nominal" $e+\mu$ cross sections. Figure 17a shows the variation in $\sigma * BR(V+\gamma)$ for the MC and experiment for each of the four channels as a function of P_T distribution choice. The error bars are associated with the statistical uncertainty on the acceptance determination and the uncertainty on the MC generated $\sigma * BR(V+\gamma)$ Figure 17b shows the $\sigma * BR$ difference between MC and experiment where the difference $\Delta\sigma(V+\gamma)_{MC-Expt} \equiv 0$ for the nominal P_T distribution. The other differences are therefore defined relative to the nominal P_T distribution. Figure 17c shows the systematic trends for the MC and experiment separately. Again, the $\Delta\sigma(V+\gamma)_{MC,Expt} \equiv 0$ for the nominal P_T distribution choice; the others are defined relative to the nominal. Table 13a summarizes the $\pm 1\sigma$ systematic uncertainties $\Delta\sigma_{MC}$, $\Delta\sigma_{Expt}$ and $\Delta\sigma_{MC-Expt}$ for the $\pm 1\sigma$ systematic excursions in the diboson P_T distributions.

Similarly, the systematic uncertainties associated with the Q^2-scale dependence for the nominal SF choice (HMRS-B) were studied by varying the Q^2-scale between the limits $M^2_{V+\gamma}/4 < Q^2 < 4M^2_{V+\gamma}$, for each of the four decay channels. Figure 18a-c show these results for (1) $Q^2 = M^2_{V+\gamma}/4$, (2) $Q^2 = M^2_{V+\gamma}$ (nominal) and (3) $Q^2 = 4M^2_{V+\gamma}$. These results are summarized in Table 13b below. A technical note here is that we ignore possible correlations between Q^2 scale dependence and the shape of the diboson P_T distribution, which are correlated with each other due to four-momentum conservation in the $V+\gamma$ production process. Hence treating these two effects as independent of each other will tend to overestimate the sensitivity to these effects.

The systematic uncertainties associated with the choice of structure functions for each of the four decay channels was investigated using various SF choices. Figure 19a shows the MC $\sigma * BR_{gen}$ results for the *generated* cross sections output from the Baur $W\gamma$ and $Z\gamma$ MC

programs for 13 different SF choices. Of these a sub-set of 5 different SF choices (DFLM-260, MRS-B, HMRS-B, MRS-S0 and MT-B1) were analyzed using the fast MC detector simulation programs to obtain MC $\sigma * BR_{cuts}$ and kinematic/geometrical acceptance results. Figures 19b-19d show the analogous set of plots as for the P_T and Q^2 scale dependence studies discussed above. Table 13c summarizes the systematic uncertainties for the SF choices.

The systematic uncertainties associated with varying the diboson P_T distributions, the Q^2-scale dependence and the SF choices for the MC and the experimental results are seen to be correlated with each other. The MC and experimental $\sigma * BR(V+\gamma)$ results for each of the four decay channels, in isolation of each other, must include the respective contributions to the overall uncertainty from these three systematic uncertainties. However, due to these correlations between MC and experimental systematic uncertainties, we *must* use the $\Delta\sigma(V+\gamma)_{MC-Expt}$ *difference* in obtaining e.g. limits on the κ and λ parameters for $W\gamma$ or e.g. limits on the h_{30}^Z and h_{40}^Z parameters for $Z\gamma$. In Table 13d we summarize the (quadrature) combined systematic uncertainties associated with varying the diboson P_T distribution, the Q^2-scale dependence and SF choices. We discuss the details of obtaining limits on e.g. the κ and λ (h_{30}^Z and h_{40}^Z) parameters for $W\gamma$ ($Z\gamma$) below.

13 $W\gamma$ and $Z\gamma$ Cross Section Results

We summarize here the "official" results for the individual e, μ $W\gamma$ and $Z\gamma$ cross sections and the combined $e+\mu$ $W\gamma$ cross sections, taking into account the $P_T(V+\gamma)$, Q^2-scale dependence and SF systematic uncertainties. These results are intended to be used solely for quotation as cross section measurements; these results must *not* be used for e.g. determination of limits on the κ and λ (h_{30}^Z and h_{40}^Z) parameters, due to the non-negligible correlations between the MC predicted $\sigma * BR_{cuts}$ and the experimental cross section results, even though these results have slightly larger uncertainties. These results are in good agreement with SM predictions.

$$\sigma * BR(W\gamma)_e = 17.0^{+13.8}_{-13.3}\ (stat+syst)\ pb \qquad \sigma * BR(W\gamma)_\mu = 19.4^{+19.2}_{-18.0}\ (stat+syst)\ pb$$
$$\sigma * BR(W\gamma)_{e+\mu} = 17.9^{+11.4}_{-10.7}\ (stat+syst)\ pb \qquad \sigma * BR(W\gamma)_{SM} = 19.0\ ^{+3.3}_{-0.9}\ (stat+syst)\ pb$$

$$\sigma * BR(Z\gamma)_e = 6.8\ ^{+5.9}_{-5.8}\ (stat+syst)\ pb \qquad \sigma * BR(Z\gamma)_\mu = 13.6^{+11.2}_{-10.1}\ (stat+syst)\ pb$$
$$\sigma * BR(Z\gamma)_{e+\mu} = 9.2\ ^{+5.6}_{-5.2}\ (stat+syst)\ pb \qquad \sigma * BR(Z\gamma)_{SM} = 4.7\ ^{+0.7}_{+0.2}\ (stat+syst)\ pb$$

14 $W\gamma$ and $Z\gamma$ Cross Section Ratios

The first set of physics results we can obtain is the formation of four cross section ratios: $\sigma * BR(W\gamma)/\sigma * BR(W)$, $\sigma * BR(Z\gamma)/\sigma * BR(Z)$, $\sigma * BR(W\gamma)/\sigma * BR(Z\gamma)$, and $\sigma * BR(W\gamma)/\sigma * BR(Z)$. The latter cross section ratio CDF has published results on for the e and μ channels[11]. These four cross section ratios form a "sum rule", and are shown below in Figure 20 and summarized in Table 14. By taking ratios of these cross sections, as in the case of the W/Z cross section ratio, many common experimental (and theoretical) uncertainties cancel. These ratios, such as the first cross section ratio, $\sigma * BR(W\gamma)/\sigma * BR(W)$, are sensitive in the SM to the destructive interference between the various Feynman amplitudes for the $W\gamma$ process[23]. The SM prediction for this cross section ratio (for our choice of photon cuts) is $\sim$ 0.9%, whereas if the radiation were due soley to final-state bremm. this

ratio would be $\sim$ 0.5%. The experimental results, while presently statistically compatible with either hypothesis, favors the SM $W\gamma$ prediction by approximately 0.5 SD. The cross section ratio of $\sigma * BR(Z\gamma)/\sigma * BR(Z)$ is also shown in Figure 20, along with its SM prediction of $\sim$ 2.4%. This experimental cross section ratio, albeit with (very) limited statistics, tends to be high by approximately $0.5 - 1.0$ SD. We note here that this was also the case for the observed 1-legged $Z + \gamma$ background in the electron/muon $W\gamma$ sample(s). The third cross section ratio, that of $\sigma * BR(W\gamma)/\sigma * BR(Z\gamma)$ is predicted to be $\sim$ 4.0 in the SM. If the photons observed in W events were due soley to final-state bremm, this ratio is expected to be $\sim$ 2.5 instead. The data favor this latter ratio, soley because the $Z\gamma$ cross section is higher than the SM prediction. We note here that for future $W\gamma/Z\gamma$ analyses, this particular cross section ratio is also quite sensitive to the destructive interference in the $W\gamma$ case; the photon P_T spectrum is predicted to fall more steeply with increasing P_T than in the $Z\gamma$ case, which has no such destructive interference effects in the SM. The fourth cross section ratio, $\sigma * BR(W\gamma)/\sigma * BR(Z)$ is the canonical inclusive W/Z cross section ratio, which is predicted (and measured) to be $\sim$ 10.0. Our cross section ratio results are summarized below:

$$\begin{array}{llll} \mathcal{R}(W\gamma/W)_{e+\mu} & = 0.8^{+0.5}_{-0.5}\% \ (stat + syst) & \mathcal{R}(Z\gamma/Z)_{e+\mu} & = 4.3^{+2.5}_{-2.4}\% \ (stat + syst) \\ \mathcal{R}(W\gamma/Z\gamma)_{e+\mu} & = 1.9^{+2.0}_{-1.4} \ \ (stat + syst) & \mathcal{R}(W/Z)_{e+\mu} & = 10.0^{+0.7}_{-0.7} \ \ (stat + syst) \end{array}$$

15 Limits on Anomalous Couplings for $W\gamma$ and $Z\gamma$

We obtain 68.3%, 90.0% and 95.0% CL limits on the $\Delta\kappa = \kappa - 1$ and λ parameters for $W\gamma$ (h^Z_{30} and h^Z_{40} parameters for $Z\gamma$) by running the Baur $W\gamma$ ($Z\gamma$) MC program, stepping through a matrix of 80 $\Delta\kappa$ and λ (58 h^Z_{30} and h^Z_{40}) parameters, and analyzing the MC event data with the use of the fast $W\gamma$($Z\gamma$) MC detector simulation programs. We record the MC $\sigma \cdot BR(V + \gamma)_{gen,cuts}$ and kinematic/geometrical acceptances and the predicted number of MC e or μ events for each $W\gamma$ ($Z\gamma$) decay channel, for each cross section point in the $\kappa - \lambda$ ($h^Z_{30} - h^Z_{40}$) plane. This includes recording *all* statistical uncertainties for these variables. For $W\gamma$, the Baur MC was run with non-zero values of anomalous parameters with a fixed Λ scale of $\Lambda = 10\ TeV$. The cross section results are negligbly different if e.g. a compositeness scale $\Lambda = 1.0\ TeV$ is chosen, simply because the parton SF luminosities (for Bjorken-x of $x \sim 0.5$) contribute negligibly to the overall $W\gamma$ cross section at our center-of-mass energy. For $Z\gamma$, which has much greater sensitivity to the compositeness scale Λ, three sets of scales were used: $\Lambda = 250$, 500 and 750 GeV.

Each set of MC $\sigma \cdot BR(V+\gamma)_{cuts}$ data is then fit using MINUIT to obtain a 3-dimensional description of the $\sigma * BR(V + \gamma)$ cross section surface in the $\Delta\kappa - \lambda$ ($h^Z_{30} - h^Z_{40}$) plane for $W\gamma$ ($Z\gamma$). The parametrization of the fit is of the following form:

$$\sigma(x, y) = \sigma_{SM} + ax + bx^2 + cy + dy^2 + exy$$

where $x = \Delta\kappa$ (h^Z_{30}) and $y = \lambda$ (h^Z_{40}). No higher-order terms in x, y are needed, since the invariant amplitudes $\mathcal{M}$ containing the anomalous contributions to the $W\gamma$ /$Z\gamma$ processes are *linear* in their anomalous parameters (κ, λ; h^Z_{30}, h^Z_{40}, etc.). The terms in the expression given above that are linear in x, y are due to interference between the various amplitudes associated with the $W\gamma$ /$Z\gamma$ processes. Note that if the coefficients associated with these terms were zero, the expression would be the equation describing the surface of an elliptic paraboloid. The MINUIT fits to each data set returns the fitted values of the parameters

σ_{SM}, $a-e$ and their uncertainties. The χ^2 of the fits and the fit residuals are also returned; in general the χ^2 of the fits are quite good. The largest fit residuals are always associated with the extreme values of anomalous parameters, well away from the region of interest (i.e. the SM).

The $\Delta\sigma(V+\gamma)_{MC-Expt}$ systematic uncertainties associated with the diboson P_T distribution, Q^2-scale dependence and SF choice are included in the MC $\sigma * BR(V+\gamma)_{cuts}$ curves (as a function of κ/λ for $W\gamma$or h_{30}^Z/h_{40}^Z for $Z\gamma$). For the purposes of obtaining limits on these parameters, the MC $\sigma * BR(V+\gamma)$ "surfaces" are "down-shifted" relative to their nominal central-value MC prediction by $-1.0\ \sigma$, where σ is the quadrature sum of the MC statistical uncertainty on $\sigma * BR(V+\gamma)$ and the $MC-Expt$ systematic uncertainties associated with the diboson P_T distribution, Q^2-scale dependence and SF choice. The intersection of the plane containing e.g. the 68.3%, 90.0% or 95.0% CL limit on the experimental $\sigma * BR(V+\gamma)$ with the "downshifted" MC $\sigma * BR(V+\gamma)$ surface determines the limits on (contours of) the κ/λ parameters for $W\gamma$ and/or h_{30}^Z/h_{40}^Z for $Z\gamma$.

The 68.3%, 90.0% and 95.0% CL limits on the $\Delta\kappa = \kappa-1$ and λ parameters for electron, muon and $e+\mu$ combined $W\gamma$ results are summarized in Tables 15a-15b. Figures 21a and 21b show the projections of the $W\gamma$ cross section on the κ/λ axes. The central value of the electron, muon an combined experimental results are shown as a solid horizontal line in each figure, the $\pm 1\sigma$ (stat+syst) (68% double-sided CL) uncertainties are shown as dotted horizontal lines. The 90.0% and 95.0% single-sided CL upper limits to the experimental cross section are shown as a horizontal dashed line and a horizonal solid line, respectively.

The 68.3%, 90.0% and 95.0% single-sided CL contours in the $\Delta\kappa-\lambda$ plane for the $e+\mu$ combined $W\gamma$ results are shown in Figure 22. Note that there are possible values of $\Delta\kappa$ and λ where the magnetic dipole moment μ_W and/or the electric quadrupole moment Q_W of the W boson vanish, separately, and one point where they both vanish simultaneously. This point is at present contained within the 68.3% CL limit contour. Note also the displacement of the location of the minimum of the $\sigma * BR(W+\gamma)$ cross section relative to the SM value.

We note here that tree-level unitarity places restrictions on the maximum allowed values of $\Delta\kappa$ and λ, which assuming that only one anomalous coupling is non-zero at a time, and for $\Lambda >> M_W$, the unitarity limits are[4]:

$$|\Delta\kappa| < \frac{7.4\ TeV^2}{\Lambda^2} \quad (\lambda = 0)$$

$$|\lambda| < \frac{4.0\ TeV^2}{\Lambda^2} \quad (\Delta\kappa = 0)$$

A comparison of these restrictions for e.g. $\Lambda = 1.0\ TeV$ (or less) with the κ/λ limits shows that e.g. for the 90.0% CL limits obtained with the individual electron/muon $W\gamma$ results, we are near the limit of sensitivity to compositeness scales beyond these Λ values, whereas for the combined $e+\mu$ result we do better. We also have good sensitivity at the 90% CL limits on the λ parameter for the individual electron/muon and combined $W\gamma$results at (and below) this value of compositeness scale.

The UA2 experiment recently published limits on κ and λ from an analysis of 13 pb^{-1} of electron $W\gamma$ data[24]. They analyzed their data in a manner equivalent to ours, comparing the number of signal events to the number of predicted events. Our results are very competative with theirs, for this method, as summarized in Table 16a. They also published limits on κ and λ obtained by fitting the P_T^γ spectrum, comparing observed vs. expected for different

κ and λ parameter values. They obtain better limits via this method, however this method is potentially more sensitive to systematic effects e.g. associated with the QCD corrections to $P_T(W+\gamma)$, which are not discussed in their paper. These results are summarized in Table 16b. We note here that because the correlations between κ and λ are much stronger for $\sqrt{s} = 630\ GeV$ than at the Tevatron, the *area* contained within our $e+\mu$ combined 68.3% (95%) contours in the $\kappa - \lambda$ plane is approximately 75% of that contained within the corresponding UA2 contours, which were obtained using their P_T^γ method![3] See/compare Figure 5 of their paper to our $\kappa - \lambda$ contours. This is in fact the most appropriate measure of comparison of $\kappa - \lambda$ limit results from the two experiments.

We can go one step further, to turn results on limits on the κ and λ parameters into limits on the W boson magnetic dipole moment, μ_W, electric quadrupole moment Q_W and the W boson mean-squared charge radius, $< R_W >^2$, since they are related to the κ and λ parameters by:

$$\begin{aligned}
\mu_W &= \tfrac{e}{2M_W}(2+\Delta\kappa+\lambda) \quad \text{Magnetic Dipole Moment} \\
Q_W &= -\tfrac{e}{M_W^2}(1+\Delta\kappa-\lambda) \quad \text{Electric Quadrupole Moment} \\
< R_W >^2 &= \tfrac{1}{M_W^2}(1+\Delta\kappa+\lambda) \quad \text{Mean-Squared Charge Radius}
\end{aligned}$$

Recall that in the SM (at the tree level): $\Delta\kappa = 1-\kappa = 0$, $\lambda = 0$. It is illuminating to explicitly calculate the numerical values of these SM parameters:

$$\mu_W^\circ = \tfrac{e\hbar c}{2M_W c^2} = 3.691 \pm 0.012 \times 10^{-16}\ MeV/T$$

$$(\mu_e^\circ = \tfrac{e\hbar c}{2M_e c^2} = 5.788 \pm 0.000 \times 10^{-11}\ MeV/T)$$

$$Q_W^\circ = -e\left(\tfrac{\hbar c}{M_W c^2}\right)^2 = -e\lambda_W^2 = 6.063 \pm 0.041 \times 10^{-6}\ e-fm^2$$

$$\lambda_W = \tfrac{\hbar c}{M_W c^2} = 2.462 \pm 0.008 \times 10^{-3}\ fm = 2.462 \pm 0.008 \times 10^{-16}\ cm$$

Where λ_W is the (reduced) Compton wavelength of the W boson. Note that the uncertainties on these quantities are due primarily to the uncertainty on the W boson mass, $M_W = 80.14 \pm 0.27\ GeV/c^2$ (combined CDF+UA2 result). Thus, we are probing (i.e. sensitive to) possible internal structure of the W boson at this distance scale! Table 16 summarizes the combined $e+\mu$ limits on the W boson electromagnetic moments, μ_W and Q_W. Figure 23 shows the 68.3%, 90.0% and 95.0% single-sided CL contours in the $Q_W/Q_W^\circ - \mu_W/\mu_W^\circ$ plane.

Recently, the CLEO experiment has observed the decay $B \to K^*\gamma$[25] which in the SM occurs through the Penguin process $b \to s\gamma$. This process is also sensitive to anomalous κ and λ values. Ulrich Baur, as well as others[26] have used the CLEO result to extract limits on κ and λ parameters. The CLEO results are more assumption-dependent than our results (e.g. the possibility of an anomalous b–quark magnetic moment is also not considered), and additionally are sensitive to the value of M_{top}. We overlay the CLEO $1-\sigma$ (i.e. 68% single-sided CL) contraints on the these parameters (courtesy of Ulrich Baur), as shown in Figures 24a-b for $M_{top} = 108,\ 200\ GeV/c^2$. These results are also shown in terms of the $Q_W - \mu_W$ parameters in Figures 25a-b. The CLEO results are complementary to (hadron) collider

[3]The area of an ellipse is $A = \pi ab$ where a and b are the major and minor "radii" of the ellipse.

results, in that the $B \rightarrow K^*\gamma$ measurement (with the appropriate cautionary remarks!) imposes significant constraints on $\Delta\kappa$, but provides little restriction on λ, whereas CDF, due to the $\hat{s}/M_W^2$ sensitivity to the λ parameter, does better on constraining this parameter than for $\Delta\kappa$.

Before discussing limits on the h_{30}^Z and h_{40}^Z $Z\gamma$ parameters, we mention here for completeness' sake that the experimental limit on the electric dipole moment (EDM) of the neutron ($d_n < 12 \times 10^{-26}\ e - cm$ @ 95% CL) imposes severe restrictions on the $\mathcal{T}$ (i.e. $\mathcal{CP}$) violating $\Delta\kappa'$ and λ' parameters[4]:

$$|\kappa'|,\ |\lambda'| < 10^{-3}$$

We obtain limits on the h_{30}^Z and h_{40}^Z $Z\gamma$ parameters using the same method(s) as for the $W\gamma$ case. As discussed earlier, for $Z\gamma$, the dependence on the compositeness scale Λ is much more significant than for the $W\gamma$ process. We compare our experimental measurement of $\sigma * BR(Z\gamma)_{expt}$ with MC predictions for three different Λ values, $\Lambda = 250,\ 500,$ and $750\ GeV$.

The 68.3%, 90.0% and 95.0% CL limits on the h_{30}^Z and h_{40}^Z parameters for electron, muon and $e+\mu$ combined $Z\gamma$ results are summarized in Tables 18a-18c. Figures 26a and 26b show the projections of the $Z\gamma$ cross section on the h_{30}^Z/h_{40}^Z axes. The central value of the electron, muon and combined experimental results are shown as a solid horizontal line in each figure, the $\pm 1\sigma$ (stat+syst) (68% double-sided CL) uncertainties are shown as dotted horizontal lines. The 90.0% and 95.0% single-sided CL upper limits to the experimental cross section are shown as a horizontal dashed line and a horizonal solid line, respectively.

Tree-level unitarity places restrictions on the maximum values of h_{30}^Z and h_{40}^Z, which assuming that only one anomalous coupling is non-zero at a time and that $\Lambda >> M_Z$, the unitarity limits are[5]:

$$|h_{30}^Z| < \frac{1.00\ TeV^3}{\Lambda^3} \quad (h_{40}^Z = 0,\ n = 3)$$

$$|h_{40}^Z| < \frac{0.03\ TeV^5}{\Lambda^5} \quad (h_{30}^Z = 0,\ n = 4)$$

The unitarity limits is shown as a dotted line on each of the figures in Figure 26a. The region *above* the point where these lines intersect each of the MC $\sigma * BR(Z\gamma)_{cuts}$ curves is excluded by unitarity considerations. For a given Λ value (250, 500, or $750\ GeV$), if the intersection of the experimental 68.3%, 90.0% or 95.0% CL limit associated with the $\sigma * BR(Z\gamma)_{expt}$ result with the MC $\sigma * BR(Z\gamma)_{cuts}$ curve(s) occurs *above* the dotted line of the unitarity limit, the experimental result simply does not have sensitivity to anomalous h_{30}^Z or h_{40}^Z values as given by the Experiment-MC $\sigma * BR(Z\gamma)$ intersection point, for compositeness scales Λ (and larger) for that particular MC $\sigma * BR(Z\gamma)$ curve. In Tables 18a-18c, we explicitly flag the $Z\gamma$ h_{30}^Z or h_{40}^Z limits which violate unitarity at the Λ scale given in each of the tables with a †

The 68.3%, 90.0% and 95.0% single-sided CL contours in the $h_{30}^Z - h_{40}^Z$ plane for the $e+\mu$ combined $Z\gamma$ results are shown in Figure 27a-27c for $\Lambda = 250,\ 500$ and $750\ GeV$. Partial wave unitarity places restrictions on the reduced amplitudes[27, 5]:

$$\sum_{\lambda_Z \lambda_\gamma} \left| A^Z_{\lambda_Z \lambda_\gamma} \right|^2 \leq \frac{1}{\alpha^2(\hat{s})} \frac{3}{10} 16 \sin^2\theta_W \cos^2\theta_W$$

Where λ_Z, λ_γ are the Z boson and photon helicities, respectively. Unitarity is violated if

$$\frac{(\frac{\hat{s}}{M_Z^2}-1)^3}{(1+\frac{\hat{s}}{\Lambda^2})^6}\left[\left(h_{30}^Z-\frac{1}{2}h_{40}^Z\frac{(\frac{\hat{s}}{M_Z^2}-1)}{(1+\frac{\hat{s}}{\Lambda^2})}\right)^2+(h_{30}^Z)^2\frac{M_Z^2/\Lambda^2}{\hat{s}/\Lambda^2}\right]\geq\frac{48}{5\alpha^2(\hat{s})}\sin^2\theta_W\cos^2\theta_W=27857.44$$

The 2-dimensional unitarity limit in the $h_{30}^Z - h_{40}^Z$ plane is indicated by a dotted line. The region contained within the dotted line is allowed by unitarity considerations. It can be seen that for $\Lambda = 250\ GeV$, that the $e+\mu$ combined limits are entirely within region allowed by unitarity, whereas for a compositeness scale of $\Lambda = 500\ GeV$, the unitarity bound is tighter than our experimental limits in a significant portion of the $h_{30}^Z - h_{40}^Z$ plane. For $\Lambda = 750\ GeV$, the unitarity bound is tighter than nearly all of our experimental limits in the $h_{30}^Z - h_{40}^Z$ plane. Thus, from $\sim 4\ pb^{-1}$ data, our sensitivity limits to anomalous $ZZ\gamma$ couplings with a compositeness scale for the Z boson of $\Lambda \sim < 500\ GeV$.

Although limited in statistical power, our experimental results on the measurement of $\sigma * BR(Z+\gamma)$ in both the e and μ channels is higher than the SM prediction, at the $\sim 1\ \sigma$ level. This could easily be due to small-statistics fluctuations, but is also consistent with the possibility of finite $ZZ\gamma$ anomalous couplings/finite Λ. Note that the apparent excess of events conspires to give us worse limits on the h_{30}^Z and h_{40}^Z parameters for a particular Λ choice, than we would have obtained if the data had been more consistent with the SM prediction. It will be interesting to repeat this analysis with the present run's data to determine whether or not this trend continues!

The L3 Collaboration has recently published a paper setting limits on the h_3^Z form factor (which they call the β parameter) from measurement of the cross section for $e^+e^- \rightarrow Z^0 \rightarrow \nu\bar{\nu}\gamma$. They obtain a limit on β of $|\beta| < 0.80$ $(95\%\ CL)$, from the absence of an excess of such events in the Z resonance region from $11.2\ pb^{-1}$ data, for $E_\gamma > \frac{1}{2}E_{beam}$[28]. Translating this result into limits on the h_{30}^Z parameter, their result is $|h_{30}^Z| < 1.16,\ 0.88,\ 0.84$ $(95\%\ CL)$, for $\Lambda = 250,\ 500,\ 750\ GeV$, respectively. The L3 results are well within the $|h_{30}^Z|$ unitarity limit for these Λ values. They exceed the $|h_{30}^Z|$ unitarity limit for $\Lambda > 1.08\ TeV$ We have analyzed our $Z\gamma$ data in terms of limits on anomalous $ZZ\gamma$ couplings. The limits for anomalous $Z\gamma\gamma$ couplings differ from those for $ZZ\gamma$ typically by only a few percent. The LEP $Z \rightarrow \nu\nu\gamma$ results are sensitive only to anomalous $ZZ\gamma$ couplings, and place no constraints on anomalous $Z\gamma\gamma$ couplings.

16 Conclusions

We have measured the cross sections × branching ratios for $W+\gamma$ and $Z+\gamma$ in the electron and muon channels using the inclusive e, μ W and Z data samples from the CDF '88-'89 collider run, with $4.05\pm0.28\ pb^{-1}$ ($3.54\pm0.24\ pb^{-1}$) electron (muon) data. For central photons with $E_T^\gamma > 5.0\ GeV$ and $\Delta R_{\ell\gamma} > 0.7$, we observe 8 (5) electron (muon) $W\gamma$ candidates and 2 (2) electron (muon) $Z\gamma$ candidates. From these events, we measure $\sigma * BR(W\gamma)$ and $\sigma * BR(Z\gamma)$ for the electron, muon and $e+\mu$ combined samples, and compare to the SM predictions:

$$\begin{array}{llll} \sigma * BR(W\gamma)_e & = 17.0^{+13.8}_{-13.3}\ (stat+syst)\ pb & \sigma * BR(W\gamma)_\mu & = 19.4^{+19.2}_{-18.0}\ (stat+syst)\ pb \\ \sigma * BR(W\gamma)_{e+\mu} & = 17.9^{+11.4}_{-10.7}\ (stat+syst)\ pb & \sigma * BR(W\gamma)_{SM} & = 19.0\ ^{+3.3}_{-0.9}\ (stat+syst)\ pb \end{array}$$

$$\begin{array}{llll} \sigma * BR(Z\gamma)_e & = 6.8\ ^{+5.9}_{-5.8}\ (stat+syst)\ pb & \sigma * BR(Z\gamma)_\mu & = 13.6^{+11.2}_{-10.1}\ (stat+syst)\ pb \\ \sigma * BR(Z\gamma)_{e+\mu} & = 9.2\ ^{+5.6}_{-5.2}\ (stat+syst)\ pb & \sigma * BR(Z\gamma)_{SM} & = 4.7\ ^{+0.7}_{+0.2}\ (stat+syst)\ pb \end{array}$$

We have also obtained three new results on cross section ratios, which for the combined $e+\mu$ results, along with the previous CDF measurement(s) of the W/Z cross section ratio provide new insight on the SM, and test possible anomalous couplings of the W and Z bosons:

$$\begin{array}{llll} \mathcal{R}(W\gamma/W)_{e+\mu} & = 0.8^{+0.5}_{-0.5}\%\ (stat+syst) & \mathcal{R}(Z\gamma/Z)_{e+\mu} & = 4.3^{+2.5}_{-2.4}\%\ (stat+syst) \\ \mathcal{R}(W\gamma/Z\gamma)_{e+\mu} & = 1.9^{+2.0}_{-1.4}\ \ (stat+syst) & \mathcal{R}(W/Z)_{e+\mu} & = 10.0^{+0.7}_{-0.7}\ \ (stat+syst) \end{array}$$

From the $W\gamma$ and $Z\gamma$ cross section measurements, we obtain limits on anomalous $WW\gamma$ and $ZZ\gamma$ couplings of the W and Z bosons, providing constraints on possible internal (composite) structure for these gauge bosons. For $W\gamma$, from the combined $e+\mu$ result, we obtain limits on $WW\gamma$ anomalous coupling parameters $\Delta\kappa = \kappa - 1$ and λ of

$$\Delta\kappa\ = 0.0^{+5.4}_{-4.9}\ (stat+syst)\ \ (\lambda = 0) \qquad \lambda\ = 0.0^{+2.3}_{-2.4}\ (stat+syst)\ \ (\Delta\kappa = 0)$$

$$\begin{array}{rcccl} -6.6 & < & \Delta\kappa & < & +7.1\ \ (\lambda = 0,\ 95.0\%\ CL) \\ -3.2 & < & \lambda & < & +3.1\ \ (\Delta\kappa = 0,\ 95.0\%\ CL) \end{array}$$

Since the $\Delta\kappa$ and λ parameters are related to the W boson magnetic dipole and electric quadrupole moments, and mean-squared charge radius by

$\mu_W = \mu_W^\circ(2+\Delta\kappa+\lambda) \qquad Q_W = Q_W^\circ(1+\Delta\kappa-\lambda) \qquad < R_W >^2 = \lambda_W^2(1+\Delta\kappa+\lambda)$

where λ_W is the (reduced) Compton wavelength of the W boson, we obtain limits on these additional electromagnetic properties of the W boson:

$$\begin{array}{rcll} \mu_W/\mu_W^\circ & \equiv\ g_W & = 2.0^{+3.7}_{-3.6}\ (stat+syst) & (Q_W/Q_W^\circ = 1) \\ Q_W/Q_W^\circ & \equiv\ q_W & = 1.0^{+5.6}_{-5.3}\ (stat+syst) & (\mu_W/\mu_W^\circ = 2) \\ < R_W >^2/\lambda_W^2 & \equiv\ r_W^2 & = 1.0^{+3.7}_{-3.6}\ (stat+syst) & (Q_W/Q_W^\circ = 1) \end{array}$$

$$\begin{array}{rcccl} -4.8 & < & \mu_W/\mu_W^\circ - 2 \equiv g_W - 2 & < & +4.9\ \ (Q_W/Q_W^\circ = 1,\ 95.0\%\ CL) \\ -7.1 & < & Q_W/Q_W^\circ - 1 \equiv q_W - 1 & < & +7.4\ \ (\mu_W/\mu_W^\circ = 2,\ 95.0\%\ CL) \\ -4.8 & < & < R_W >^2/\lambda_W^2 - 1 \equiv r_W^2 - 1 & < & +4.9\ \ (Q_W/Q_W^\circ = 1,\ 95.0\%\ CL) \end{array}$$

These results probe possible internal structure of the W boson at a distance scale of $\lambda_W \sim 2.5 \times 10^{-3}\ fm$, and are sensitive up to a compositeness scale $\Lambda \sim 1\ TeV$. For $Z\gamma$, from the combined $e + \mu$ result, we obtain limits on $ZZ\gamma$ anomalous coupling parameters h_{30}^Z and h_{40}^Z for three different choices of the compositeness scale Λ, with sensitivity to such anomalous couplings up to $\Lambda \sim 500\ GeV$. These results are also valid for anomalous $Z\gamma\gamma$ couplings.

We are extremely greatful to U. Baur for his enormous help and the extensive use of his Monte Carlo programs. We deeply appreciate the many stimulating discussions we have had with him during the course of this analysis. We also wish to thank our CDF collaborators at the University of Chicago for the loan of their QCD04 tapes, in order to make copies of them for our own use on QCD background studies.

References

[1] S.J. Brodsky, R.W. Brown, Phys. Rev. Lett. **49**, 966 (1982).

[2] R.W. Robinett, Phys Rev **D28**, 1185 (1983).

[3] J. P. Eboli, Angela V. Olinto, Phys. Rev. **D38**, 3461 (1988).

[4] U. Baur and D. Zeppenfeld, Nucl. Phys. **B308**, 127 (1988).

[5] U. Baur, E. L. Berger, Phys Rev **D41**, 1476 (1990); U. Baur, E. L. Berger, to appear in Phys Rev **D** (1993), and FSU-HEP-921030.

[6] U. Baur and D. Zeppenfeld, Phys. Lett. **B201**, 383 (1988).

[7] K. Hagiwara *et al*, Nucl. Phys. **B282**, 253 (1987).

[8] A. Barroso *et al*, Z. Phys. **C28**, 149 1985

[9] J. M. Cornwall, D. N. Levin and G. Tiktopoulos, Phys. Rev. Lett. **30**, 1268 1973; Phys. Rev. **D10**, 1145 (1974); C. H. Llewellyn Smith, Phys. Lett. **46B**, 233 (1973); S. D. Joglekar, Ann. of Phys. **83**, 427 (1974).

[10] G.W. Foster *et al*, Nucl. Instr. and Meth. **269A**, 93 (1988).

[11] F. Abe *et al*, Phys. Rev. Lett. **64**, 152 (1990); F. Abe *et al*, Phys. Rev. **D44**, 29 (1991); P. Derwent *et al*, **CDF-1107**; P. Derwent *et al*, **CDF-1254**; P. Derwent and M. Miller, **CDF-1166**; M. Miller, **CDF-1086**; F. Abe *et al*, Phys. Rev. Lett. **69**, 28 (1992); S. Eno *et al*, **CDF-1349**; S. Eno *et al*, **CDF-1629**; R. Swartz and D. Kardelis, **CDF-1220**; A. Byon *et al*, **CDF-1263**; D.A. Smith and R. Swartz, **CDF-1259**

[12] C. Grosso-Pilcher and S. White, **CDF-1202**.

[13] **CDF-1260**, Cosmic Filtering of Central Muon Events.

[14] G. Peter Lepage, J. Comp. Phys. **27**, 192-202, Academic Press (1978); G. Peter Lepage, CLNS-80/447 (1980).

[15] H. Plothow-Besch, CERN Report W5051, 1992.

[16] C. Campagnari, **CDF-1025**.

[17] F. Abe *et al*, Phys. Rev. Lett. **66**, 2951 (1991); F. Abe *et al*, Phys. Rev. Lett. **67**, 2937 (1991); B. Winer, Ph.D. thesis, University of California at Berkeley (1991); J. Ng, Ph.D. thesis, Harvard University (1991); J. Ng, **CDF-1504**

[18] F. Abe *et al*, Phys. Rev. **D43**, 2070 (1991); F. Abe *et al*, Phys. Rev. Lett. **65**, 2243 (1990); W. Trischuk, Ph.D. thesis, Harvard University (1990); P. Schlabach, Ph.D. thesis, University of Illinois (1990).

[19] S. Errede, "Methodology for the Measurement of $W\gamma$ and $Z\gamma$ in the Muon Channel at CDF", **CDF-1732** (1992).

[20] M. Mangano, "The Unweighting of Matrix Element Monte Carlos", **CDF-1665** (1992).

[21] Barry Wicklund, private communication.

[22] Review of Particle Properties, Phys. Rev. **D45**, III.39, (1992).

[23] U. Baur, S. Errede and J. Ohnemus, "Ratios of $W^{\pm}\gamma$ and $Z\gamma$ Cross Sections: New Tools in Probing the Weak Boson Sector at the Tevatron and the SSC", submitted to Phys. Rev. **D**, March, 1993 and **CDF-2039** and **SDC-93-476**.

[24] J. Alitti, *et al*, Phys. Lett. **B 277**, 194 (1992).

[25] E. Thorndike, CLEO Collaboration, talk presented at the Washington APS meeting, Washington, D.C., unpublished (1993).

[26] U. Baur, private communication, and T. Rizzo, ANL preprint ANL-HEP-PR-93-19.

[27] U. Baur, private communication

[28] O. Adriani, *et al*, Phys. Lett. **B 297**, 469 (1992).

[29] M. Baillargeon and F. Boudjema, CERN Report 92-04, p.178 (1992).

17 Tables

Table 1a: CEM Photon Efficiency Determination

Data Sample	$\epsilon_{ET4<2.0\ GeV}$	$\epsilon_{ET4<1.0\ GeV}$
W_e Random Cones	$95.46 \pm 0.46\%$	$86.26 \pm 0.75\%$
W_μ Random Cones	$95.93 \pm 0.44\%$	$87.57 \pm 0.71\%$
Z_e Random Cones	$95.75 \pm 0.62\%$	$87.66 \pm 0.98\%$
Z_μ Random Cones	$94.49 \pm 1.16\%$	$86.23 \pm 1.69\%$
QFL e $W\gamma$ MC	$98.86 \pm 0.63\%$	$93.61 \pm 1.28\%$
QFL μ $W\gamma$ MC	$99.33 \pm 0.66\%$	$92.93 \pm 1.66\%$
QFL e $Z\gamma$ MC	$97.86 \pm 1.17\%$	$93.59 \pm 1.82\%$
QFL μ $Z\gamma$ MC	$98.33 \pm 0.69\%$	$91.46 \pm 1.38\%$
MinBias Random Cones	$98.57 \pm 0.18\%$	$94.07 \pm 0.35\%$
Jet-20a Random Cones	$99.12 \pm 0.08\%$	$92.34 \pm 0.23\%$
Jet-20b Random Cones	$92.65 \pm 0.22\%$	$81.89 \pm 0.33\%$

Data Sample	$\epsilon_{ET4<2.0\ \Sigma PT4<2.0}$	$\epsilon_{ET4<1.0\ \Sigma PT4<2.0}$
W_e Random Cones	$93.35 \pm 0.55\%$	$84.91 \pm 0.78\%$
W_μ Random Cones	$93.12 \pm 0.55\%$	$85.85 \pm 0.75\%$
Z_e Random Cones	$93.63 \pm 0.74\%$	$86.36 \pm 1.02\%$
Z_μ Random Cones	$91.10 \pm 1.42\%$	$83.90 \pm 1.80\%$
QFL e $W\gamma$ MC	$96.35 \pm 1.01\%$	$92.01 \pm 1.41\%$
QFL μ $W\gamma$ MC	$96.63 \pm 1.22\%$	$90.91 \pm 1.84\%$
QFL e $Z\gamma$ MC	$97.01 \pm 1.34\%$	$92.74 \pm 1.91\%$
QFL μ $Z\gamma$ MC	$94.79 \pm 1.12\%$	$88.75 \pm 1.55\%$
MinBias Random Cones	$97.71 \pm 0.22\%$	$93.52 \pm 0.36\%$
Jet-20a Random Cones	$97.55 \pm 0.13\%$	$91.25 \pm 0.24\%$
Jet-20b Random Cones	$89.30 \pm 0.26\%$	$80.08 \pm 0.34\%$

Data Sample	$\epsilon_{ET4<2.0\ \Sigma PT4<1.0}$	$\epsilon_{ET4<1.0\ \Sigma PT4<1.0}$
W_e Random Cones	$86.84 \pm 0.74\%$	$80.29 \pm 0.87\%$
W_μ Random Cones	$86.90 \pm 0.73\%$	$81.43 \pm 0.84\%$
Z_e Random Cones	$87.66 \pm 0.98\%$	$81.94 \pm 1.14\%$
Z_μ Random Cones	$85.59 \pm 1.72\%$	$79.87 \pm 1.95\%$
QFL e $W\gamma$ MC	$91.32 \pm 1.46\%$	$86.99 \pm 1.72\%$
QFL μ $W\gamma$ MC	$90.57 \pm 1.87\%$	$86.53 \pm 2.15\%$
QFL e $Z\gamma$ MC	$89.74 \pm 2.20\%$	$86.75 \pm 2.43\%$
QFL μ $Z\gamma$ MC	$89.38 \pm 1.51\%$	$84.17 \pm 1.77\%$
MinBias Random Cones	$94.23 \pm 0.34\%$	$90.81 \pm 0.42\%$
Jet-20a Random Cones	$91.62 \pm 0.24\%$	$86.36 \pm 0.29\%$
Jet-20b Random Cones	$81.98 \pm 0.33\%$	$74.84 \pm 0.37\%$

Data Sample	$\epsilon_{ET4<2.0\ \Sigma PT4<2.0\ N3D=0}$	$\epsilon_{ET4<1.0\ \Sigma PT4<2.0\ N3D=0}$
W_e Random Cones	$89.18 \pm 0.68\%$	$81.45 \pm 0.85\%$
W_μ Random Cones	$88.57 \pm 0.69\%$	$82.13 \pm 0.82\%$
Z_e Random Cones	$89.05 \pm 0.93\%$	$82.84 \pm 1.12\%$
Z_μ Random Cones	$87.29 \pm 1.64\%$	$80.72 \pm 1.92\%$
QFL e $W\gamma$ MC	$90.18 \pm 1.54\%$	$86.07 \pm 1.77\%$
QFL μ $W\gamma$ MC	$93.27 \pm 1.63\%$	$87.88 \pm 2.06\%$
QFL e $Z\gamma$ MC	$91.88 \pm 2.00\%$	$87.61 \pm 2.37\%$
QFL μ $Z\gamma$ MC	$91.88 \pm 1.35\%$	$86.46 \pm 1.67\%$
Jet-20a Random Cones	$92.73 \pm 0.22\%$	$86.99 \pm 0.29\%$
Jet-20b Random Cones	$84.18 \pm 0.31\%$	$75.92 \pm 0.36\%$

Data Sample	$\epsilon_{ET4<2.0\ \Sigma PT4<1.0\ N3D=0}$	$\epsilon_{ET4<1.0\ \Sigma PT4<1.0\ N3D=0}$
W_e Random Cones	$83.39 \pm 0.81\%$	$77.46 \pm 0.91\%$
W_μ Random Cones	$83.22 \pm 0.80\%$	$78.18 \pm 0.89\%$
Z_e Random Cones	$84.31 \pm 1.08\%$	$79.25 \pm 1.20\%$
Z_μ Random Cones	$82.42 \pm 1.86\%$	$77.33 \pm 2.03\%$
QFL e $W\gamma$ MC	$85.84 \pm 1.78\%$	$81.74 \pm 1.76\%$
QFL μ $W\gamma$ MC	$87.54 \pm 2.08\%$	$83.84 \pm 2.30\%$
QFL e $Z\gamma$ MC	$85.04 \pm 2.54\%$	$82.05 \pm 2.72\%$
QFL μ $Z\gamma$ MC	$87.08 \pm 1.64\%$	$82.50 \pm 1.84\%$
Jet-20a Random Cones	$87.53 \pm 0.28\%$	$82.70 \pm 0.32\%$
Jet-20b Random Cones	$77.87 \pm 0.35\%$	$71.35 \pm 0.38\%$

Table 1b: CEM Photon Efficiency Determination (cont.)

Data Sample	$\epsilon_{Had/EM<ABW}$	$\epsilon_{L_{shr}<0.5}$	$\epsilon_{\chi^2_{stp},\chi^2_{wir}<20}$
5 *GeV* e Test Beam	$98.88 \pm 0.17\%$	$99.89 \pm 0.06\%$	$97.28 \pm 0.25\%$
10 *GeV* e Test Beam	$99.64 \pm 0.13\%$	$98.84 \pm 0.38\%$	$96.24 \pm 0.36\%$
50 *GeV* e Test Beam	$98.02 \pm 0.25\%$	$99.94 \pm 0.06\%$	$99.20 \pm 0.16\%$
QFL e $W\gamma$ MC	$94.15 \pm 1.35\%$	$99.72 \pm 0.25\%$	$99.01 \pm 0.54\%$
QFL μ $W\gamma$ MC	$97.04 \pm 1.22\%$	$100.00^{+0.00}_{-0.35}\%$	$98.09 \pm 1.05\%$
QFL e $Z\gamma$ MC	$93.95 \pm 1.83\%$	$100.00^{+0.00}_{-0.45}\%$	$96.04 \pm 1.63\%$
QFL μ $Z\gamma$ MC	$95.24 \pm 1.13\%$	$100.00^{+0.00}_{-0.22}\%$	$98.33 \pm 0.75\%$

Data Sample	$\epsilon_{no\ 2^{nd}\ CES>1\ GeV}$	$\epsilon_{\text{product}}$
5 *GeV* e Test Beam	$97.50 \pm 0.52\%$	$93.68 \pm 0.57\%$
10 *GeV* e Test Beam	$94.90 \pm 0.76\%$	$89.95 \pm 0.84\%$
18 *GeV* e Test Beam	$87.58 \pm 1.43\%$	–
30 *GeV* e Test Beam	$85.71 \pm 1.99\%$	–
50 *GeV* e Test Beam	$80.80 \pm 1.43\%$	$78.52 \pm 1.15\%$
QFL e $W\gamma$ MC	$94.15 \pm 1.24\%$	$87.52 \pm 1.22\%$
QFL μ $W\gamma$ MC	$94.55 \pm 1.61\%$	$90.00 \pm 2.01\%$
QFL e $Z\gamma$ MC	$94.45 \pm 2.44\%$	$88.39 \pm 1.76\%$
QFL μ $Z\gamma$ MC	$94.67 \pm 1.23\%$	$88.66 \pm 1.62\%$

Table 1c: Overall CEM Photon Efficiency Determination

Data Sample	$\epsilon_{ET4<2.0\ \Sigma PT4<2.0}$	$\epsilon_{ET4<1.0\ \Sigma PT4<2.0}$
W_e Random Cones	$80.90 \pm 0.67\%$	$73.89 \pm 0.84\%$
W_μ Random Cones	$81.62 \pm 0.57\%$	$75.10 \pm 0.73\%$
Z_e Random Cones	$80.80 \pm 0.95\%$	$75.16 \pm 1.10\%$
Z_μ Random Cones	$81.62 \pm 0.57\%$	$75.10 \pm 0.73\%$
QFL e $W\gamma$ MC	$78.54 \pm 2.08\%$	$75.11 \pm 2.18\%$
QFL μ $W\gamma$ MC	$84.18 \pm 2.29\%$	$79.46 \pm 2.51\%$
QFL e $Z\gamma$ MC	$85.42 \pm 1.80\%$	$80.41 \pm 2.01\%$
QFL μ $Z\gamma$ MC	$81.46 \pm 1.88\%$	$76.67 \pm 2.03\%$

Data Sample	$\epsilon_{ET4<2.0\ \Sigma PT4<1.0}$	$\epsilon_{ET4<1.0\ \Sigma PT4<1.0}$
W_e Random Cones	$76.07 \pm 0.78\%$	$70.27 \pm 0.92\%$
W_μ Random Cones	$75.41 \pm 2.36\%$	$71.91 \pm 2.49\%$
Z_e Random Cones	$76.49 \pm 1.07\%$	$71.91 \pm 1.17\%$
Z_μ Random Cones	$75.90 \pm 0.72\%$	$70.98 \pm 0.81\%$
QFL e $W\gamma$ MC	$75.34 \pm 2.17\%$	$71.92 \pm 2.26\%$
QFL μ $W\gamma$ MC	$79.80 \pm 2.50\%$	$76.09 \pm 2.64\%$
QFL e $Z\gamma$ MC	$81.32 \pm 1.97\%$	$77.22 \pm 2.11\%$
QFL μ $Z\gamma$ MC	$77.08 \pm 2.02\%$	$73.13 \pm 2.13\%$

Table 2a: W and Z Acceptances for e and μ $W\gamma$ and $Z\gamma$

Acceptance	Electron	Muon
A_W	$27.62 \pm 0.06\%$	$16.24 \pm 0.05\%$
A_Z	$28.57 \pm 0.07\%$	$13.45 \pm 0.05\%$
A_{oo}	$12.76 \pm 0.05\%$	$4.22 \pm 0.03\%$
A_{ox}	$13.18 \pm 0.05\%$	$9.24 \pm 0.04\%$
A_{oy}	$2.62 \pm 0.02\%$	$- - -$
A_{ZW}	$9.87 \pm 0.04\%$	$16.24 \pm 0.05\%$

Table 2b: Photon Acceptances for e and μ $W\gamma$

$W\gamma$	Electron	Muon
f^{γ}_{cem}	$46.98 \pm 0.07\%$	$46.81 \pm 0.07\%$
f^{γ}_{pem}	$36.59 \pm 0.07\%$	$36.32 \pm 0.07\%$
f^{γ}_{fem}	$15.12 \pm 0.05\%$	$15.30 \pm 0.05\%$
f'^{γ}_{cem}	$48.19 \pm 0.34\%$	$50.93 \pm 0.49\%$
f'^{γ}_{pem}	$32.00 \pm 0.32\%$	$31.22 \pm 0.46\%$
f'^{γ}_{fem}	$19.81 \pm 0.27\%$	$17.86 \pm 0.31\%$
A^{γ}_{cem}	$13.53 \pm 0.12\%$	$13.12 \pm 0.15\%$
A^{γ}_{pem}	$19.27 \pm 0.21\%$	$21.20 \pm 0.30\%$
A^{γ}_{fem}	$24.12 \pm 0.32\%$	$21.54 \pm 0.41\%$
A'^{γ}_{cem}	$77.93 \pm 0.24\%$	$75.73 \pm 0.33\%$
A'^{γ}_{pem}	$56.88 \pm 0.44\%$	$58.99 \pm 0.61\%$
A'^{γ}_{fem}	$81.45 \pm 0.54\%$	$78.76 \pm 0.78\%$

Table 2c: Photon Acceptances for e and μ $Z\gamma$

$Z\gamma$	Electron	Muon
f^{γ}_{coo}	$70.83 \pm 0.17\%$	$75.53 \pm 0.29\%$
f^{γ}_{poo}	$22.83 \pm 0.16\%$	$18.58 \pm 0.26\%$
f^{γ}_{foo}	$5.85 \pm 0.09\%$	$5.48 \pm 0.15\%$
f^{γ}_{cox}	$50.80 \pm 0.17\%$	$71.54 \pm 0.20\%$
f^{γ}_{pox}	$39.84 \pm 0.17\%$	$22.41 \pm 0.19\%$
f^{γ}_{fox}	$8.81 \pm 0.10\%$	$5.64 \pm 0.10\%$
f^{γ}_{coy}	$39.52 \pm 0.24\%$	$0.00 \pm 0.00\%$
f^{γ}_{poy}	$35.66 \pm 0.23\%$	$0.00 \pm 0.00\%$
f^{γ}_{foy}	$23.77 \pm 0.21\%$	$0.00 \pm 0.00\%$
$f^{\prime\gamma}_{coo}$	$69.55 \pm 0.43\%$	$72.60 \pm 0.73\%$
$f^{\prime\gamma}_{poo}$	$23.28 \pm 0.40\%$	$21.06 \pm 0.67\%$
$f^{\prime\gamma}_{foo}$	$7.16 \pm 0.24\%$	$6.34 \pm 0.40\%$
$f^{\prime\gamma}_{cox}$	$55.45 \pm 0.47\%$	$68.40 \pm 0.50\%$
$f^{\prime\gamma}_{pox}$	$31.88 \pm 0.45\%$	$23.03 \pm 0.45\%$
$f^{\prime\gamma}_{fox}$	$12.67 \pm 0.32\%$	$8.57 \pm 0.30\%$
$f^{\prime\gamma}_{coy}$	$33.66 \pm 1.14\%$	$0.00 \pm 0.00\%$
$f^{\prime\gamma}_{poy}$	$45.56 \pm 1.20\%$	$0.00 \pm 0.00\%$
$f^{\prime\gamma}_{foy}$	$12.67 \pm 0.98\%$	$0.00 \pm 0.00\%$
A^{γ}_{coo}	$18.94 \pm 0.19\%$	$18.69 \pm 0.32\%$
A^{γ}_{poo}	$19.77 \pm 0.35\%$	$22.12 \pm 0.70\%$
A^{γ}_{foo}	$22.90 \pm 0.71\%$	$21.75 \pm 1.27\%$
A^{γ}_{cox}	$20.26 \pm 0.23\%$	$19.44 \pm 0.23\%$
A^{γ}_{pox}	$14.48 \pm 0.23\%$	$20.74 \pm 0.41\%$
A^{γ}_{fox}	$24.14 \pm 0.57\%$	$28.69 \pm 0.90\%$
A^{γ}_{coy}	$14.74 \pm 0.56\%$	$0.00 \pm 0.00\%$
A^{γ}_{poy}	$16.47 \pm 0.53\%$	$0.00 \pm 0.00\%$
A^{γ}_{foy}	$12.50 \pm 0.62\%$	$0.00 \pm 0.00\%$
$A^{\prime\gamma}_{coo}$	$77.15 \pm 0.31\%$	$74.75 \pm 0.53\%$
$A^{\prime\gamma}_{poo}$	$51.60 \pm 0.68\%$	$54.79 \pm 1.32\%$
$A^{\prime\gamma}_{foo}$	$80.52 \pm 1.28\%$	$89.45 \pm 2.03\%$
$A^{\prime\gamma}_{cox}$	$74.43 \pm 0.40\%$	$75.71 \pm 0.37\%$
$A^{\prime\gamma}_{pox}$	$60.46 \pm 0.51\%$	$52.90 \pm 0.80\%$
$A^{\prime\gamma}_{fox}$	$84.82 \pm 0.87\%$	$84.98 \pm 1.25\%$
$A^{\prime\gamma}_{coy}$	$69.76 \pm 1.35\%$	$0.00 \pm 0.00\%$
$A^{\prime\gamma}_{poy}$	$59.14 \pm 1.22\%$	$0.00 \pm 0.00\%$
$A^{\prime\gamma}_{foy}$	$81.28 \pm 1.66\%$	$0.00 \pm 0.00\%$

Table 2d: Electron Efficiencies for $W\gamma$ and $Z\gamma$

$\mathcal{L}_e \cdot dt$	$4.05 \pm 0.28\ pb^{-1}$	Integrated Luminosity
F_{DY}	0.985 ± 0.005	$70 < M_Z < 110\ GeV/c^2$
ϵ_{zvx}	0.954 ± 0.001	$\lvert Z_{vtx}\rvert < 60\ cm$
ϵ_{iso}^{CEM}	0.960 ± 0.010	Electron Isolation (R=0.4)
$\epsilon_{Had/EM}^{CEM}$	0.990 ± 0.010	$Had/EM < ABW$
$\epsilon_{\chi^2_{stp}}$	0.970 ± 0.010	$\chi^2_{stp} < 15$
$\epsilon_{L_{shr}}^{CEM}$	0.970 ± 0.010	$L_{shr} < 0.2$
$\epsilon_{E/P}^{T}$	0.930 ± 0.010	Tight CEM E/P < 1.5 Cut
$\epsilon_{E/P}^{L}$	0.970 ± 0.010	Loose CEM E/P < 2.0 Cut
ϵ_{trk}^{CEM}	1.000 ± 0.001	CTC Tracking
ϵ_{dz}^{CEM}	0.980 ± 0.010	$dz < 3.0\ cm$ Matching Cut
ϵ_{dx}^{CEM}	0.970 ± 0.010	$dx < 1.5\ cm$ Matching Cut
ϵ_{iso}^{PEM}	0.960 ± 0.010	Electron Isolation (R=0.4)
$\epsilon_{Had/EM}^{PEM}$	0.990 ± 0.010	$Had/EM < ABW$
$\epsilon_{\chi^2_{3x3}}$	0.940 ± 0.010	$\chi^2_{3x3} < 20$
ϵ_{vtpc}^{PEM}	0.930 ± 0.020	VTPC Occupancy > 0.5 cut
ϵ_{iso}^{FEM}	0.910 ± 0.010	Electron Isolation (R=0.4)
$\epsilon_{Had/EM}^{FEM}$	1.000 ± 0.010	$Had/EM < ABW$
$T = \epsilon_{L1} \cdot \epsilon_{L2} \cdot \epsilon_{L3}$	0.973 ± 0.005	Fiducial Electron Trigger

Table 2e: Muon Efficiencies for $W\gamma$ and $Z\gamma$

$\mathcal{L}_\mu \cdot dt$	$3.54 \pm 0.24\ pb^{-1}$	Integrated Luminosity
F_{DY}	0.970 ± 0.002	$65 < M_Z < 115\ GeV/c^2$
ϵ_{zvx}	0.954 ± 0.001	$\lvert Z_{vtx}\rvert < 60\ cm$
ϵ_{dx}	0.960 ± 0.010	CTC-CMU Track-Stub Match
ϵ_{mi}	$0.987 + 0.003 - 0.004$	Minimum Ionizing Energy
ϵ_{iso}	0.980 ± 0.010	Muon Isolation (R=0.4)
ϵ_{trk}	0.987 ± 0.010	CTC Re-Tracking
ϵ_{cmuo}	$0.986 + 0.012 - 0.033$	CMU Stub Finding
ϵ_{cos}	0.997 ± 0.002	Cosmic Ray Filter
ϵ_{L1}	0.934 ± 0.004	Level-1 Trigger
ϵ_{L2}	$0.972 + 0.015 - 0.027$	Level-2 Trigger
ϵ_{L3}	$1.000 + 0.000 - 0.028$	Level-3 Trigger
$T = \epsilon_{L1} \cdot \epsilon_{L2} \cdot \epsilon_{L3}$	0.910 ± 0.002	Fiducial Muon Trigger
$\epsilon_{S1} = \epsilon_{mi} \cdot \epsilon_{trk} \cdot \epsilon_{cmuo}$	0.960 ± 0.035	Fiducial Silver Muon
$\epsilon_{S2} = \epsilon_{mi} \cdot \epsilon_{trk}$	0.974 ± 0.011	Non-Fiducial Silver Muon
$\epsilon_G = \epsilon_{S1} \cdot \epsilon_{iso} \cdot \epsilon_{trk}$	0.904 ± 0.038	Fiducial Golden Muon

Table 3a: Electron and Muon $W\gamma$ MC Predictions

	Electron	Muon
Baur Fast $W\gamma$ MC ($\epsilon^{\gamma}_{CEM} \equiv 80\%$):	4.56 ± 0.43	2.54 ± 0.24
Baur QFL $W\gamma$ MC: $ET4 < 2$, $\sum PT4 < 2$	4.27 ± 0.38	2.65 ± 0.25
Baur QFL $W\gamma$ MC: $ET4 < 2$, $\sum PT4 < 1$	4.10 ± 0.36	2.52 ± 0.24
Baur QFL $W\gamma$ MC: $ET4 < 1$, $\sum PT4 < 2$	4.08 ± 0.36	2.51 ± 0.24
Baur QFL $W\gamma$ MC: $ET4 < 1$, $\sum PT4 < 1$	3.91 ± 0.35	2.40 ± 0.23

Table 3b: Electron and Muon $Z\gamma$ MC Predictions

	Electron	Muon
Baur Fast $Z\gamma$ MC ($\epsilon^{\gamma}_{CEM} \equiv 80\%$):	1.15 ± 0.11	0.67 ± 0.07
Baur Fast $Z + DY\gamma$ MC ($\epsilon^{\gamma}_{CEM} \equiv 80\%$):	1.19 ± 0.11	0.68 ± 0.06
Baur QFL $Z\gamma$ MC: $ET4 < 2$, $\sum PT4 < 2$	1.41 ± 0.14	0.75 ± 0.10
Baur QFL $Z\gamma$ MC: $ET4 < 2$, $\sum PT4 < 1$	1.31 ± 0.14	0.73 ± 0.10
Baur QFL $Z\gamma$ MC: $ET4 < 1$, $\sum PT4 < 2$	1.34 ± 0.14	0.68 ± 0.10
Baur QFL $Z\gamma$ MC: $ET4 < 1$, $\sum PT4 < 1$	1.26 ± 0.13	0.67 ± 0.09

Table 4a: QCD γ Background Estimates for e and μ $W\gamma$

Overall CEM Photon Cut	Electron	Muon
Jet-20 ($\Delta R_{JJ} > 1.4$) $ET4 < 2$, $\sum PT4 < 2$	3.57 ± 0.81	1.87 ± 0.42
Jet-20 ($\Delta R_{JJ} > 1.4$) $ET4 < 2$, $\sum PT4 < 1$	2.63 ± 0.70	1.39 ± 0.37
Jet-20 ($\Delta R_{JJ} > 1.4$) $ET4 < 1$, $\sum PT4 < 2$	2.12 ± 0.65	1.12 ± 0.33
Jet-20 ($\Delta R_{JJ} > 1.4$) $ET4 < 1$, $\sum PT4 < 1$	1.92 ± 0.61	1.01 ± 0.31
VecBos ($\Delta R_{\ell J} > 0.7$) $ET4 < 2$, $\sum PT4 < 2$	2.09 ± 0.63	1.03 ± 0.39
VecBos ($\Delta R_{\ell J} > 0.7$) $ET4 < 2$, $\sum PT4 < 1$	1.31 ± 0.55	0.76 ± 0.34
VecBos ($\Delta R_{\ell J} > 0.7$) $ET4 < 1$, $\sum PT4 < 2$	0.94 ± 0.47	0.62 ± 0.31
VecBos ($\Delta R_{\ell J} > 0.7$) $ET4 < 1$, $\sum PT4 < 1$	0.67 ± 0.43	0.56 ± 0.29

Table 4b: QCD γ Background Estimates for e and μ $Z\gamma$

Overall CEM Photon Cut	Electron	Muon
Jet-20 ($\Delta R_{JJ} > 1.4$) $ET4 < 2$, $\sum PT4 < 2$	0.30 ± 0.07	0.11 ± 0.03
Jet-20 ($\Delta R_{JJ} > 1.4$) $ET4 < 2$, $\sum PT4 < 1$	0.23 ± 0.07	0.08 ± 0.02
Jet-20 ($\Delta R_{JJ} > 1.4$) $ET4 < 1$, $\sum PT4 < 2$	0.18 ± 0.06	0.06 ± 0.02
Jet-20 ($\Delta R_{JJ} > 1.4$) $ET4 < 1$, $\sum PT4 < 1$	0.17 ± 0.06	0.06 ± 0.02
VecBos ($\Delta R_{\ell J} > 0.7$) $ET4 < 2$, $\sum PT4 < 2$	0.16 ± 0.07	0.08 ± 0.05
VecBos ($\Delta R_{\ell J} > 0.7$) $ET4 < 2$, $\sum PT4 < 1$	0.08 ± 0.04	0.05 ± 0.04
VecBos ($\Delta R_{\ell J} > 0.7$) $ET4 < 1$, $\sum PT4 < 2$	0.08 ± 0.04	0.08 ± 0.05
VecBos ($\Delta R_{\ell J} > 0.7$) $ET4 < 1$, $\sum PT4 < 1$	0.06 ± 0.02	0.04 ± 0.04

Table 5a: Additional Backgrounds to e and μ $W\gamma$

Background Process $\epsilon^{\gamma}_{CEM} \equiv 80\%$	Electron	Muon
$Z+\gamma \rightarrow$ "$W+\gamma$": No 2^{nd} Leg Cut	0.55 ± 0.05	0.73 ± 0.07
$Z+\gamma \rightarrow$ "$W+\gamma$": w/ 2^{nd} Leg Cut	0.12 ± 0.02	0.40 ± 0.07
$Z+Jet \rightarrow$ "$W+\gamma$": No 2^{nd} Leg Cut	0.11 ± 0.01	0.14 ± 0.02
$Z+Jet \rightarrow$ "$W+\gamma$": w/ 2^{nd} Leg Cut	0.02 ± 0.01	0.04 ± 0.01
$(W \rightarrow \tau\nu_{\tau}, \tau \rightarrow \ell\nu_{\ell}\nu_{\tau}) + \gamma$	0.11 ± 0.01	0.06 ± 0.01

Table 5b: Summary of Backgrounds to Electron $W\gamma$

Overall CEM Photon Cut	N^{W}_{QCD}	$N^{Z\gamma} + N^{Z\gamma}_{QCD}$	$N^{W\tau e}$
$ET4 < 2$, $\sum PT4 < 2$	$3.57 \pm 0.81 \pm 1.47$	$0.14 \pm 0.02 \pm 0.07$	0.11 ± 0.01
$ET4 < 2$, $\sum PT4 < 1$	$2.63 \pm 0.70 \pm 1.32$	$0.13 \pm 0.02 \pm 0.09$	0.10 ± 0.01
$ET4 < 1$, $\sum PT4 < 2$	$2.12 \pm 0.65 \pm 1.18$	$0.13 \pm 0.02 \pm 0.09$	0.10 ± 0.01
$ET4 < 1$, $\sum PT4 < 1$	$1.92 \pm 0.61 \pm 1.25$	$0.12 \pm 0.02 \pm 0.05$	0.09 ± 0.01

Table 5c: Summary of Backgrounds to Muon $W\gamma$

Overall CEM Photon Cut	N^{W}_{QCD}	$N^{Z\gamma} + N^{Z\gamma}_{QCD}$	$N^{W\tau\mu}$
$ET4 < 2$, $\sum PT4 < 2$	$1.87 \pm 0.42 \pm 0.84$	$0.44 \pm 0.07 \pm 0.12$	0.06 ± 0.01
$ET4 < 2$, $\sum PT4 < 1$	$1.39 \pm 0.37 \pm 0.63$	$0.43 \pm 0.07 \pm 0.12$	0.05 ± 0.01
$ET4 < 1$, $\sum PT4 < 2$	$1.12 \pm 0.33 \pm 0.50$	$0.43 \pm 0.07 \pm 0.09$	0.05 ± 0.01
$ET4 < 1$, $\sum PT4 < 1$	$1.01 \pm 0.31 \pm 0.45$	$0.42 \pm 0.07 \pm 0.11$	0.05 ± 0.01

Table 5d: Summary of Backgrounds to Electron $Z\gamma$

Overall CEM Photon Cut	N^{Z}_{QCD}
$ET4 < 2$, $\sum PT4 < 2$	$0.30 \pm 0.07 \pm 0.14$
$ET4 < 2$, $\sum PT4 < 1$	$0.23 \pm 0.07 \pm 0.12$
$ET4 < 1$, $\sum PT4 < 2$	$0.18 \pm 0.06 \pm 0.10$
$ET4 < 1$, $\sum PT4 < 1$	$0.17 \pm 0.06 \pm 0.11$

Table 5e: Summary of Backgrounds to Muon $Z\gamma$

Overall CEM Photon Cut	N^{Z}_{QCD}
$ET4 < 2$, $\sum PT4 < 2$	$0.11 \pm 0.03 \pm 0.04$
$ET4 < 2$, $\sum PT4 < 1$	$0.08 \pm 0.02 \pm 0.04$
$ET4 < 1$, $\sum PT4 < 2$	$0.06 \pm 0.02 \pm 0.03$
$ET4 < 1$, $\sum PT4 < 1$	$0.07 \pm 0.02 \pm 0.03$

Table 6a: Observed # of e and μ $W\gamma$ Candidates

Overall CEM Photon Cut	Electron	Muon
$ET4 < 2$, $\sum PT4 < 2$	8	5
$ET4 < 2$, $\sum PT4 < 1$	6	5
$ET4 < 1$, $\sum PT4 < 2$	7	2
$ET4 < 1$, $\sum PT4 < 1$	5	2

Table 6b: Observed # of e and μ $Z\gamma$ Candidates

Overall CEM Photon Cut	Electron	Muon
$ET4 < 2$, $\sum PT4 < 2$	2	2
$ET4 < 2$, $\sum PT4 < 1$	2	2
$ET4 < 1$, $\sum PT4 < 2$	2	2
$ET4 < 1$, $\sum PT4 < 1$	2	2

Table 7a: Run # – Event # of e and μ $W\gamma$ Candidates

	Electron	Muon
1	16801 – 6582	18435 – 606
2	16807 – 4706	19177 – 8534
3	17467 – 15981	19391 – 43073
4	17529 – 442	19629 – 39980
5	17886 – 1796	19932 – 53074
6	18720 – 20145	
7	19430 – 20694	
8	19882 – 38400	

Table 7b: Run # – Event # of e and μ $Z\gamma$ Candidates

	Electron	Muon
1	17025-5219	20361-6869
2	18170-14254	20389-23545

Table 7c: Run # – Event # of e and μ 1-Legged $Z\gamma$ Candidates

	Electron	Muon
1	18143-21126	17470-9248
2		19125-169853

Table 8a: Kinematic Properties of Electron $W\gamma$ Candidates

	Run # Event #	E_T^γ (GeV)	Q_W	M_T^W (GeV)	$\Delta R_{e\gamma}$
1	16801 – 6582	5.17	−1	68.3	1.28
2	16807 – 4706	8.65	+1	63.8	0.84
3	17467 – 15981	14.43	−1	59.2	0.80
4	17529 – 442	5.04	−1	60.8	2.01
5	17886 – 1796	5.04	−1	83.2	2.53
6	18720 – 20145	12.29	+1	68.8	0.76
7	19430 – 20694	7.44	−1	78.4	0.87
8	19882 – 38400	7.04	+1	85.6	1.10

Table 8b: Kinematic Properties of Muon $W\gamma$ Candidates

	Run # Event #	E_T^γ (GeV)	Q_W	M_T^W (GeV)	$\Delta R_{\mu\gamma}$
1	18435 – 606	7.02	−1	50.5	0.93
2	19177 – 8534	14.71	−1	76.2	1.44
3	19391 – 43073	20.01	+1	45.0	1.06
4	19629 – 39980	5.22	+1	79.6	3.15
5	19932 – 53074	23.58	−1	70.3	2.22

Table 8c: Kinematic Properties of Electron $Z\gamma$ Candidates

	Run # Event #	E_T^γ (GeV)	$M_{e^+e^-}$ (GeV)	$M_{Z\gamma}$ (GeV)	$\Delta R_{e\gamma}$
1	17025-5219	13.47	91.0	104.6	1.50
2	18170-14254	5.44	82.0	88.2	0.88

Table 8d: Kinematic Properties of Muon $Z\gamma$ Candidates

	Run # Event #	E_T^γ (GeV)	$M_{\mu^+\mu^-}$ (GeV)	$M_{Z\gamma}$ (GeV)	$\Delta R_{\mu\gamma}$
3	20361-6869	6.40	78.5	84.8	0.71
4	20389-23545	7.12	84.0	91.3	1.27

Table 9a: # of Signal e and μ $W\gamma$ Candidates

Overall CEM Photon Cut	Electron	Muon
$ET4 < 2,\ \sum PT4 < 2$	$4.19^{+2.95\ +1.47}_{-2.95\ -1.47}$	$2.63^{+2.28\ +0.86}_{-2.29\ -0.85}$
$ET4 < 2,\ \sum PT4 < 1$	$3.13^{+2.55\ +1.33}_{-2.57\ -1.32}$	$3.13^{+2.28\ +0.63}_{-2.29\ -0.64}$
$ET4 < 1,\ \sum PT4 < 2$	$4.65^{+2.74\ +1.19}_{-2.73\ -1.18}$	$0.40^{+1.49\ +0.51}_{-1.49\ -0.51}$
$ET4 < 1,\ \sum PT4 < 1$	$2.86^{+2.33\ +1.25}_{-2.32\ -1.25}$	$0.52^{+1.47\ +0.47}_{-1.48\ -0.46}$

Table 9b: # of Signal e and μ $Z\gamma$ Candidates

Overall CEM Photon Cut	Electron	Muon
$ET4 < 2,\ \sum PT4 < 2$	$1.70^{+1.41\ +0.14}_{-1.42\ -0.14}$	$1.89^{+1.42\ +0.05}_{-1.41\ -0.05}$
$ET4 < 2,\ \sum PT4 < 1$	$1.77^{+1.42\ +0.12}_{-1.42\ -0.11}$	$1.92^{+1.42\ +0.04}_{-1.41\ -0.03}$
$ET4 < 1,\ \sum PT4 < 2$	$1.82^{+1.42\ +0.10}_{-1.40\ -0.10}$	$1.93^{+1.43\ +0.03}_{-1.40\ -0.02}$
$ET4 < 1,\ \sum PT4 < 1$	$1.83^{+1.41\ +0.11}_{-1.42\ -0.12}$	$1.94^{+1.42\ +0.04}_{-1.41\ -0.03}$

Table 10a: e and μ $\sigma * BR(W+\gamma)$ Results

$\sigma * BR(W+\gamma)$ (pb)	Electron	Muon
Baur Fast $W\gamma$ MC ($\epsilon^{\gamma}_{CEM} \equiv 80\%$):	18.8 ± 0.3	19.2 ± 0.4
$ET4 < 2,\ \sum PT4 < 2$	$17.0^{+12.0\ +1.5\ +6.0}_{-12.0\ -1.2\ -6.0}$	$19.4^{+16.8\ +2.2\ +6.2}_{-16.9\ -1.2\ -6.3}$
$ET4 < 2,\ \sum PT4 < 1$	$13.5^{+11.0\ +1.2\ +5.7}_{-11.0\ -1.0\ -5.7}$	$24.5^{+17.9\ +2.9\ +5.0}_{-17.9\ -1.4\ -5.0}$
$ET4 < 1,\ \sum PT4 < 2$	$20.1^{+11.8\ +1.9\ +5.1}_{-11.9\ -1.5\ -5.1}$	$3.1^{+11.6\ +0.4\ +4.0}_{-11.6\ -0.2\ -4.0}$
$ET4 < 1,\ \sum PT4 < 1$	$13.1^{+10.7\ +1.3\ +5.7}_{-10.6\ -0.9\ -5.7}$	$4.3^{+12.2\ +0.5\ +3.8}_{-12.3\ -0.3\ -3.9}$
$ET4 < 2,\ \sum PT4 < 2$ (68.3% $SS\ CL$)	< 24.5	< 30.4
$ET4 < 2,\ \sum PT4 < 1$ (68.3% $SS\ CL$)	< 20.8	< 34.8
$ET4 < 1,\ \sum PT4 < 2$ (68.3% $SS\ CL$)	< 26.7	< 14.6
$ET4 < 1,\ \sum PT4 < 1$ (68.3% $SS\ CL$)	< 20.3	< 15.7
$ET4 < 2,\ \sum PT4 < 2$ (90.0% $SS\ CL$)	< 35.9	< 46.4
$ET4 < 2,\ \sum PT4 < 1$ (90.0% $SS\ CL$)	< 31.4	< 51.8
$ET4 < 1,\ \sum PT4 < 2$ (90.0% $SS\ CL$)	< 38.1	< 25.0
$ET4 < 1,\ \sum PT4 < 1$ (90.0% $SS\ CL$)	< 30.6	< 26.7
$ET4 < 2,\ \sum PT4 < 2$ (95.0% $SS\ CL$)	< 41.5	< 54.3
$ET4 < 2,\ \sum PT4 < 1$ (95.0% $SS\ CL$)	< 36.6	< 60.1
$ET4 < 1,\ \sum PT4 < 2$ (95.0% $SS\ CL$)	< 43.6	< 30.4
$ET4 < 1,\ \sum PT4 < 1$ (95.0% $SS\ CL$)	< 35.7	< 32.5

Table 10b: e and μ $\sigma * BR(Z+\gamma)$ Results

$\sigma * BR(Z+\gamma)$ (pb)	Electron	Muon
Baur Fast $Z\gamma$ MC ($\epsilon^{\gamma}_{CEM} \equiv 80\%$):	4.6 ± 0.1	4.7 ± 0.1
$ET4 < 2,\ \sum PT4 < 2$	$6.8^{+5.7\ +0.6\ +0.5}_{-5.7\ -0.5\ -0.6}$	$13.6^{+10.1\ +1.6\ +0.3}_{-10.1\ -0.6\ -0.3}$
$ET4 < 2,\ \sum PT4 < 1$	$7.5^{+6.0\ +0.7\ +0.5}_{-6.0\ -0.5\ -0.5}$	$14.6^{+10.8\ +1.8\ +0.3}_{-10.7\ -0.7\ -0.3}$
$ET4 < 1,\ \sum PT4 < 2$	$7.8^{+6.1\ +0.7\ +0.4}_{-6.1\ -0.5\ -0.4}$	$14.8^{+10.8\ +1.8\ +0.3}_{-10.7\ -0.7\ -0.2}$
$ET4 < 1,\ \sum PT4 < 1$	$8.3^{+6.4\ +0.8\ +0.4}_{-6.4\ -0.5\ -0.4}$	$15.7^{+11.5\ +1.9\ +0.3}_{-11.4\ -0.7\ -0.2}$
$ET4 < 2,\ \sum PT4 < 2$ (68.3% $SS\ CL$)	< 10.4	< 20.4
$ET4 < 2,\ \sum PT4 < 1$ (68.3% $SS\ CL$)	< 11.3	< 21.8
$ET4 < 1,\ \sum PT4 < 2$ (68.3% $SS\ CL$)	< 11.5	< 22.0
$ET4 < 1,\ \sum PT4 < 1$ (68.3% $SS\ CL$)	< 12.2	< 23.3
$ET4 < 2,\ \sum PT4 < 2$ (90.0% $SS\ CL$)	< 15.4	< 29.5
$ET4 < 2,\ \sum PT4 < 1$ (90.0% $SS\ CL$)	< 16.6	< 31.5
$ET4 < 1,\ \sum PT4 < 2$ (90.0% $SS\ CL$)	< 16.9	< 31.8
$ET4 < 1,\ \sum PT4 < 1$ (90.0% $SS\ CL$)	< 17.9	< 33.7
$ET4 < 2,\ \sum PT4 < 2$ (95.0% $SS\ CL$)	< 18.2	< 34.7
$ET4 < 2,\ \sum PT4 < 1$ (95.0% $SS\ CL$)	< 19.6	< 36.9
$ET4 < 1,\ \sum PT4 < 2$ (95.0% $SS\ CL$)	< 19.9	< 37.2
$ET4 < 1,\ \sum PT4 < 1$ (95.0% $SS\ CL$)	< 21.1	< 39.4

Table 11a: Summary of $W\gamma$ and $Z\gamma$ Results

Channel	N_{obs}	$\sum N_{bkgnd}$	N_{signal}	N^{SM}_{pred}
$e\ W\gamma$	8	$3.8 \pm 0.8 \pm 1.5$	$4.2 \pm 2.9 \pm 1.5$	4.6 ± 0.4
$\mu\ W\gamma$	5	$2.2 \pm 0.4 \pm 0.9$	$2.6 \pm 2.3 \pm 0.8$	2.5 ± 0.2
$e\ Z\gamma$	2	$0.3 \pm 0.1 \pm 0.1$	$1.7 \pm 1.4 \pm 0.1$	1.2 ± 0.1
$\mu\ Z\gamma$	2	$0.1 \pm 0.1 \pm 0.1$	$1.9 \pm 1.4 \pm 0.1$	0.7 ± 0.1

Table 11b: Summary of $\sigma * BR(W+\gamma)$ and $\sigma * BR(Z+\gamma)$ Results

Channel	$\sigma \cdot B_{expt}$ (pb)	$\sigma \cdot B^{SM}_{pred}$ (pb)
e $W\gamma$ (68.3% DS CL)	$17.0^{+12.0\ +1.5\ +6.0}_{-12.0\ -1.2\ -6.0} = 17.0^{+13.7}_{-13.3}$	18.8 ± 0.3
$e\,W\gamma$ (68.3% SS CL)	< 24.5	
$e\,W\gamma$ (90.0% SS CL)	< 35.9	
$e\,W\gamma$ (95.0% SS CL)	< 41.5	
μ $W\gamma$ (68.3% DS CL)	$19.4^{+16.8\ +2.2\ +6.2}_{-16.9\ -1.2\ -6.3} = 19.4^{+19.1}_{-18.0}$	19.2 ± 0.4
$\mu\,W\gamma$ (68.3% SS CL)	< 30.4	
$\mu\,W\gamma$ (90.0% SS CL)	< 46.4	
$\mu\,W\gamma$ (95.0% SS CL)	< 54.3	
e $Z\gamma$ (68.3% DS CL)	$6.8^{+5.7\ +0.6\ +0.5}_{-5.7\ -0.5\ -0.6} = 6.8^{+5.9}_{-5.8}$	4.6 ± 0.1
$e\,Z\gamma$ (68.3% SS CL)	< 10.4	
$e\,Z\gamma$ (90.0% SS CL)	< 15.4	
$e\,Z\gamma$ (95.0% SS CL)	< 18.2	
μ $Z\gamma$ (68.3% DS CL)	$13.6^{+10.1\ +1.6\ +0.3}_{-10.1\ -0.6\ -0.3} = 13.6^{+11.2}_{-10.1}$	4.7 ± 0.1
$\mu\,Z\gamma$ (68.3% SS CL)	< 20.4	
$\mu\,Z\gamma$ (90.0% SS CL)	< 29.5	
$\mu\,Z\gamma$ (95.0% SS CL)	< 34.7	

Table 12: Combined $e+\mu$ $\sigma * BR(W+\gamma)$ and $\sigma * BR(Z+\gamma)$ Results

Channel	$\sigma \cdot B_{expt}$ (pb)	$\sigma \cdot B^{SM}_{pred}$ (pb)
$e+\mu$ $W\gamma$ (68.3% DS CL)	$17.9^{+9.8\ +1.8\ +4.5}_{-9.8\ -1.1\ -4.5} = 17.9^{+11.3}_{-10.7}$	19.0 ± 0.3
$e+\mu\,W\gamma$ (68.3% SS CL)	< 23.5	
$e+\mu\,W\gamma$ (90.0% SS CL)	< 32.9	
$e+\mu\,W\gamma$ (95.0% SS CL)	< 37.4	
$e+\mu$ $Z\gamma$ (68.3% DS CL)	$9.2^{+5.2\ +0.9\ +0.4}_{-5.2\ -0.5\ -0.4} = 9.2^{+5.6}_{-5.2}$	4.7 ± 0.1
$e+\mu\,Z\gamma$ (68.3% SS CL)	< 11.8	
$e+\mu\,Z\gamma$ (90.0% SS CL)	< 16.6	
$e+\mu\,Z\gamma$ (95.0% SS CL)	< 19.1	

Table 13a: Summary of Diboson P_T Systematic Uncertainties

Channel	$\Delta\sigma_{MC}$ (pb)	$\Delta\sigma_{Expt}$ (pb)	$\Delta\sigma_{MC-Expt}$ (pb)
$e\ W\gamma$	$^{+2.2}_{-0.5}$	$^{+1.1}_{-0.7}$	$^{+1.2}_{-0.2}$
$\mu\ W\gamma$	$^{+1.8}_{-0.6}$	$^{+1.4}_{-0.3}$	$^{+0.4}_{-0.4}$
$e+\mu\ W\gamma$	$^{+1.8}_{-0.6}$	$^{+1.2}_{-0.6}$	$^{+1.7}_{-0.1}$
$e\ Z\gamma$	$^{+0.05}_{-0.08}$	$^{+0.26}_{-0.07}$	$^{+0.21}_{-0.05}$
$\mu\ Z\gamma$	$^{+0.11}_{-0.05}$	$^{+0.05}_{-0.05}$	$^{+0.14}_{-0.05}$
$e+\mu\ Z\gamma$	$^{+0.11}_{-0.05}$	$^{+0.21}_{-0.07}$	$^{+0.08}_{-0.10}$

Table 13b: Summary of Diboson Q^2 Systematic Uncertainties

Channel	$\Delta\sigma_{MC}$ (pb)	$\Delta\sigma_{Expt}$ (pb)	$\Delta\sigma_{MC-Expt}$ (pb)
$e\ W\gamma$	$^{+1.1}_{-0.3}$	$^{+0.8}_{-0.3}$	$^{+0.7}_{-0.4}$
$\mu\ W\gamma$	$^{+0.9}_{-0.3}$	$^{+0.5}_{-0.4}$	$^{+1.3}_{-0.8}$
$e+\mu\ W\gamma$	$^{+0.9}_{-0.3}$	$^{+0.7}_{-0.1}$	$^{+0.8}_{-1.0}$
$e\ Z\gamma$	$^{+0.1}_{-0.1}$	$^{+0.1}_{-0.1}$	$^{+0.1}_{-0.2}$
$\mu\ Z\gamma$	$^{+0.1}_{-0.2}$	$^{+0.2}_{-0.5}$	$^{+0.4}_{-0.1}$
$e+\mu\ Z\gamma$	$^{+0.1}_{-0.2}$	$^{+0.1}_{-0.2}$	$^{+0.1}_{-0.2}$

Table 13c: Summary of Diboson SF Systematic Uncertainties

Channel	$\Delta\sigma_{MC}$ (pb)	$\Delta\sigma_{Expt}$ (pb)	$\Delta\sigma_{MC-Expt}$ (pb)
$e\ W\gamma$	$^{+3.3}_{-1.0}$	$^{+0.7}_{-0.6}$	$^{+2.6}_{-0.3}$
$\mu\ W\gamma$	$^{+2.6}_{-0.6}$	$^{+1.6}_{-0.6}$	$^{+2.1}_{-1.0}$
$e+\mu\ W\gamma$	$^{+2.6}_{-0.6}$	$^{+1.0}_{-0.6}$	$^{+2.0}_{-0.6}$
$e\ Z\gamma$	$^{+0.5}_{-0.2}$	$^{+0.2}_{-0.7}$	$^{+0.7}_{-0.3}$
$\mu\ Z\gamma$	$^{+0.7}_{-0.1}$	$^{+0.6}_{-0.1}$	$^{+0.5}_{-0.5}$
$e+\mu\ Z\gamma$	$^{+0.7}_{-0.1}$	$^{+0.4}_{-0.1}$	$^{+0.5}_{-0.2}$

Table 13d: Summary of $P_T \oplus Q^2 \oplus SF$ Systematic Uncertainties

Channel	$\Delta\sigma_{MC}$ (pb)	$\Delta\sigma_{Expt}$ (pb)	$\Delta\sigma_{MC-Expt}$ (pb)
$e\ W\gamma$	$^{+4.1}_{-1.2}$	$^{+1.5}_{-1.0}$	$^{+2.9}_{-0.5}$
$\mu\ W\gamma$	$^{+3.3}_{-0.9}$	$^{+2.2}_{-0.8}$	$^{+2.5}_{-1.3}$
$e+\mu\ W\gamma$	$^{+3.3}_{-0.9}$	$^{+1.7}_{-0.9}$	$^{+2.3}_{-1.3}$
$e\ Z\gamma$	$^{+0.5}_{-0.2}$	$^{+0.3}_{-0.7}$	$^{+0.7}_{-0.4}$
$\mu\ Z\gamma$	$^{+0.7}_{-0.2}$	$^{+0.6}_{-0.5}$	$^{+0.7}_{-0.4}$
$e+\mu\ Z\gamma$	$^{+0.7}_{-0.2}$	$^{+0.5}_{-0.2}$	$^{+0.5}_{-0.3}$

Table 14: Combined $e + \mu$ Cross Section Ratios

Cross Section Ratio	$\mathcal{R}_{expt}$	$\mathcal{R}_{SM}$
$\mathcal{R}(W\gamma/W)_e$	$0.8^{+0.6}_{-0.6}\%$	
$\mathcal{R}(W\gamma/W)_\mu$	$0.9^{+0.8}_{-0.8}\%$	$0.92 \pm 0.02\%$
$\mathcal{R}(W\gamma/W)_{e+\mu}$	$0.8^{+0.5}_{-0.5}\%$	
$\mathcal{R}(Z\gamma/Z)_e$	$3.3^{+2.8}_{-2.7}\%$	
$\mathcal{R}(Z\gamma/Z)_\mu$	$6.0^{+4.7}_{-4.5}\%$	$2.42 \pm 0.04\%$
$\mathcal{R}(Z\gamma/Z)_{e+\mu}$	$4.3^{+2.5}_{-2.4}\%$	
$\mathcal{R}(W\gamma/Z\gamma)_e$	$2.5^{+2.7}_{-2.5}$	
$\mathcal{R}(W\gamma/Z\gamma)_\mu$	$1.4^{+2.1}_{-1.4}$	4.00 ± 0.07
$\mathcal{R}(W\gamma/Z\gamma)_{e+\mu}$	$1.9^{+2.0}_{-1.4}$	
$\mathcal{R}(W/Z)_e$	$10.2^{+0.9}_{-0.9}$	
$\mathcal{R}(W/Z)_\mu$	$9.8^{+1.2}_{-1.2}$	10.69 ± 0.22
$\mathcal{R}(W/Z)_{e+\mu}$	$10.0^{+0.7}_{-0.7}$	

Table 15a: Electron $W\gamma$ $\Delta\kappa$ – λ Limits

Parameter	CL Range	Electron Limits
$\Delta\kappa$	68.3% DS CL	$0.0^{+5.0}_{-4.5}(stat) \pm 0.7(syst) = 0.0^{+5.7}_{-5.2}(stat+syst)$
	68.3% SS CL	$-3.5 < \Delta\kappa < +4.0$
$(\lambda = 0)$	90.0% SS CL	$-6.3 < \Delta\kappa < +6.7$
	95.0% SS CL	$-7.3 < \Delta\kappa < +7.7$
λ	68.3% DS CL	$0.0^{+2.2}_{-2.2}(stat) \pm 0.3(syst) = 0.0^{+2.5}_{-2.5}(stat+syst)$
	68.3% SS CL	$-1.7 < \lambda < +1.7$
$(\Delta\kappa = 0)$	90.0% SS CL	$-3.0 < \lambda < +3.0$
	95.0% SS CL	$-3.5 < \lambda < +3.4$

Table 15b: Muon $W\gamma$ $\Delta\kappa$ – λ Limits

Parameter	CL Range	Muon Limits
$\Delta\kappa$	68.3% DS CL	$0.0^{+6.6}_{-6.1}(stat) \pm 0.7(syst) = 0.0^{+7.2}_{-6.8}(stat+syst)$
	68.3% SS CL	$-5.1 < \Delta\kappa < +5.6$
$(\lambda = 0)$	90.0% SS CL	$-8.0 < \Delta\kappa < +8.5$
	95.0% SS CL	$-9.1 < \Delta\kappa < +9.6$
λ	68.3% DS CL	$0.0^{+2.9}_{-2.9}(stat) \pm 0.3(syst) = 0.0^{+3.2}_{-3.2}(stat+syst)$
	68.3% SS CL	$-2.5 < \lambda < +2.5$
$(\Delta\kappa = 0)$	90.0% SS CL	$-3.8 < \lambda < +3.8$
	95.0% SS CL	$-4.3 < \lambda < +4.3$

Table 15c: $e+\mu$ Combined $W\gamma$ $\Delta\kappa$ – λ Limits

Parameter	CL Range	$e+\mu$ Limits
$\Delta\kappa$	68.3% DS CL	$0.0^{+4.6}_{-4.2}(stat) \pm 0.7(syst) = 0.0^{+5.4}_{-4.9}(stat+syst)$
	68.3% SS CL	$-3.3 < \Delta\kappa < +3.7$
$(\lambda = 0)$	90.0% SS CL	$-5.7 < \Delta\kappa < +6.2$
	95.0% SS CL	$-6.6 < \Delta\kappa < +7.1$
λ	68.3% DS CL	$0.0^{+2.0}_{-2.0}(stat) \pm 0.3(syst) = 0.0^{+2.3}_{-2.4}(stat+syst)$
	68.3% SS CL	$-1.6 < \lambda < +1.6$
$(\Delta\kappa = 0)$	90.0% SS CL	$-2.7 < \lambda < +2.7$
	95.0% SS CL	$-3.2 < \lambda < +3.1$

Table 16a: CDF *vs* UA2 Comparison of $\Delta\kappa$ – λ Limits ($\sigma * B$ Method)

Parameter	CL Range	CDF $e+\mu$ Limits	UA2 Limits
$\Delta\kappa$	68.3% $DS\ CL$	$0.0^{+4.6}_{-4.2}(stat) \pm 0.7(syst)$	$0.0^{+4.6}_{-4.2}(stat) \pm 1.0(syst)$
	68.3% $SS\ CL$	$-3.3 < \Delta\kappa < +3.7$	–
$(\lambda = 0)$	90.0% $SS\ CL$	$-5.7 < \Delta\kappa < +6.2$	–
	95.0% $SS\ CL$	$-6.6 < \Delta\kappa < +7.1$	$-6.3 < \Delta\kappa < +6.9$
λ	68.3% $DS\ CL$	$0.0^{+2.0}_{-2.0}(stat) \pm 0.3(syst)$	$0.0^{+2.9}_{-2.9}(stat) \pm 0.7(syst)$
	68.3% $SS\ CL$	$-1.6 < \lambda < +1.6$	–
$(\Delta\kappa = 0)$	90.0% $SS\ CL$	$-2.7 < \lambda < +2.7$	–
	95.0% $SS\ CL$	$-3.2 < \lambda < +3.1$	$-4.4 < \lambda < +4.4$

Table 16b: UA2 $\Delta\kappa$ – λ Limits (P_T^γ Method)

Parameter	CL Range	UA2 Limits
$\Delta\kappa$	68.3% $DS\ CL$	$0.0^{+2.6}_{-2.2}\ (stat)$
$(\lambda = 0)$	95.0% $SS\ CL$	$-4.5 < \Delta\kappa < +4.9$
λ	68.3% $DS\ CL$	$0.0^{+1.7}_{-1.8}\ (stat)$
$(\Delta\kappa = 0)$	95.0% $SS\ CL$	$-3.6 < \lambda < +3.5$

Table 17: CDF Limits on W Boson EM Moments

$$\begin{aligned}
\mu_W &= \tfrac{e}{2M_W}(2+\Delta\kappa+\lambda) && \text{Magnetic Dipole Moment}\\
Q_W &= -\tfrac{e}{M_W^2}(1+\Delta\kappa-\lambda) && \text{Electric Quadrupole Moment}\\
< R_W >^2 &= \tfrac{1}{M_W^2}(1+\Delta\kappa+\lambda) && \text{Mean-Squared Charge Radius}
\end{aligned}$$

In the SM (tree level): $\Delta\kappa = 1-\kappa = 0, \quad \lambda = 0$

$$\begin{aligned}
\mu_W^\circ &= \tfrac{e\hbar c}{2M_W c^2} && = 3.691 \pm 0.012 \times 10^{-16}\ MeV/T\\
(\mu_e^\circ &= \tfrac{e\hbar c}{2M_e c^2} && = 5.788 \pm 0.000 \times 10^{-11}\ MeV/T)\\
Q_W^\circ &= -e\left(\tfrac{\hbar c}{M_W c^2}\right)^2 = -e\lambda_W^2 && = 6.063 \pm 0.041 \times 10^{-6}\ e-fm^2\\
\lambda_W &= \tfrac{\hbar c}{M_W c^2} && = 2.462 \pm 0.008 \times 10^{-3}\ fm = 2.462 \pm 0.008 \times 10^{-16}\ cm
\end{aligned}$$

Parameter	CL Range	CDF $e+\mu$ Limits
μ_W/μ_W°	68.3% $DS\ CL$	$2.0\ ^{+3.2}_{-3.1}\ (stat) \pm 0.5\ (syst) = 2.0\ ^{+3.7}_{-3.6}\ (stat+syst)$
	68.3% $SS\ CL$	$-2.5 < \mu_W/\mu_W^\circ - 2 \equiv g_W - 2 < +2.5$
$(Q_W/Q_W^\circ = 1)$	90.0% $SS\ CL$	$-4.2 < \mu_W/\mu_W^\circ - 2 \equiv g_W - 2 < +4.3$
	95.0% $SS\ CL$	$-4.8 < \mu_W/\mu_W^\circ - 2 \equiv g_W - 2 < +4.9$
Q_W/Q_W°	68.3% $DS\ CL$	$1.0\ ^{+4.9}_{-4.5}\ (stat) \pm 0.7\ (syst) = 1.0\ ^{+5.6}_{-5.3}\ (stat+syst)$
	68.3% $SS\ CL$	$-3.6 < Q_W/Q_W^\circ - 1 \equiv q_W - 1 < +3.9$
$(\mu_W/\mu_W^\circ = 2)$	90.0% $SS\ CL$	$-6.2 < Q_W/Q_W^\circ - 1 \equiv q_W - 1 < +6.5$
	95.0% $SS\ CL$	$-7.1 < Q_W/Q_W^\circ - 1 \equiv q_W - 1 < +7.4$
$< R_W >^2 /\lambda_W^2$	68.3% $DS\ CL$	$1.0\ ^{+3.2}_{-3.1}\ (stat) \pm 0.5\ (syst) = 1.0\ ^{+3.7}_{-3.6}\ (stat+syst)$
	68.3% $SS\ CL$	$-2.5 < < R_W >^2 /\lambda_W^2 - 1 \equiv r_W^2 - 1 < +2.5$
$(Q_W/Q_W^\circ = 1)$	90.0% $SS\ CL$	$-4.2 < < R_W >^2 /\lambda_W^2 - 1 \equiv r_W^2 - 1 < +4.3$
	95.0% $SS\ CL$	$-4.8 < < R_W >^2 /\lambda_W^2 - 1 \equiv r_W^2 - 1 < +4.9$

Table 18a: $Z\gamma\, h_{30}^Z\ -\ h_{40}^Z$ **Limits** ($\Lambda = 250\ GeV$)

Parameter	CL Range	Electron Limits ($\Lambda = 250\ GeV$)
h_{30}^Z	68.3% $DS\ CL$	$0.0^{+22.0}_{-22.3}(stat) \pm 2.4(syst) = 0.0^{+24.4}_{-24.7}(stat+syst)$
	68.3% $SS\ CL$	$-21.2 < h_{30}^Z < +20.9$
$(h_{40}^Z = 0)$	90.0% $SS\ CL$	$-28.8 < h_{30}^Z < +28.5$
	95.0% $SS\ CL$	$-32.3 < h_{30}^Z < +32.0$
h_{40}^Z	68.3% $DS\ CL$	$0.0^{+19.2}_{-19.3}(stat) \pm 2.0(syst) = 0.0^{+21.3}_{-21.3}(stat+syst)$
	68.3% $SS\ CL$	$-18.3 < h_{40}^Z < +18.3$
$(h_{30}^Z = 0)$	90.0% $SS\ CL$	$-24.9 < h_{40}^Z < +24.9$
	95.0% $SS\ CL$	$-28.0 < h_{40}^Z < +27.9$
Parameter	CL Range	Muon Limits ($\Lambda = 250\ GeV$)
h_{30}^Z	68.3% $DS\ CL$	$0.0^{+34.8}_{-35.1}(stat) \pm 3.5(syst) = 0.0^{+38.3}_{-38.6}(stat+syst)$
	68.3% $SS\ CL$	$-34.8 < h_{30}^Z < +34.5$
$(h_{40}^Z = 0)$	90.0% $SS\ CL$	$-43.6 < h_{30}^Z < +43.3$
	95.0% $SS\ CL$	$-48.0 < h_{30}^Z < +47.7$
h_{40}^Z	68.3% $DS\ CL$	$0.0^{+30.4}_{-30.5}(stat) \pm 3.0(syst) = 0.0^{+33.4}_{-33.4}(stat+syst)$
	68.3% $SS\ CL$	$-30.1 < h_{40}^Z < +30.1$
$(h_{30}^Z = 0)$	90.0% $SS\ CL$	$-37.8 < h_{40}^Z < +37.8^{\dagger}$
	95.0% $SS\ CL$	$-41.6 < h_{40}^Z < +41.5^{\dagger}$
Parameter	CL Range	$e+\mu$ Limits ($\Lambda = 250\ GeV$)
h_{30}^Z	68.3% $DS\ CL$	$0.0^{+26.9}_{-27.2}(stat) \pm 0.9(syst) = 0.0^{+27.8}_{-28.1}(stat+syst)$
	68.3% $SS\ CL$	$-23.7 < h_{30}^Z < +23.4$
$(h_{40}^Z = 0)$	90.0% $SS\ CL$	$-30.5 < h_{30}^Z < +30.2$
	95.0% $SS\ CL$	$-33.4 < h_{30}^Z < +33.1$
h_{40}^Z	68.3% $DS\ CL$	$0.0^{+23.5}_{-23.6}(stat) \pm 0.8(syst) = 0.0^{+24.3}_{-24.3}(stat+syst)$
	68.3% $SS\ CL$	$-20.5 < h_{40}^Z < +20.4$
$(h_{30}^Z = 0)$	90.0% $SS\ CL$	$-26.4 < h_{40}^Z < +26.3$
	95.0% $SS\ CL$	$-28.9 < h_{40}^Z < +28.9$

† Exceeds unitarity limit

Table 18b: $Z\gamma\ h_{30}^Z\ -\ h_{40}^Z$ **Limits** ($\Lambda = 500\ GeV$)

Parameter	CL Range	Electron Limits ($\Lambda = 500\ GeV$)
h_{30}^Z	68.3% *DS CL*	$0.0^{+6.3}_{-6.2}(stat) \pm 0.7(syst) = 0.0^{+7.0}_{-6.8}(stat+syst)$
	68.3% *SS CL*	$-5.8 < h_{30}^Z < +6.0$
$(h_{40}^Z = 0)$	90.0% *SS CL*	$-8.0 < h_{30}^Z < +8.1$
	95.0% *SS CL*	$-9.0 < h_{30}^Z < +9.1^\dagger$
h_{40}^Z	68.3% *DS CL*	$0.0^{+1.7}_{-1.7}(stat) \pm 0.2(syst) = 0.0^{+1.9}_{-1.8}(stat+syst)$
	68.3% *SS CL*	$-1.6 < h_{40}^Z < +1.6^\dagger$
$(h_{30}^Z = 0)$	90.0% *SS CL*	$-2.2 < h_{40}^Z < +2.2^\dagger$
	95.0% *SS CL*	$-2.4 < h_{40}^Z < +2.4^\dagger$
Parameter	CL Range	Muon Limits ($\Lambda = 500\ GeV$)
h_{30}^Z	68.3% *DS CL*	$0.0^{+9.9}_{-9.8}(stat) \pm 1.0(syst) = 0.0^{+10.9}_{-10.8}(stat+syst)$
	68.3% *SS CL*	$-9.7 < h_{30}^Z < +9.8^\dagger$
$(h_{40}^Z = 0)$	90.0% *SS CL*	$-12.2 < h_{30}^Z < +12.4^\dagger$
	95.0% *SS CL*	$-13.5 < h_{30}^Z < +13.6^\dagger$
h_{40}^Z	68.3% *DS CL*	$0.0^{+2.7}_{-2.6}(stat) \pm 0.3(syst) = 0.0^{+2.9}_{-2.9}(stat+syst)$
	68.3% *SS CL*	$-2.6 < h_{40}^Z < +2.6^\dagger$
$(h_{30}^Z = 0)$	90.0% *SS CL*	$-3.3 < h_{40}^Z < +3.3^\dagger$
	95.0% *SS CL*	$-3.6 < h_{40}^Z < +3.6^\dagger$
Parameter	CL Range	$e+\mu$ Limits ($\Lambda = 500\ GeV$)
h_{30}^Z	68.3% *DS CL*	$0.0^{+7.7}_{-7.7}(stat) \pm 0.2(syst) = 0.0^{+7.9}_{-7.8}(stat+syst)$
	68.3% *SS CL*	$-6.6 < h_{30}^Z < +6.7$
$(h_{40}^Z = 0)$	90.0% *SS CL*	$-8.5 < h_{30}^Z < +8.6^\dagger$
	95.0% *SS CL*	$-9.3 < h_{30}^Z < +9.4^\dagger$
h_{40}^Z	68.3% *DS CL*	$0.0^{+2.0}_{-2.0}(stat) \pm 0.1(syst) = 0.0^{+2.1}_{-2.1}(stat+syst)$
	68.3% *SS CL*	$-1.8 < h_{40}^Z < +1.8^\dagger$
$(h_{30}^Z = 0)$	90.0% *SS CL*	$-2.3 < h_{40}^Z < +2.3^\dagger$
	95.0% *SS CL*	$-2.5 < h_{40}^Z < +2.5^\dagger$

† Exceeds unitarity limit

Table 18c: $Z\gamma\, h_{30}^Z\ -\ h_{40}^Z$ **Limits** ($\Lambda = 750\ GeV$)

Parameter	CL Range	Electron Limits ($\Lambda = 750\ GeV$)
h_{30}^Z	68.3% $DS\ CL$	$0.0^{+3.5}_{-3.5}(stat) \pm 0.4(syst) = 0.0^{+3.9}_{-3.8}(stat+syst)$
	68.3% $SS\ CL$	$-3.3 < h_{30}^Z < +3.3^{\dagger}$
$(h_{40}^Z = 0)$	90.0% $SS\ CL$	$-4.5 < h_{30}^Z < +4.5^{\dagger}$
	95.0% $SS\ CL$	$-5.0 < h_{30}^Z < +5.0^{\dagger}$
h_{40}^Z	68.3% $DS\ CL$	$0.0^{+0.6}_{-0.6}(stat) \pm 0.1(syst) = 0.0^{+0.7}_{-0.7}(stat+syst)$
	68.3% $SS\ CL$	$-0.6 < h_{40}^Z < +0.6^{\dagger}$
$(h_{30}^Z = 0)$	90.0% $SS\ CL$	$-0.8 < h_{40}^Z < +0.8^{\dagger}$
	95.0% $SS\ CL$	$-0.9 < h_{40}^Z < +0.9^{\dagger}$
Parameter	CL Range	Muon Limits ($\Lambda = 750\ GeV$)
h_{30}^Z	68.3% $DS\ CL$	$0.0^{+5.5}_{-5.5}(stat) \pm 0.5(syst) = 0.0^{+6.0}_{-6.0}(stat+syst)$
	68.3% $SS\ CL$	$-5.4 < h_{30}^Z < +5.4^{\dagger}$
$(h_{40}^Z = 0)$	90.0% $SS\ CL$	$-6.8 < h_{30}^Z < +6.8^{\dagger}$
	95.0% $SS\ CL$	$-7.5 < h_{30}^Z < +7.5^{\dagger}$
h_{40}^Z	68.3% $DS\ CL$	$0.0^{+0.9}_{-0.9}(stat) \pm 0.1(syst) = 0.0^{+1.0}_{-1.0}(stat+syst)$
	68.3% $SS\ CL$	$-0.9 < h_{40}^Z < +0.9^{\dagger}$
$(h_{30}^Z = 0)$	90.0% $SS\ CL$	$-1.2 < h_{40}^Z < +1.2^{\dagger}$
	95.0% $SS\ CL$	$-1.3 < h_{40}^Z < +1.3^{\dagger}$
Parameter	CL Range	$e+\mu$ Limits ($\Lambda = 750\ GeV$)
h_{30}^Z	68.3% $DS\ CL$	$0.0^{+4.3}_{-4.3}(stat) \pm 0.1(syst) = 0.0^{+4.4}_{-4.4}(stat+syst)$
	68.3% $SS\ CL$	$-3.7 < h_{30}^Z < +3.7^{\dagger}$
$(h_{40}^Z = 0)$	90.0% $SS\ CL$	$-4.7 < h_{30}^Z < +4.7^{\dagger}$
	95.0% $SS\ CL$	$-5.2 < h_{30}^Z < +5.2^{\dagger}$
h_{40}^Z	68.3% $DS\ CL$	$0.0^{+0.7}_{-0.7}(stat) \pm 0.1(syst) = 0.0^{+0.7}_{-0.7}(stat+syst)$
	68.3% $SS\ CL$	$-0.6 < h_{40}^Z < +0.6^{\dagger}$
$(h_{30}^Z = 0)$	90.0% $SS\ CL$	$-0.8 < h_{40}^Z < +0.8^{\dagger}$
	95.0% $SS\ CL$	$-0.9 < h_{40}^Z < +0.9^{\dagger}$

† Exceeds unitarity limit

18 List of Figures

Figure 1: Tree-Level $(W \to \ell\nu_\ell) + \gamma$ Feynman diagrams

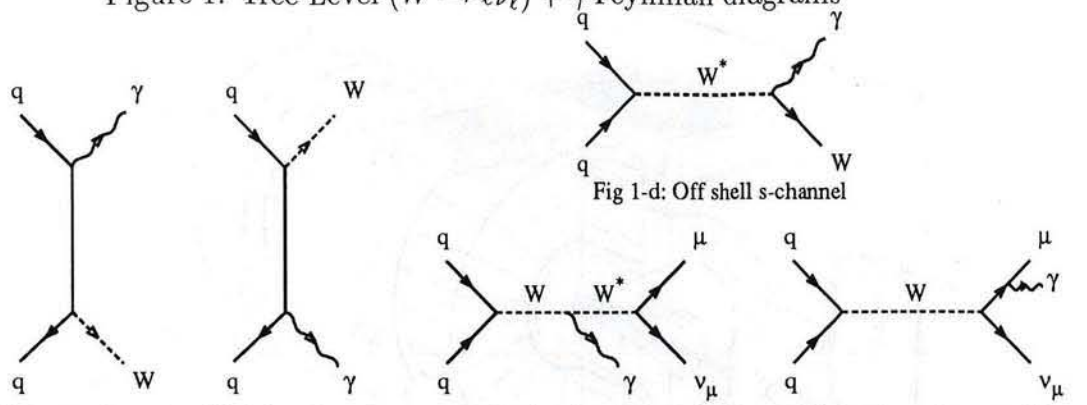

Figure 2: Tree-Level $(Z \to \ell^+\ell^-) + \gamma$ Feynman diagrams

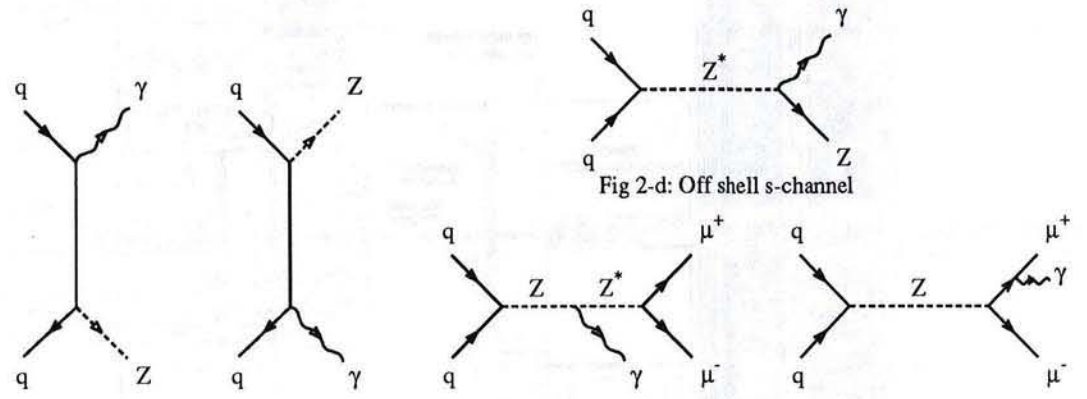

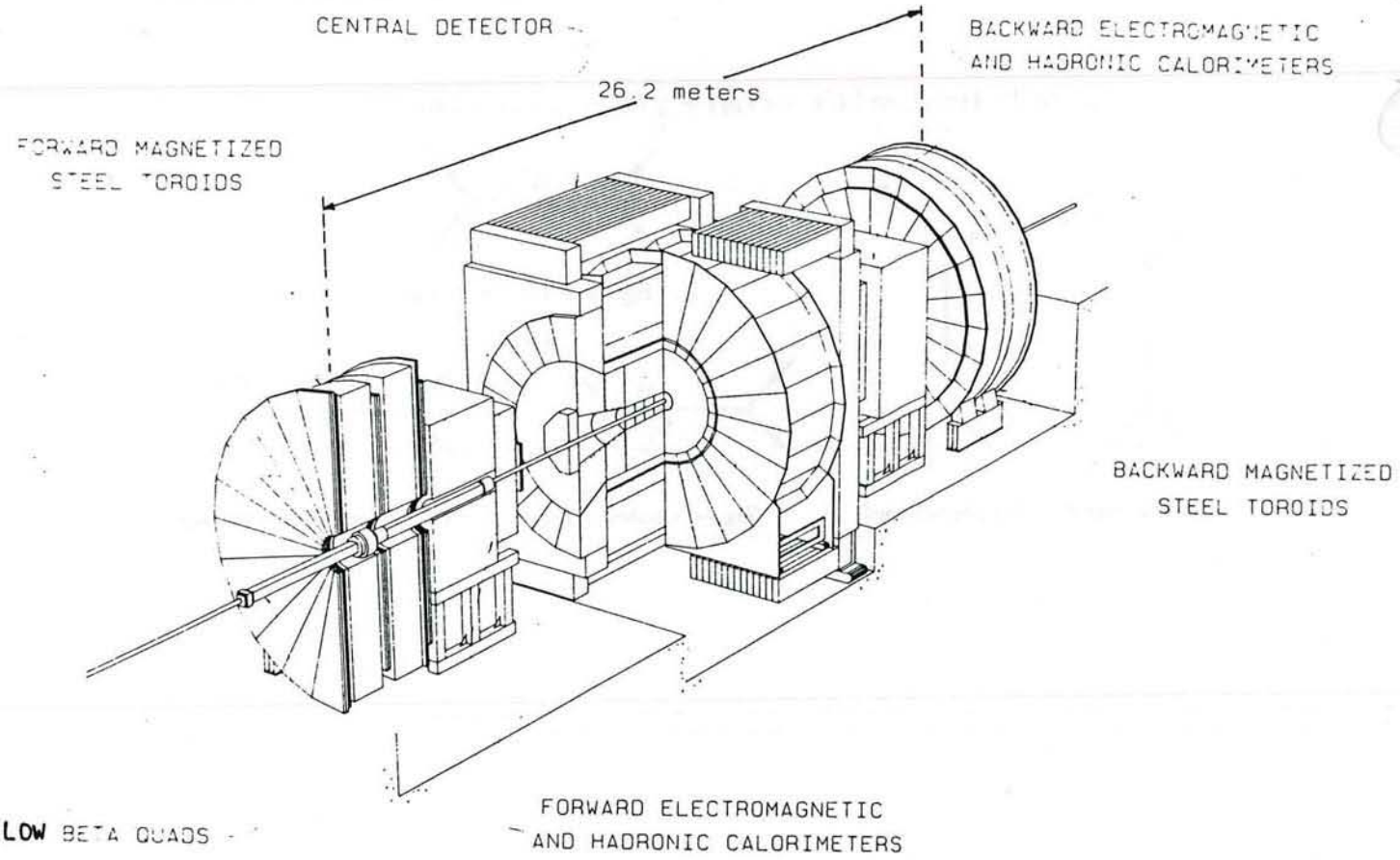

. A perspective view of the CDF detector showing the central detector and the forward and backward detectors.

Fig 3

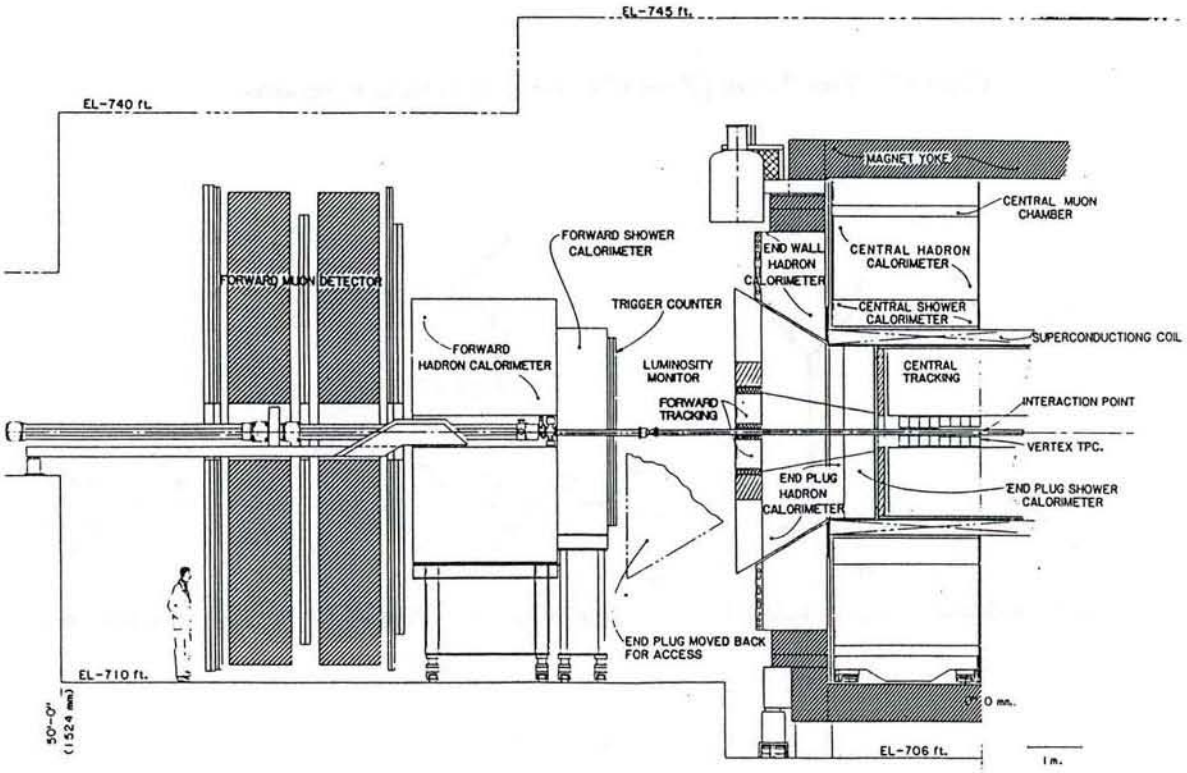

Cross section through a vertical plane of one half the CDF detector. The detector is symmetric about the midplane and roughly symmetric around the beam axis.

Fig 4

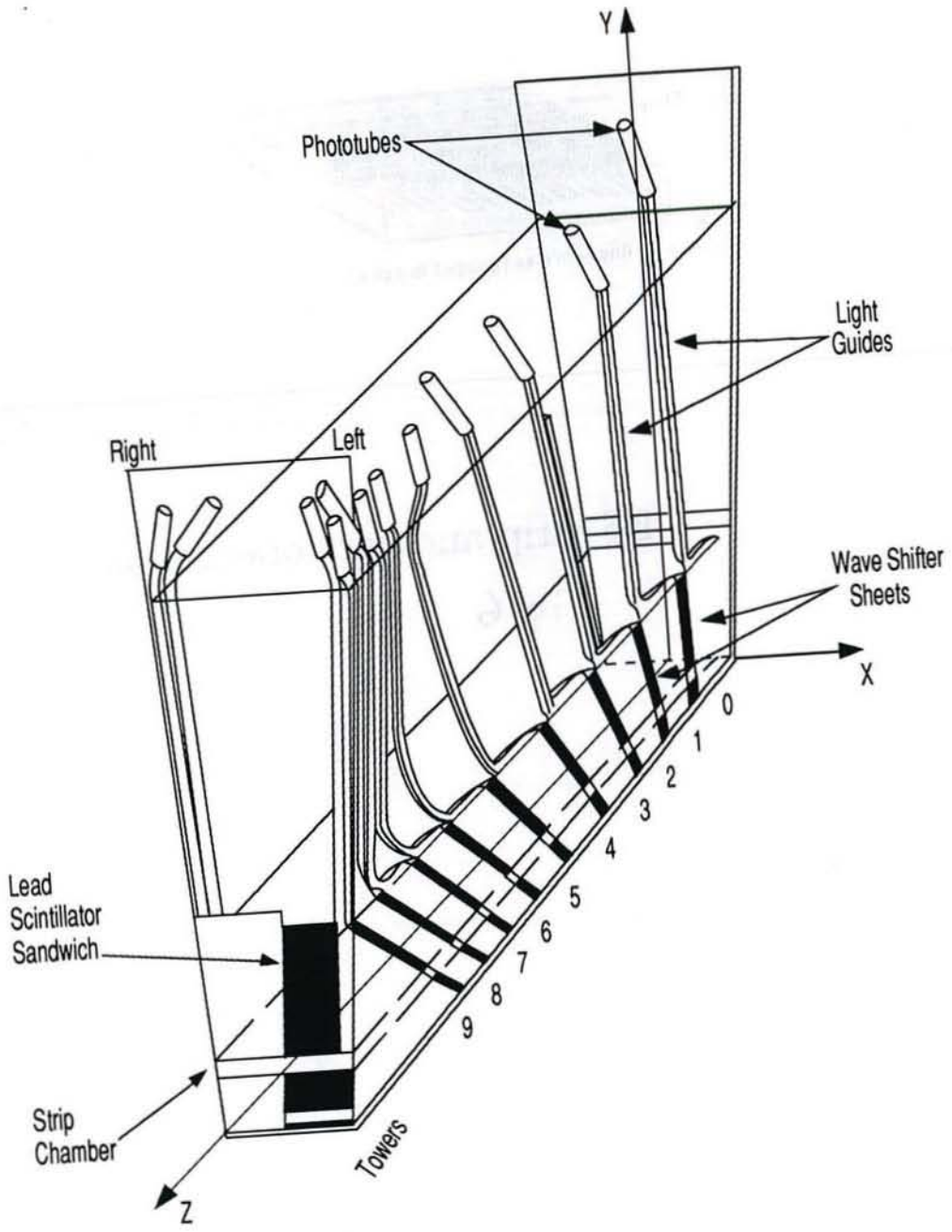
Y
Phototubes
Light
Guides
Right
Left
Wave Shifter
Sheets
X
0
1
2
3
4
5
6
7
8
9
Towers
Lead
Scintillator
Sandwich
Strip
Chamber
Z

FIG 5

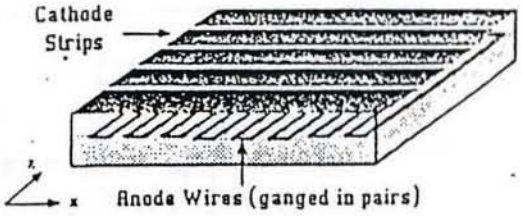

CES strip and wire orientation.

Fig 6

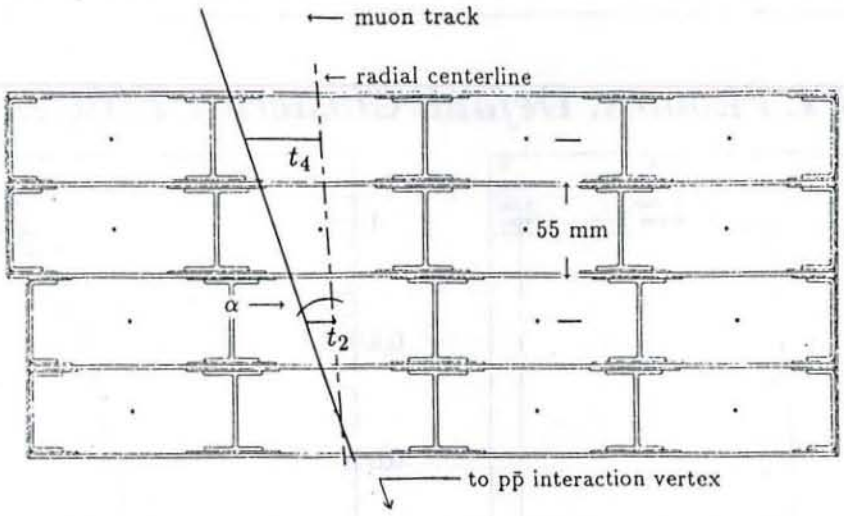

Cross section of a single muon chamber, showing drift times t_i and the track angle α.

Fig 7

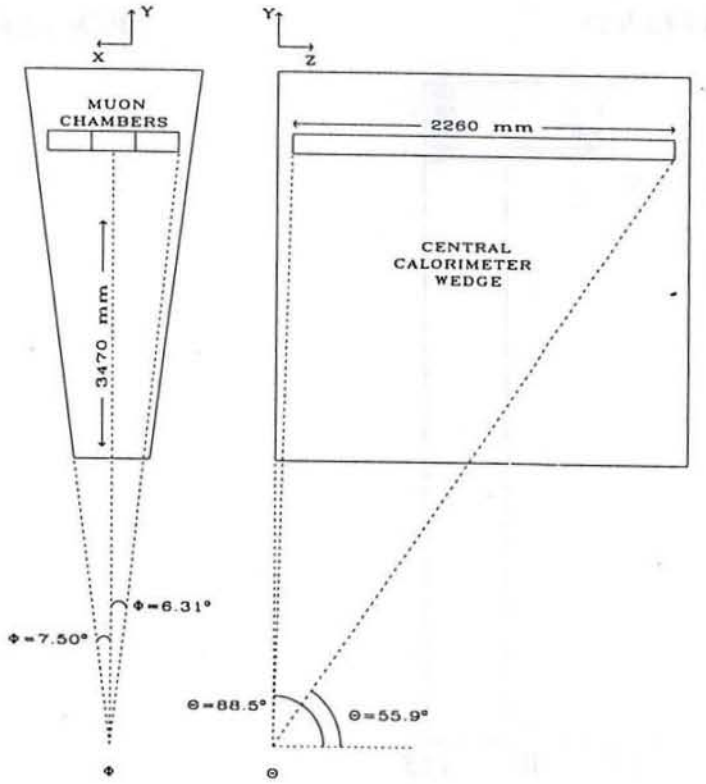

Location of the central muon chambers within the central calorimeter.

Fig 8

09/01/93 22.10

QFL Photons: Default Clustering Efficiency

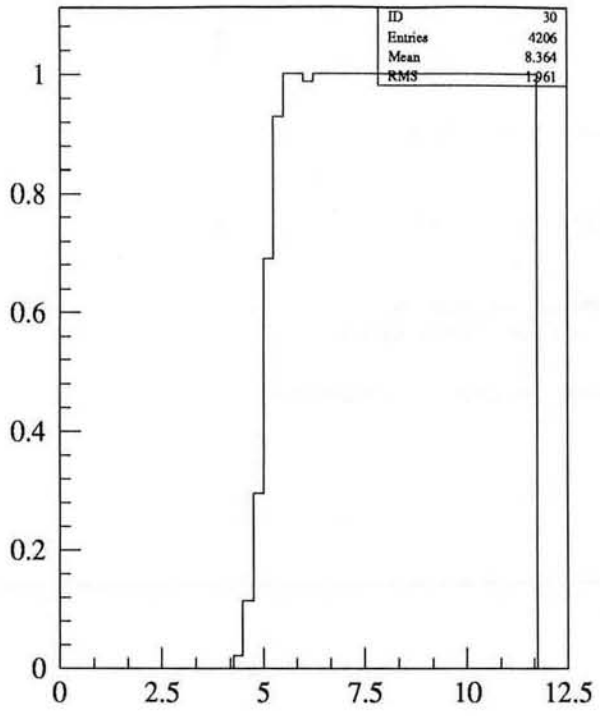

CEM ELES Et

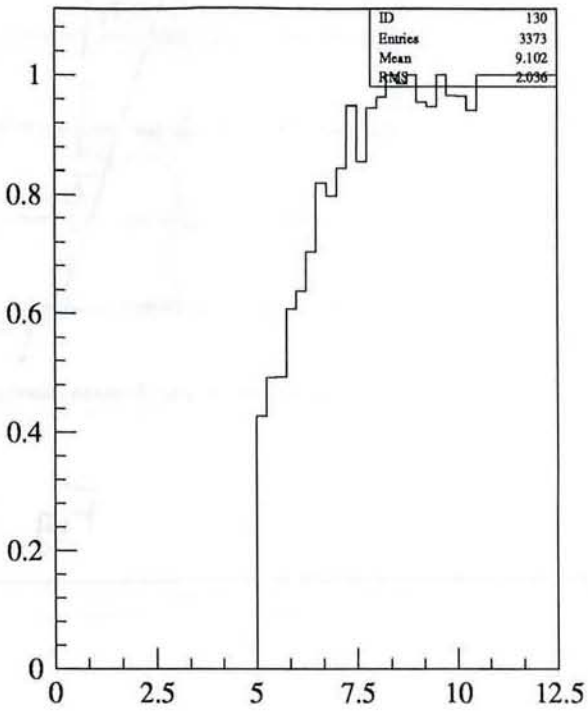

PEM ELES Et

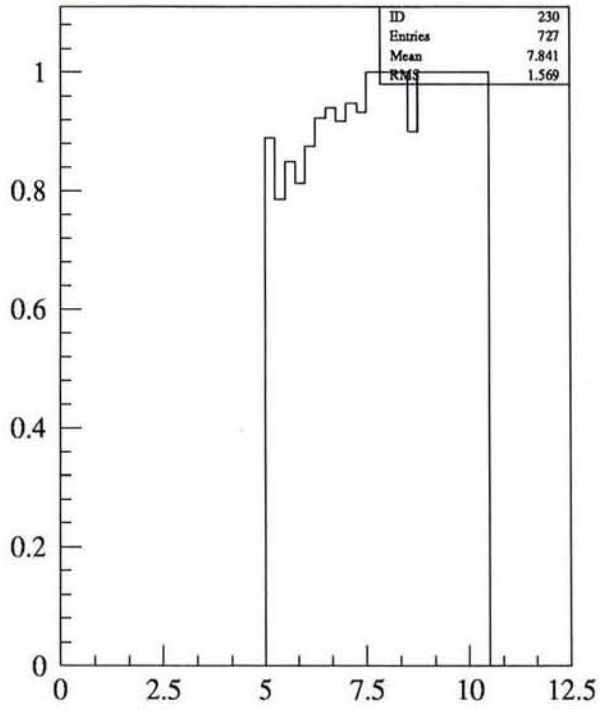

FEM ELES Et

Fig 9a

QFL Photons - Solid: Default, Dashed:Seed=1.0 Sum=1.5

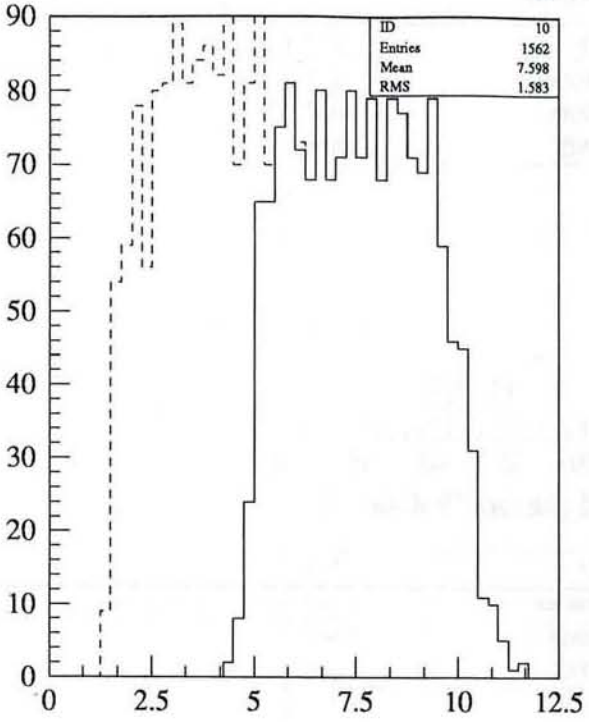

CEM ELES Et Default Clustering

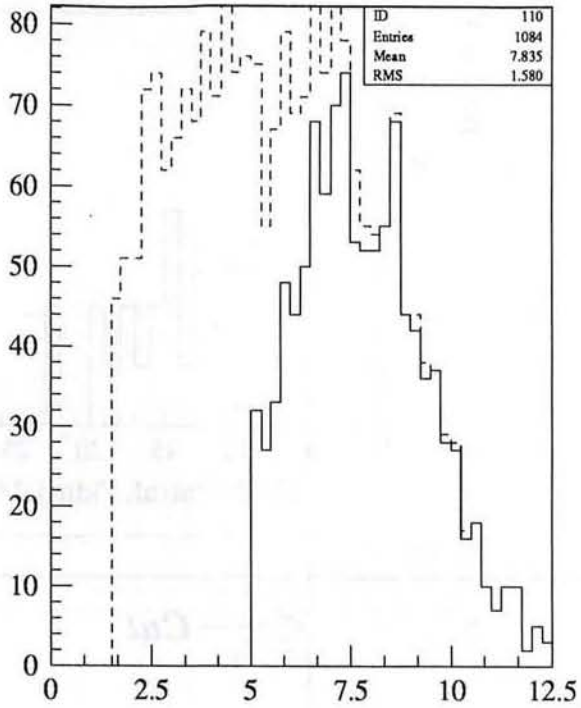

PEM ELES Et Default Clustering

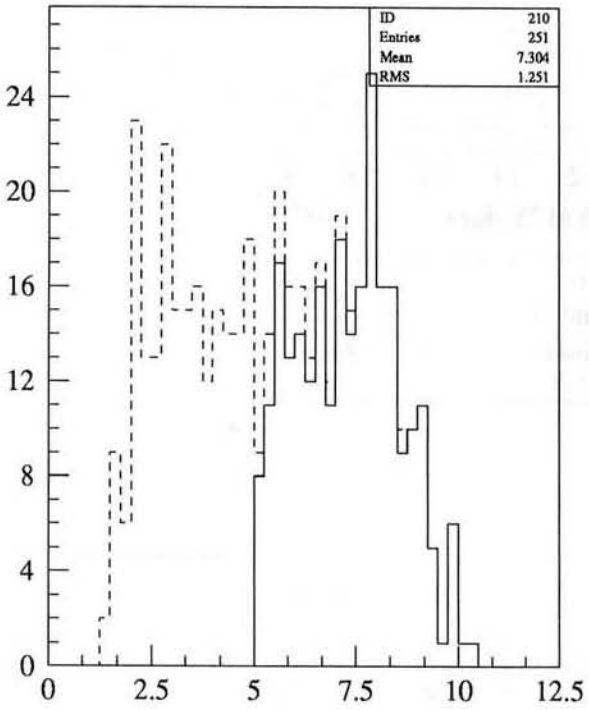

FEM ELES Et Default Clustering

Fig 96

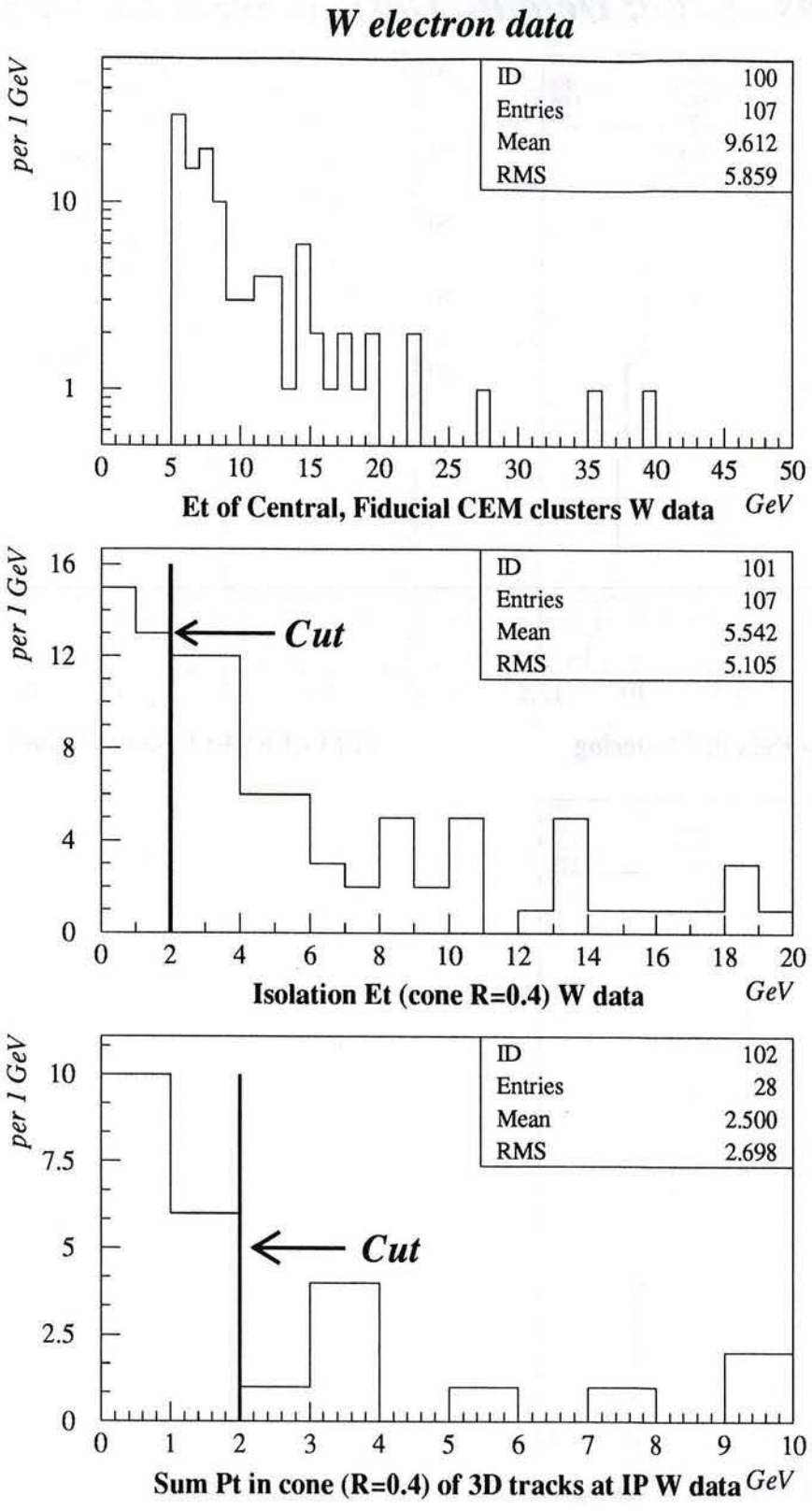
W electron data
per 1 GeV
ID 100
Entries 107
Mean 9.612
RMS 5.859
Et of Central, Fiducial CEM clusters W data GeV
per 1 GeV
ID 101
Entries 107
Mean 5.542
RMS 5.105
Cut
Isolation Et (cone R=0.4) W data GeV
per 1 GeV
ID 102
Entries 28
Mean 2.500
RMS 2.698
Cut
Sum Pt in cone (R=0.4) of 3D tracks at IP W data GeV

Fig 10a

09/03/93 19.54

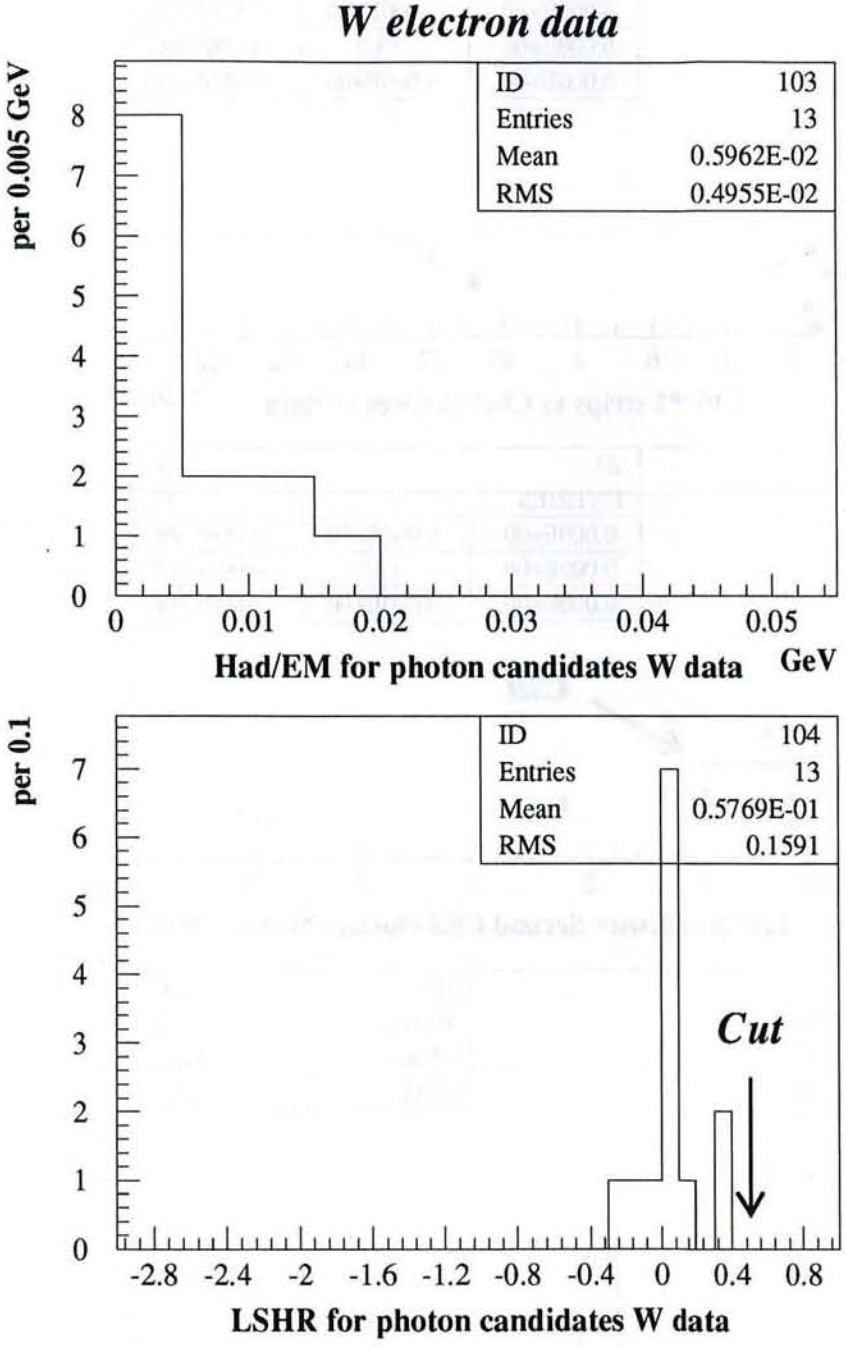

Fig 10b

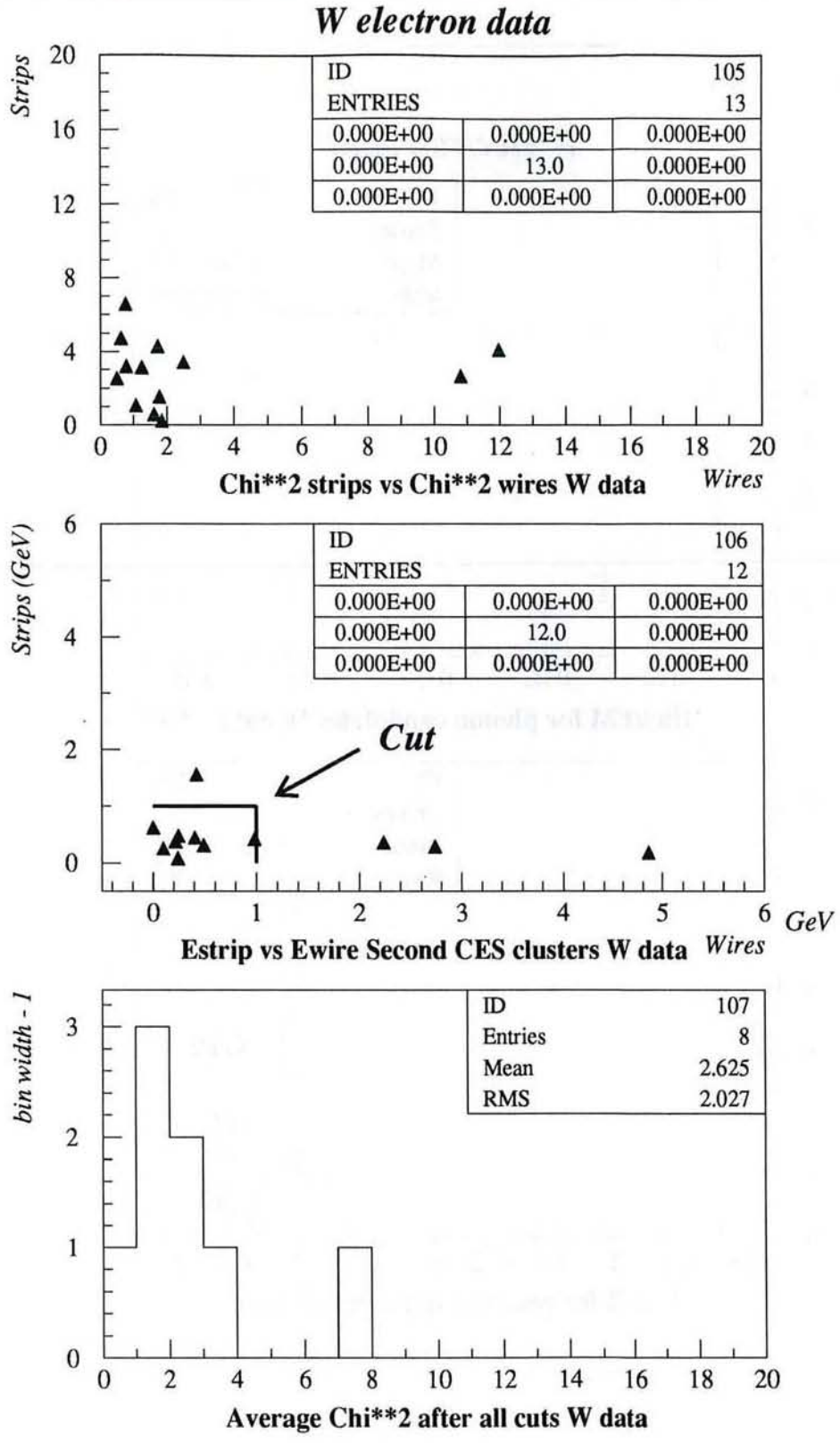
W electron data
Strips
ID 105
ENTRIES 13
0.000E+00 0.000E+00 0.000E+00
0.000E+00 13.0 0.000E+00
0.000E+00 0.000E+00 0.000E+00
Chi**2 strips vs Chi**2 wires W data
Wires
Strips (GeV)
ID 106
ENTRIES 12
0.000E+00 0.000E+00 0.000E+00
0.000E+00 12.0 0.000E+00
0.000E+00 0.000E+00 0.000E+00
Cut
GeV
Estrip vs Ewire Second CES clusters W data
Wires
bin width - 1
ID 107
Entries 8
Mean 2.625
RMS 2.027
Average Chi**2 after all cuts W data

Fig 10c

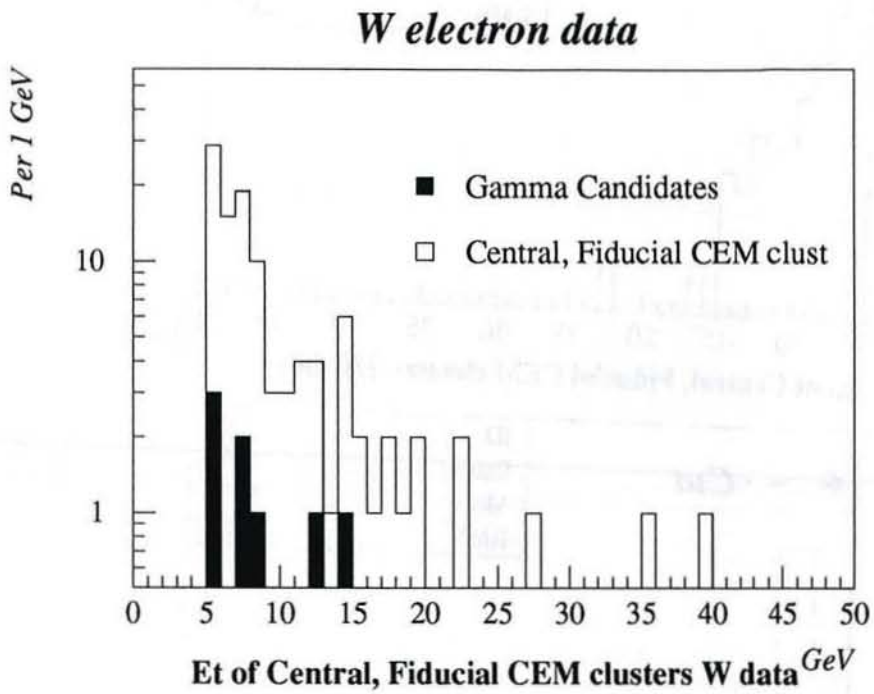
W electron data
Per 1 GeV
10
1
Gamma Candidates
Central, Fiducial CEM clust
0
5
10
15
20
25
30
35
40
45
50
Et of Central, Fiducial CEM clusters W data GeV

Fig 10d

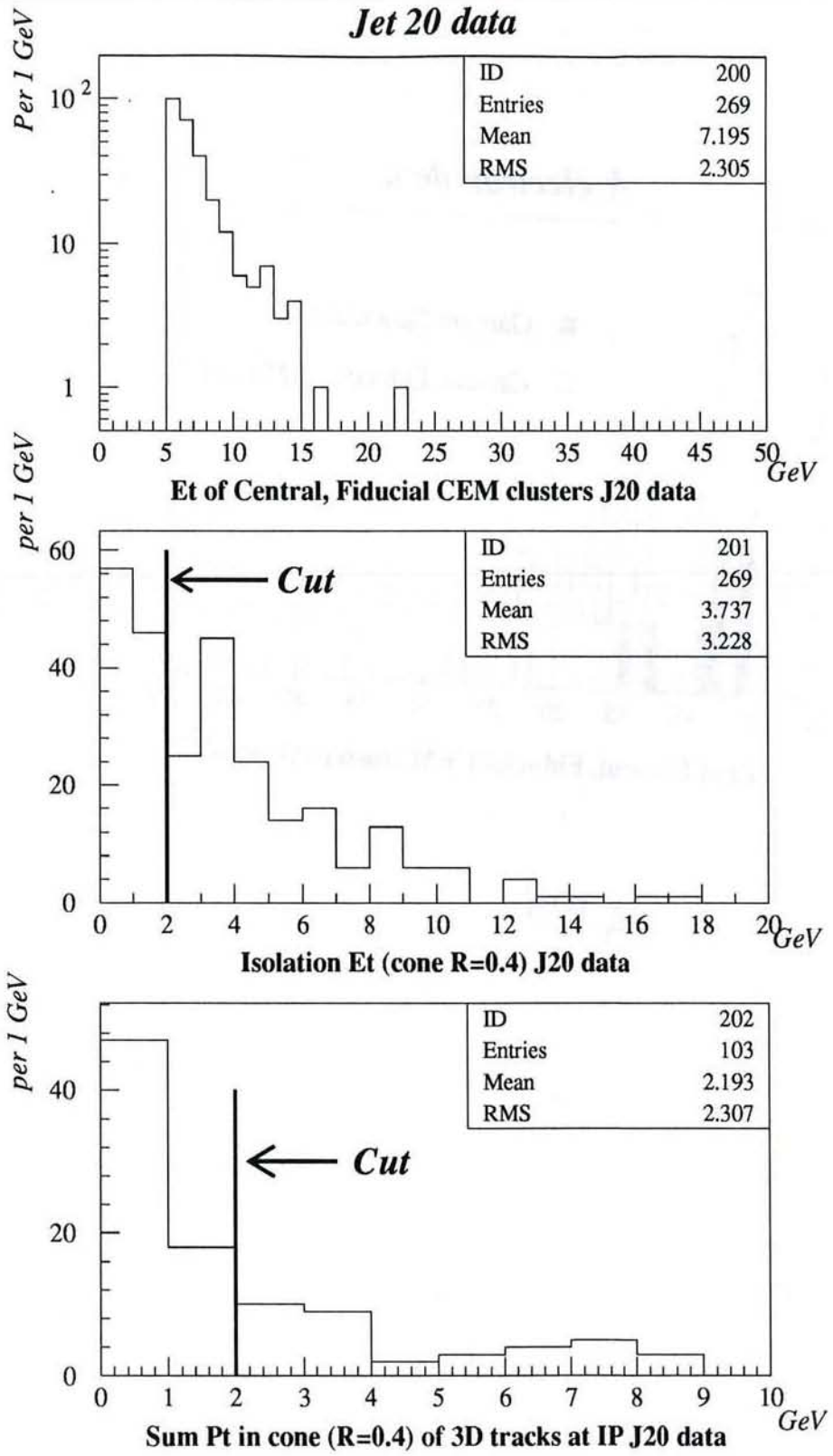
Jet 20 data
Per 1 GeV
ID 200
Entries 269
Mean 7.195
RMS 2.305
GeV
Et of Central, Fiducial CEM clusters J20 data
per 1 GeV
Cut
ID 201
Entries 269
Mean 3.737
RMS 3.228
GeV
Isolation Et (cone R=0.4) J20 data
per 1 GeV
Cut
ID 202
Entries 103
Mean 2.193
RMS 2.307
GeV
Sum Pt in cone (R=0.4) of 3D tracks at IP J20 data

Fig 11a

09/03/93 20.02

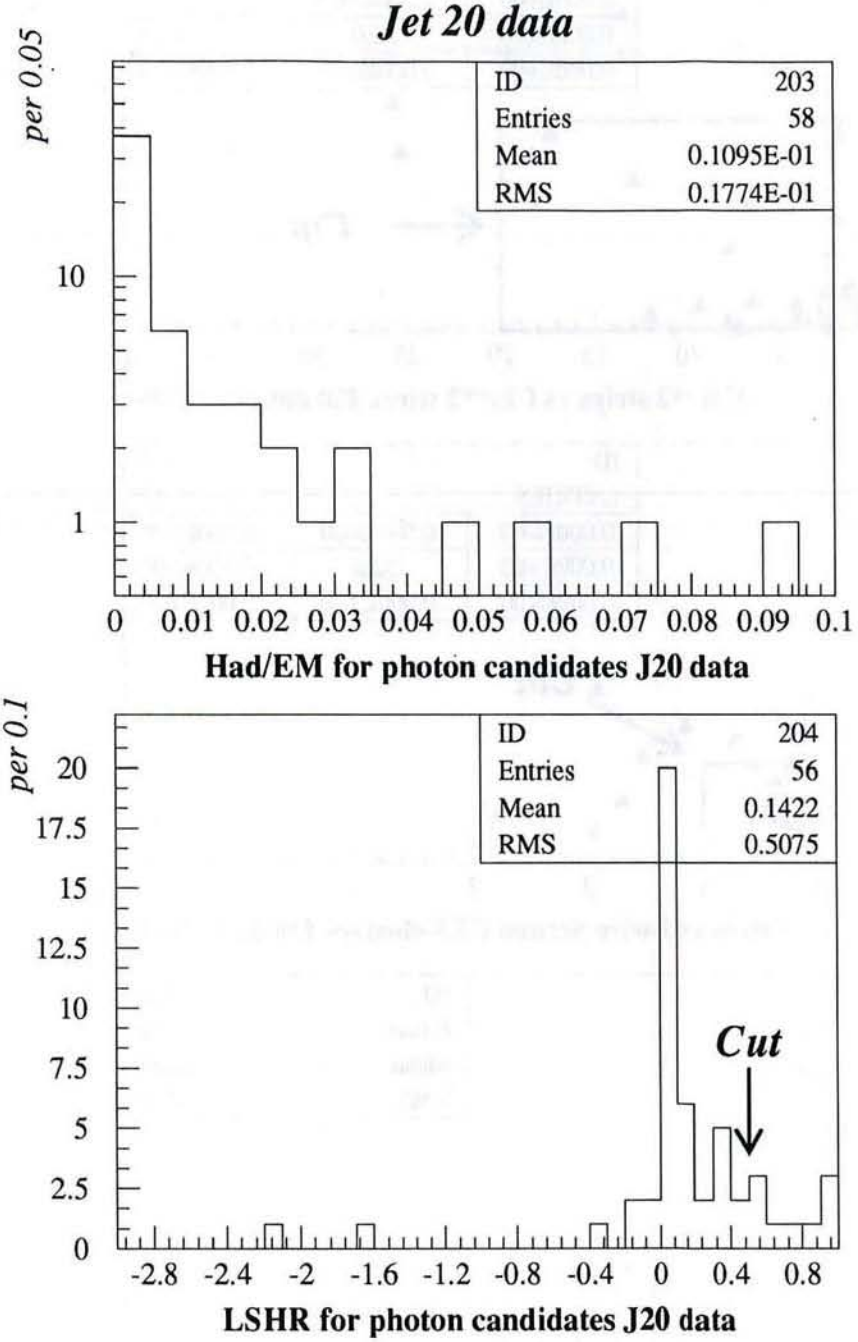

Fig 116

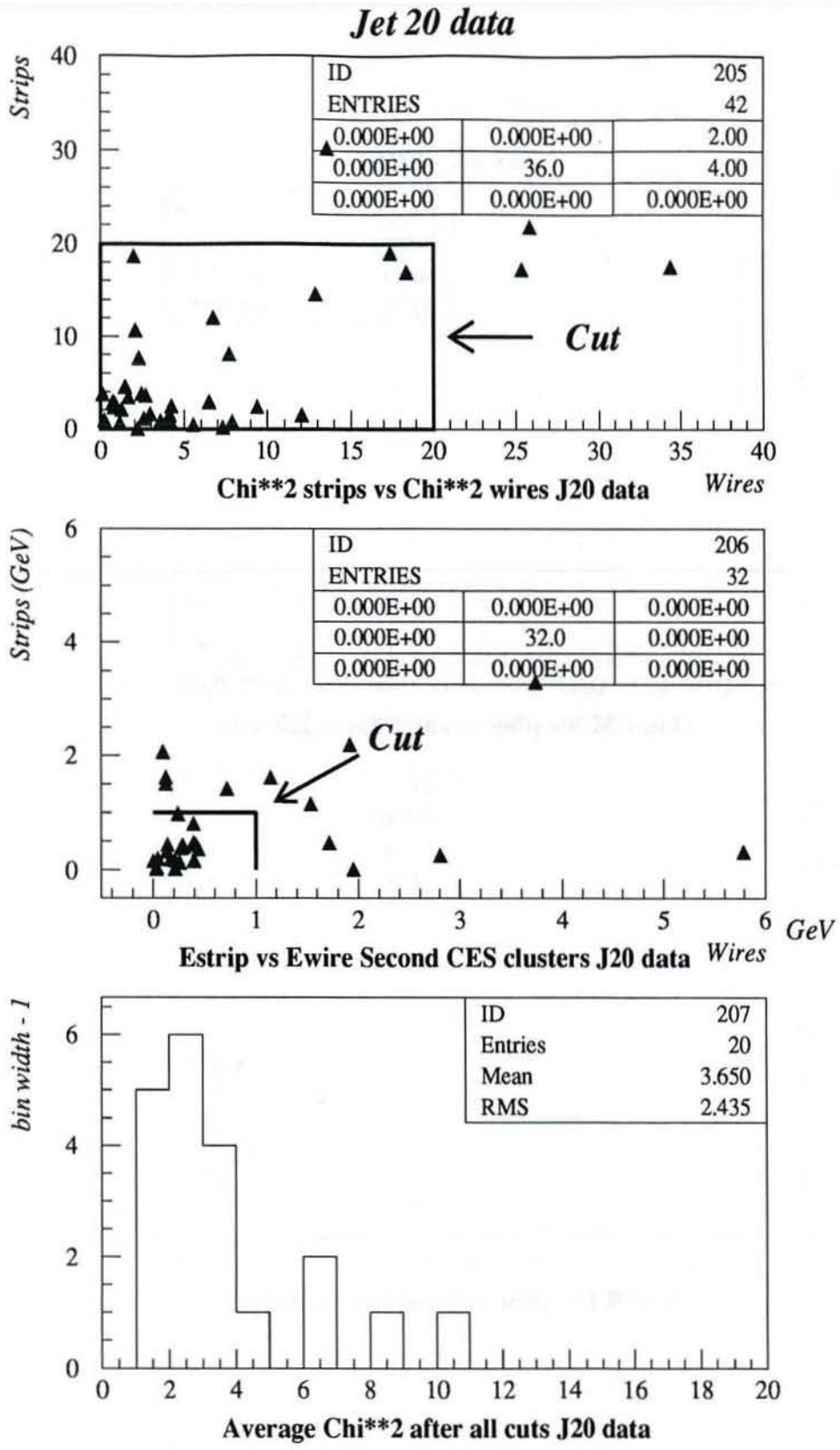
Jet 20 data
Strips
ID 205
ENTRIES 42
0.000E+00 0.000E+00 2.00
0.000E+00 36.0 4.00
0.000E+00 0.000E+00 0.000E+00
Cut
Chi**2 strips vs Chi**2 wires J20 data
Wires
Strips (GeV)
ID 206
ENTRIES 32
0.000E+00 0.000E+00 0.000E+00
0.000E+00 32.0 0.000E+00
0.000E+00 0.000E+00 0.000E+00
Cut
GeV
Estrip vs Ewire Second CES clusters J20 data
Wires
bin width - 1
ID 207
Entries 20
Mean 3.650
RMS 2.435
Average Chi**2 after all cuts J20 data

Fig 11c

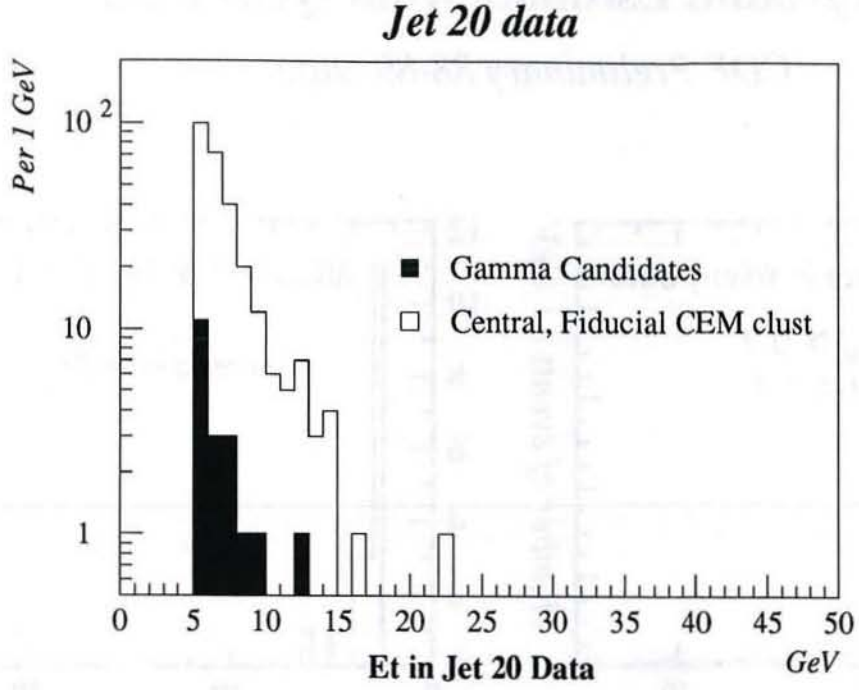
Jet 20 data
Per 1 GeV
10 2
10
1
Gamma Candidates
Central, Fiducial CEM clust
0
5
10
15
20
25
30
35
40
45
50
Et in Jet 20 Data
GeV

Fig 11d

Background Estimate from QCD data

CDF Preliminary 88-89 Data

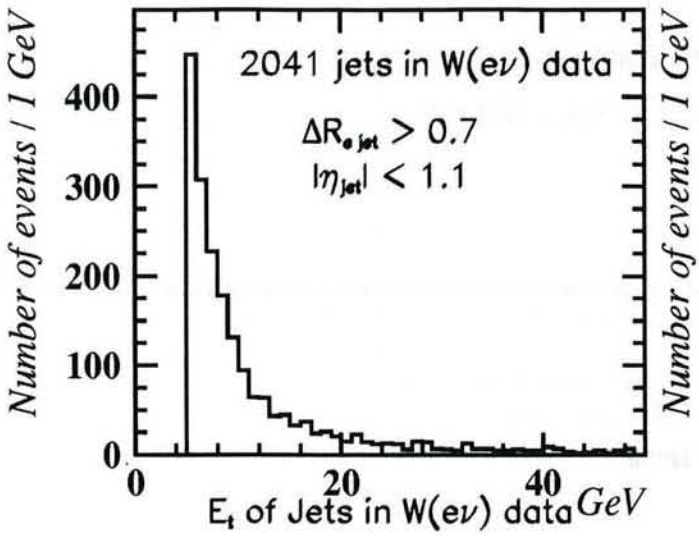

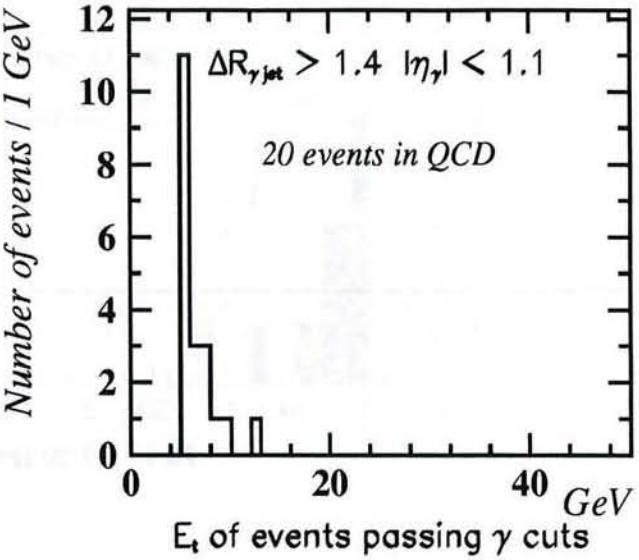

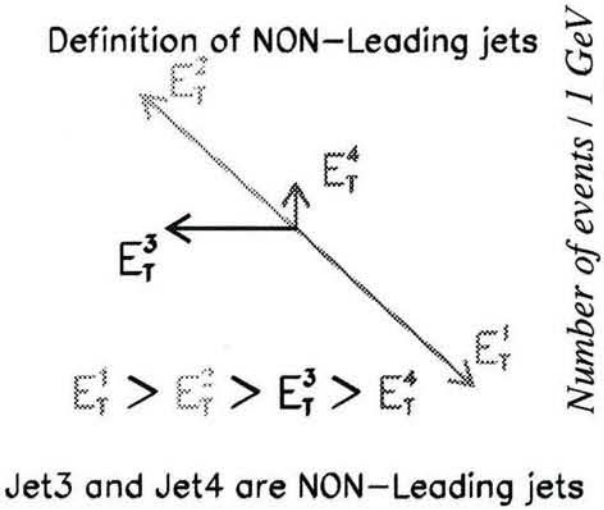

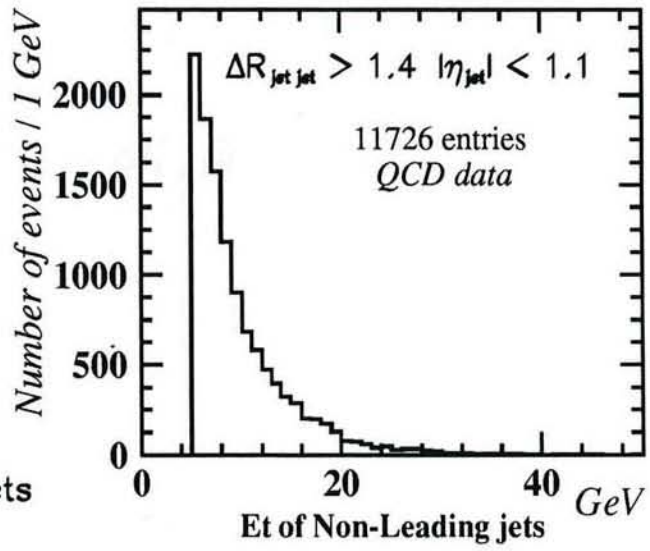

Fig 12a

Et spectra of jets in the inclusive W/Z data

CDF Preliminary 88-89 Data

$\Delta R_{\text{jet lepton}} > 0.7 \quad |\eta_{\text{jet}}| < 1.1$

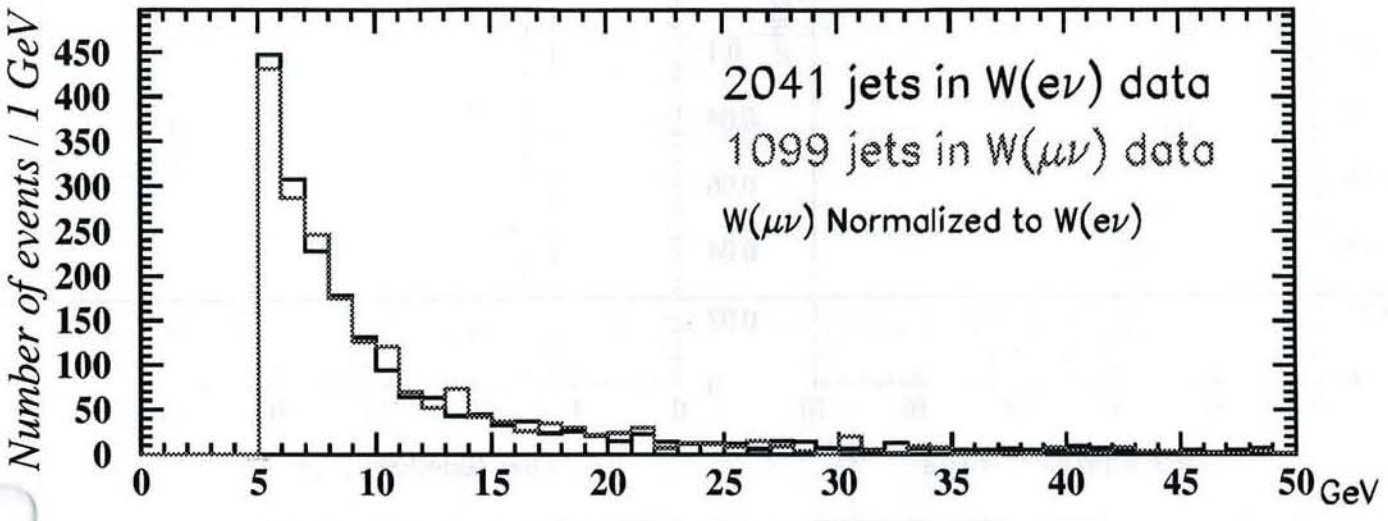

Et of Jets in W data

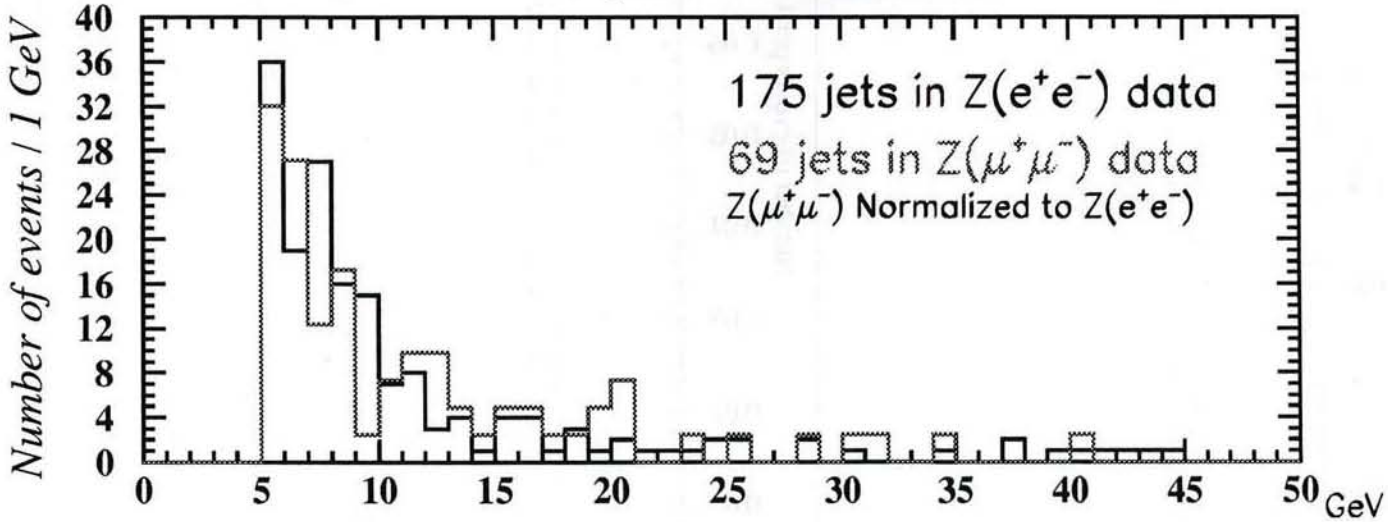

Et of Jets in Z data

Fig 12b

09/03/93 22.11

Fake rate in all four data samples

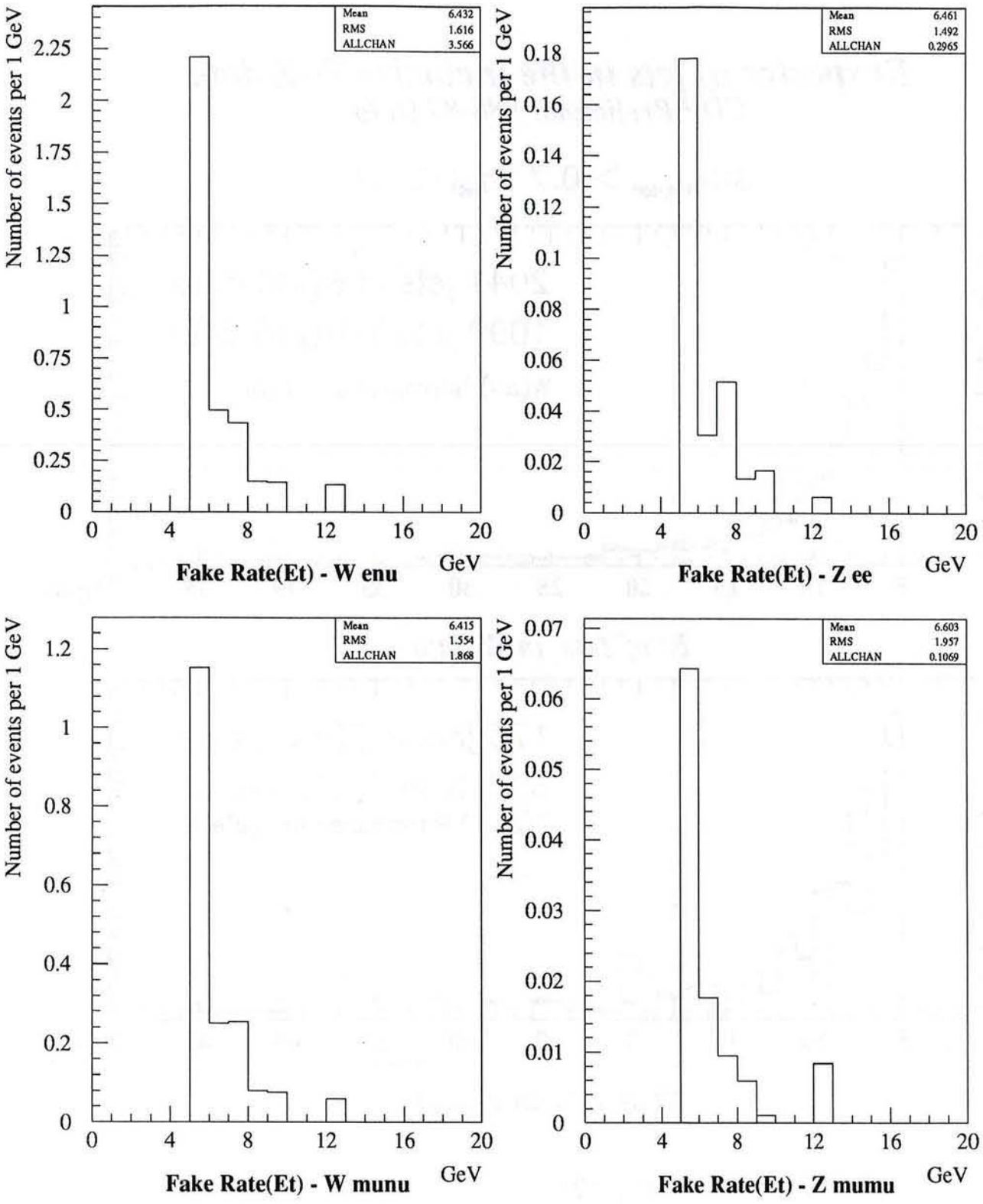

Fig 12c

MC Signal vs Observed Events W/Z γ

CDF Preliminary 88-89 Data

$\Delta R_{\gamma\,\text{lepton}} > 0.7 \quad |\eta_\gamma| < 1.1$

Shaded Histogram Signal MC

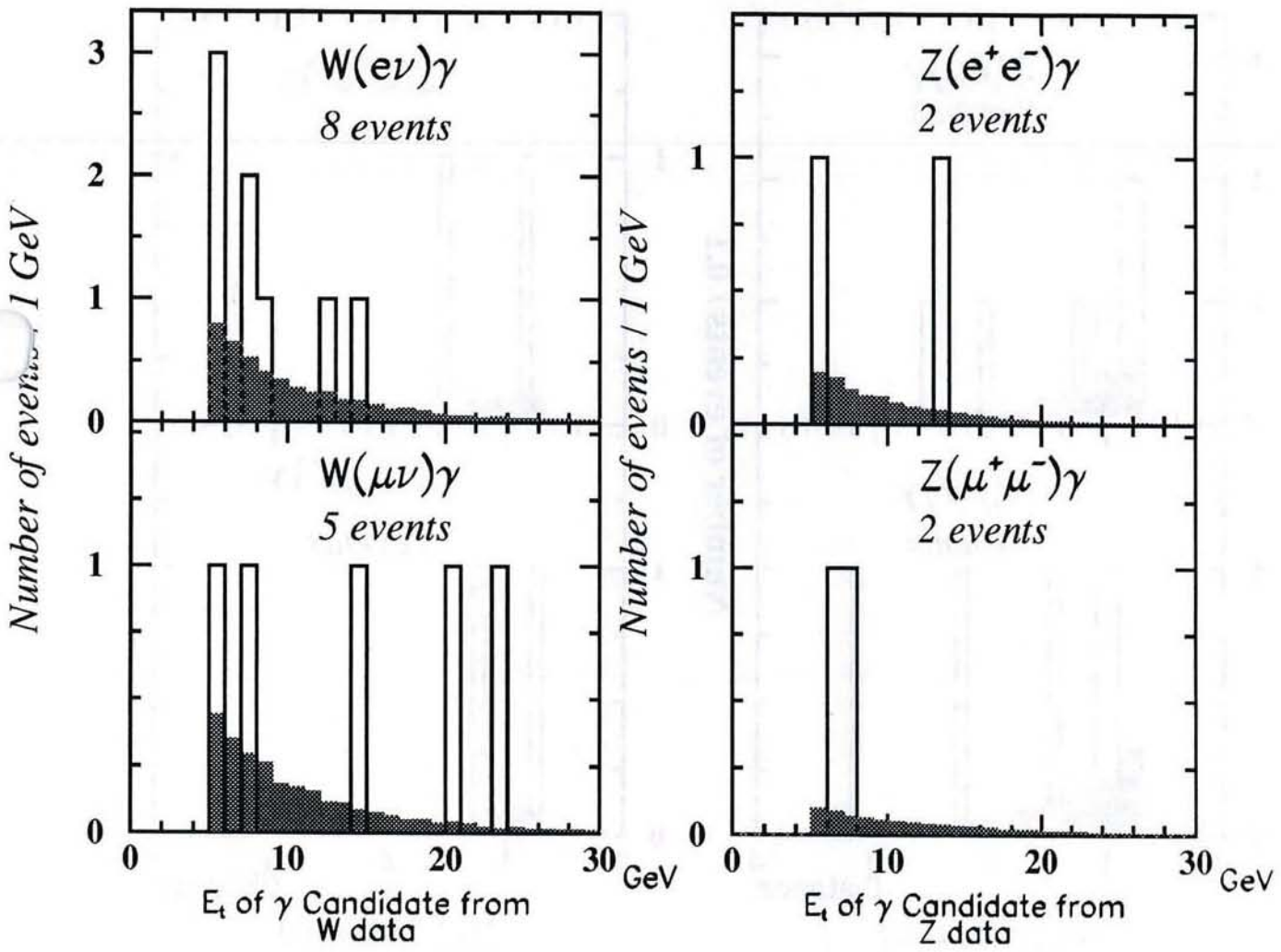

Fig 13a

MC Signal vs Observed Events W/Z γ

CDF Preliminary 88-89 Data

$\Delta R_{\gamma\ \text{lepton}} > 0.7 \quad |\eta_\gamma| < 1.1$

Shaded Histogram Signal MC

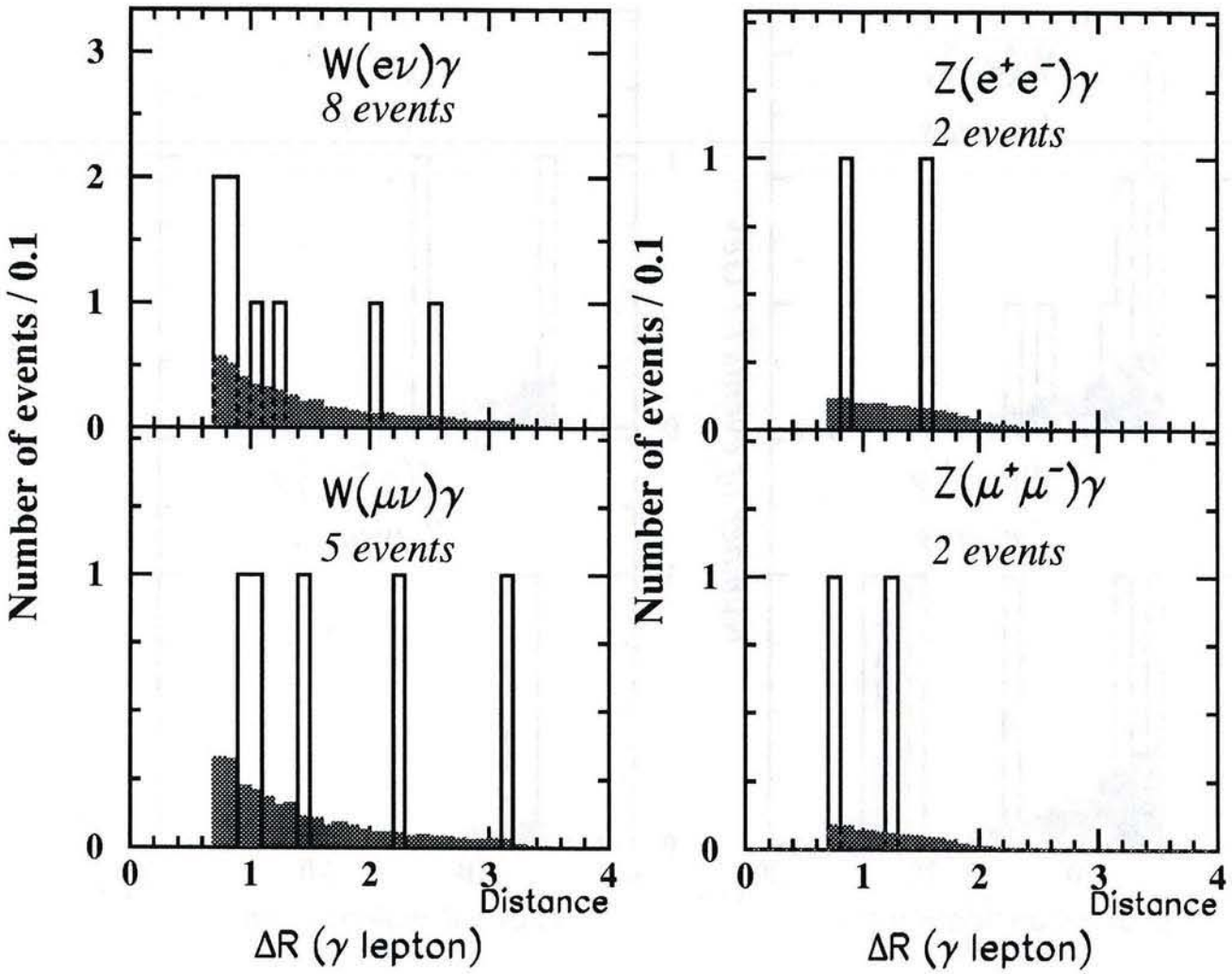

Fig 13b

MC Signal vs Observed Events W/Zγ

CDF Preliminary 88-89 Data

$\Delta R_{\gamma\ \text{lepton}} > 0.7\ |\eta_\gamma| < 1.1$

*Shaded Histogram Signal MC*10*

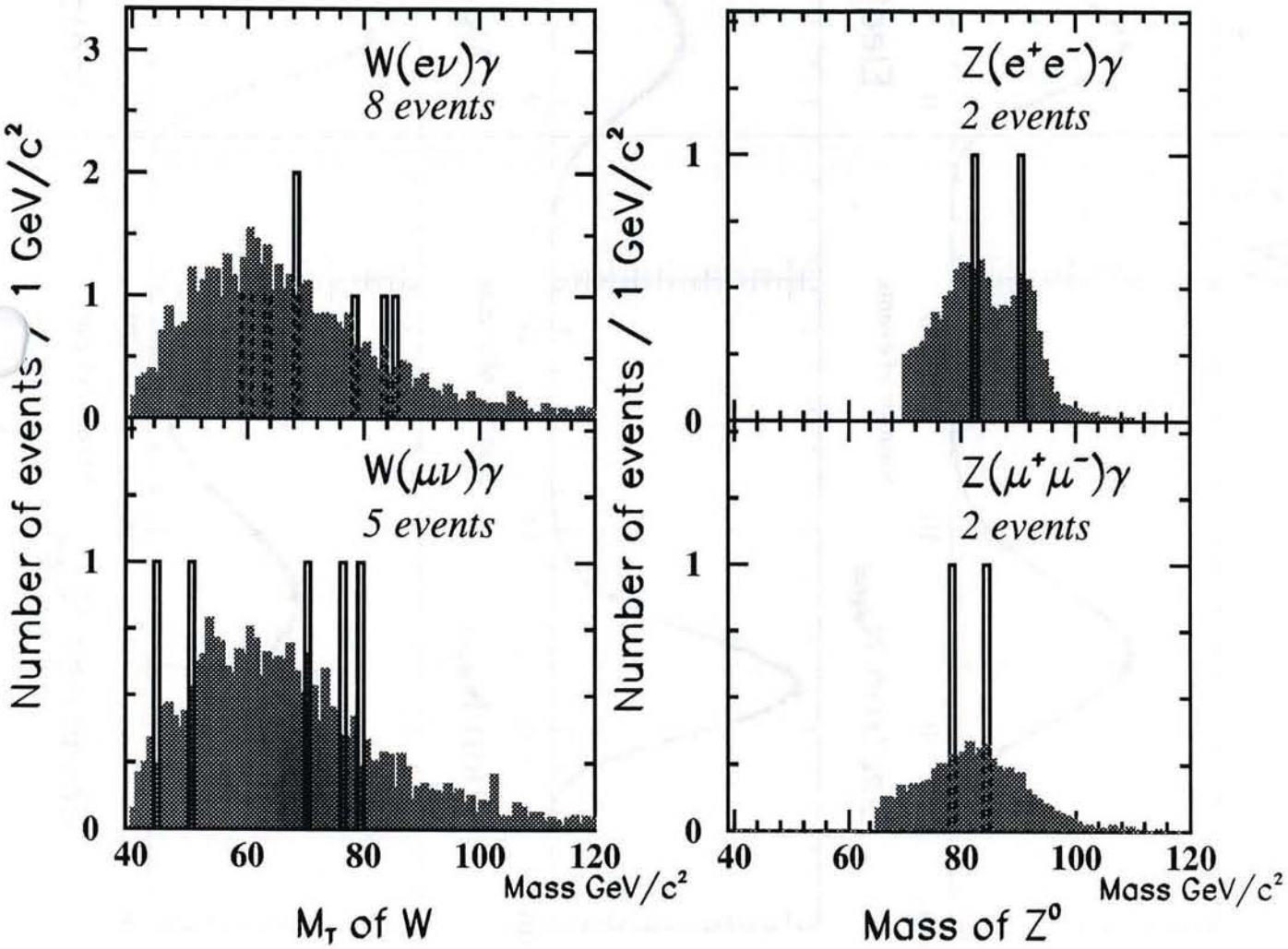

Fig 13c

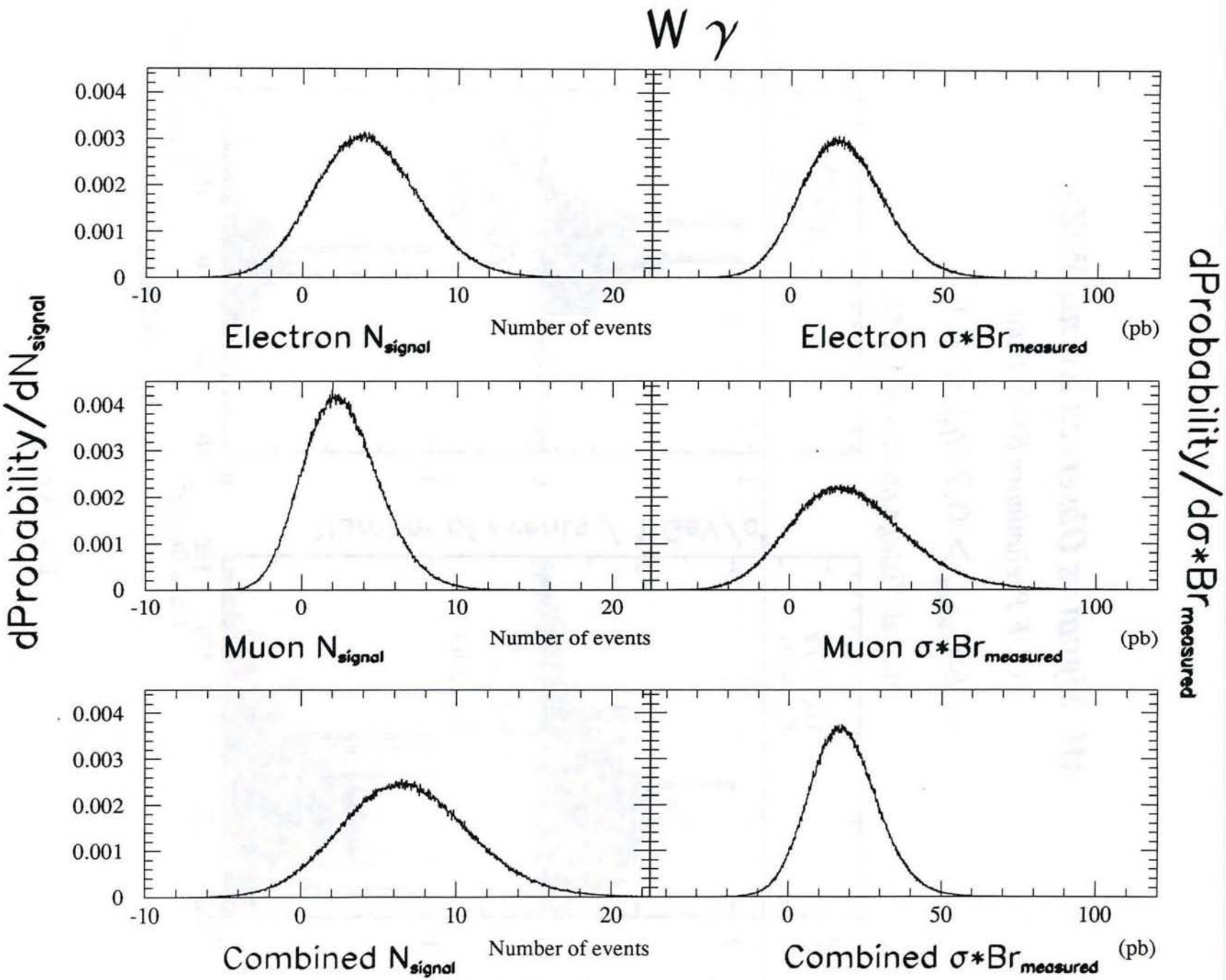
W γ
dProbability/dN_signal
dProbability/dσ*Br_measured
0.004
0.003
0.002
0.001
0
-10
0
10
20
50
100
Electron N_signal
Number of events
Electron σ*Br_measured
(pb)
Muon N_signal
Number of events
Muon σ*Br_measured
(pb)
Combined N_signal
Number of events
Combined σ*Br_measured
(pb)

Fig

$\angle\gamma$

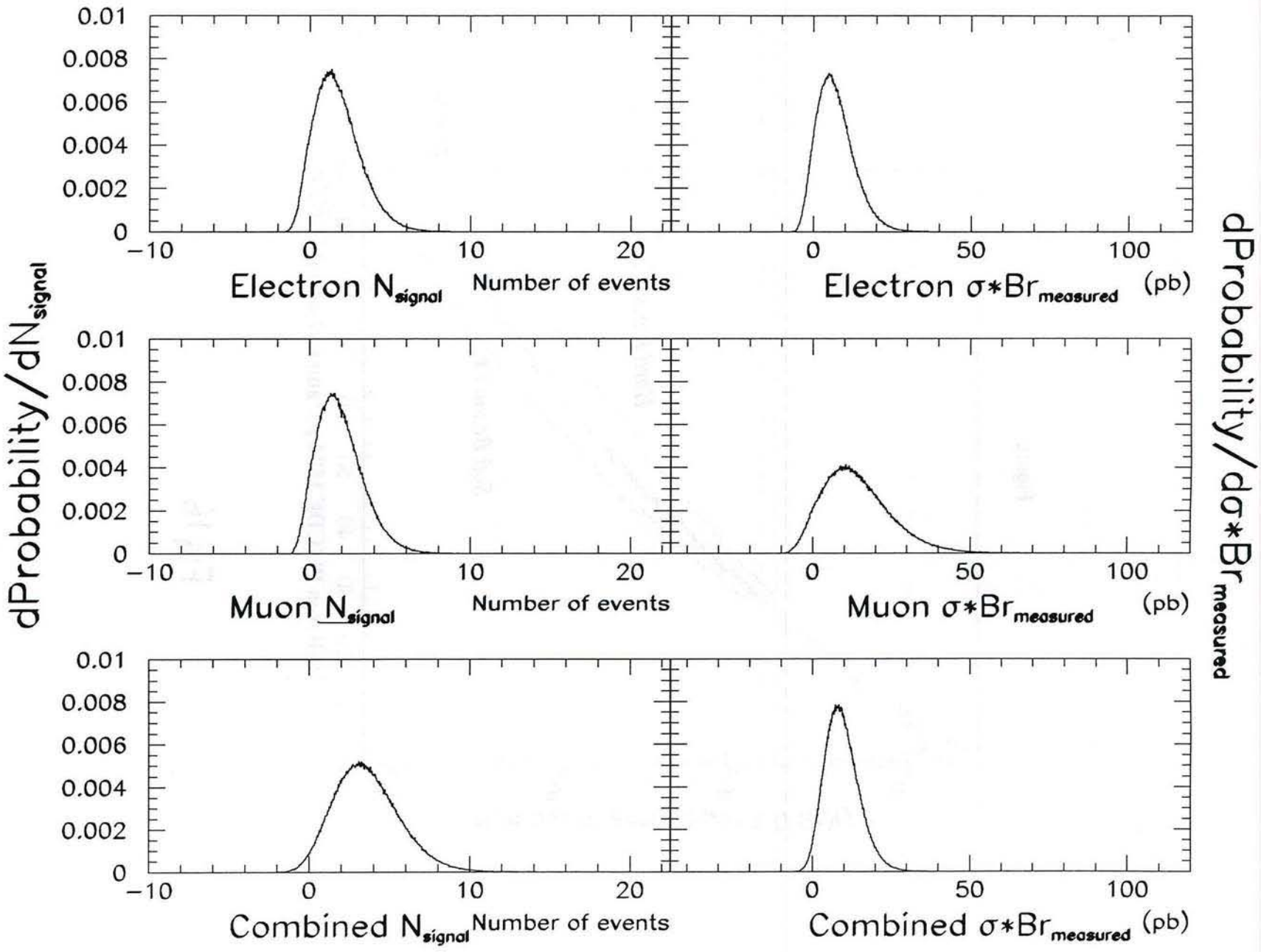

Fig 15

Figure

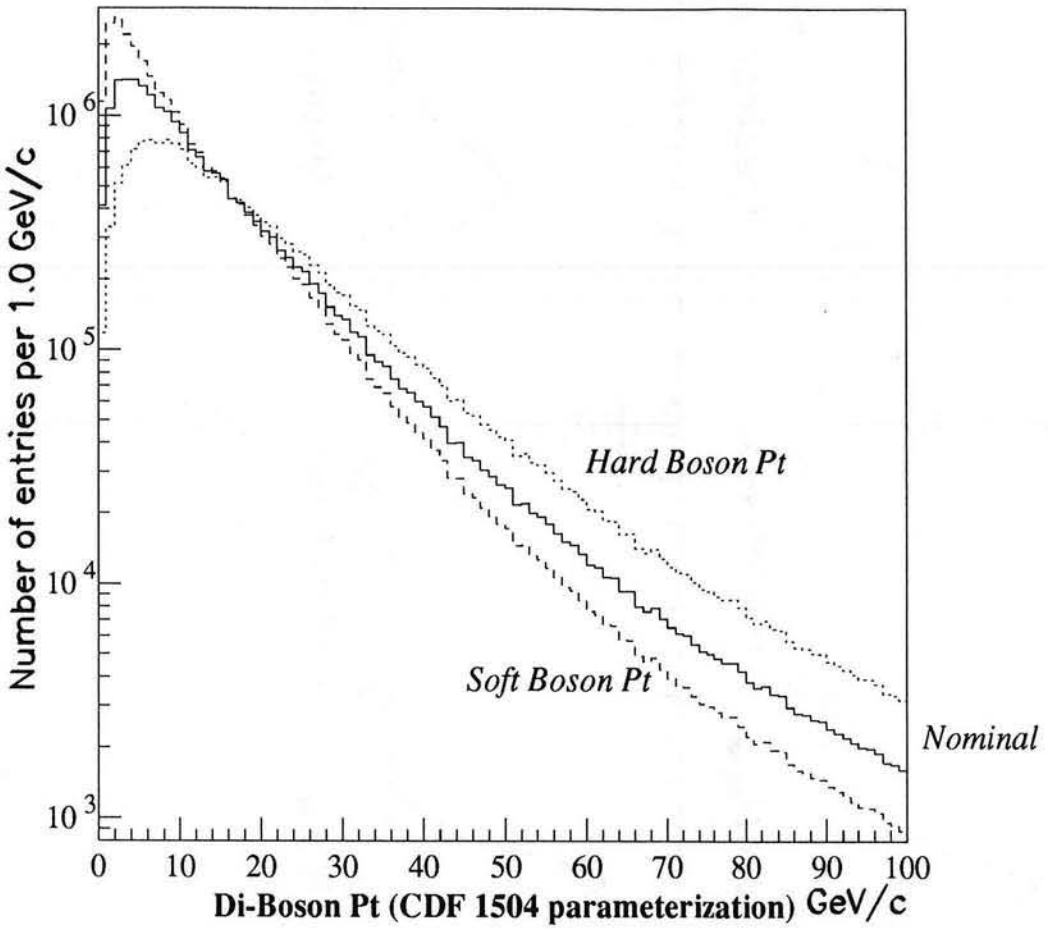

Fig 16

Electron $W^{\pm}\gamma$

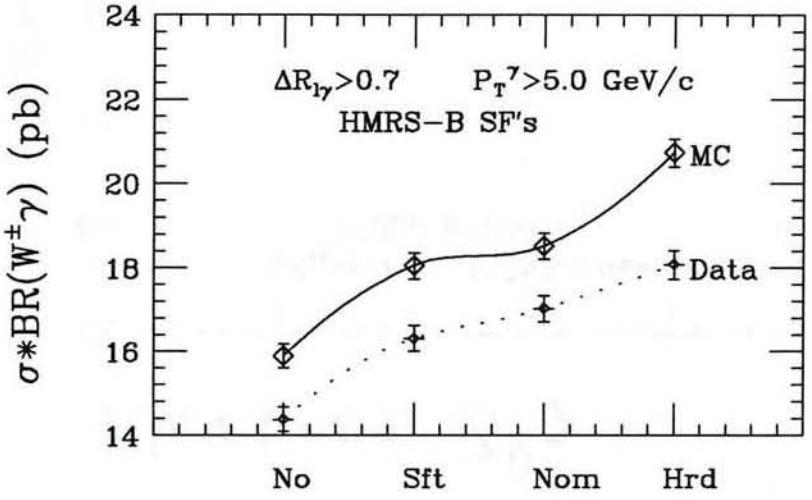

Muon $W^{\pm}\gamma$

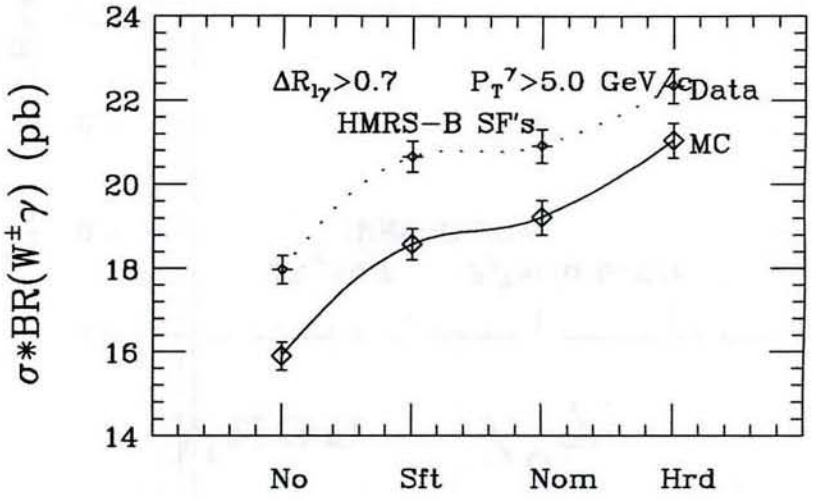

Electron $Z^0\gamma$

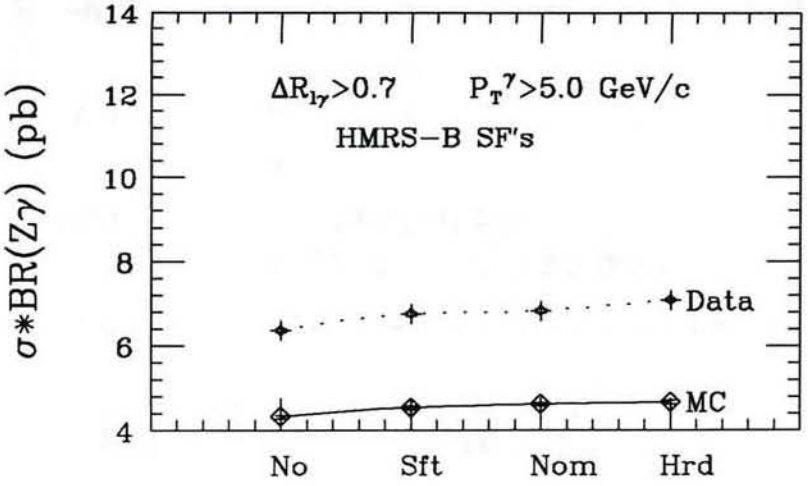

Muon $Z^0\gamma$

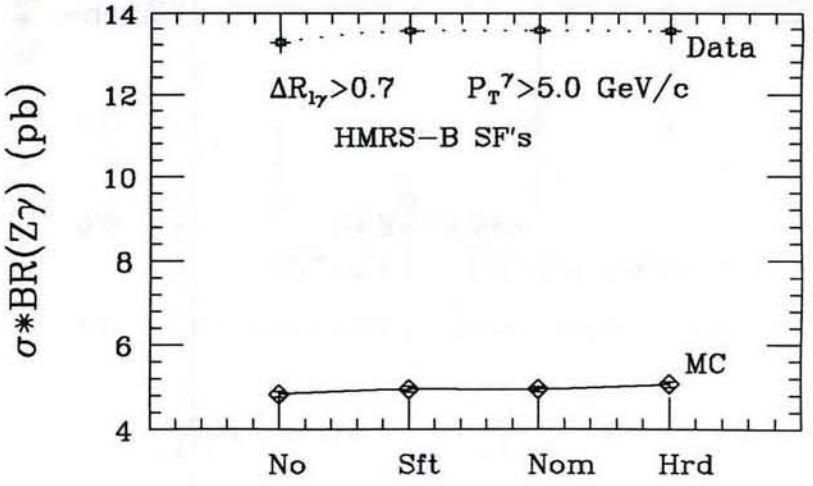

Fig 17a

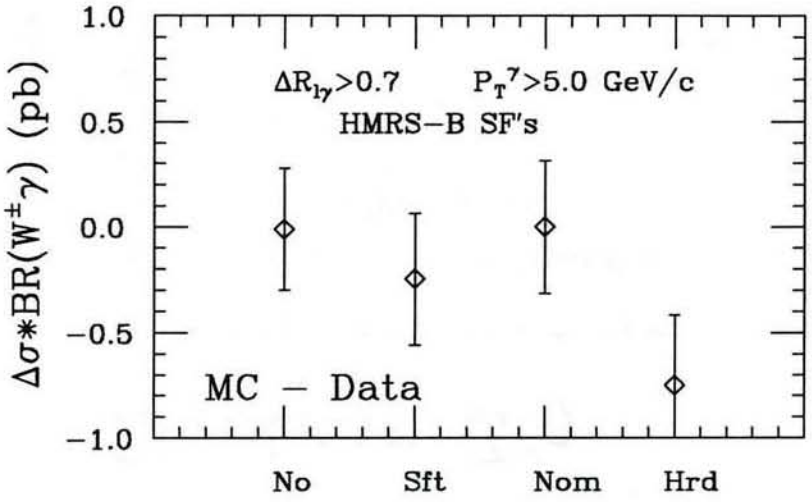
Electron $W^{\pm}\gamma$
$\Delta R_{l\gamma}>0.7$ $P_T^{\gamma}>5.0$ GeV/c
HMRS-B SF's
MC − Data
$\Delta\sigma*BR(W^{\pm}\gamma)$ (pb)
1.0
0.5
0.0
−0.5
−1.0
No
Sft
Nom
Hrd

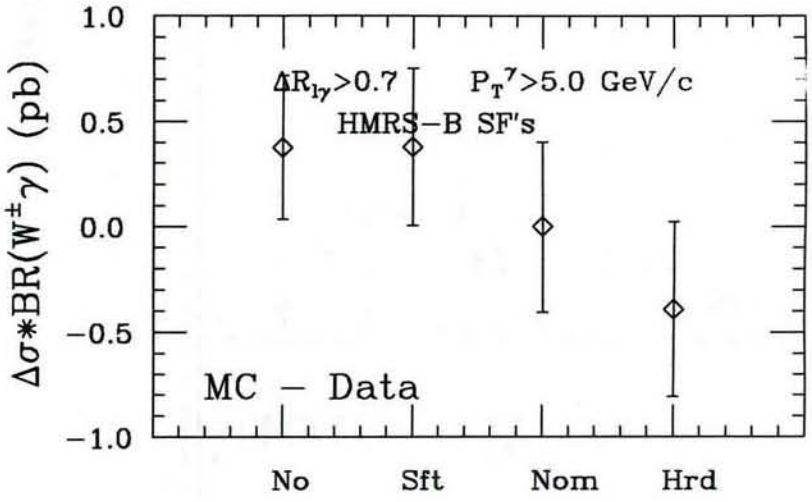
Muon $W^{\pm}\gamma$
$\Delta R_{l\gamma}>0.7$ $P_T^{\gamma}>5.0$ GeV/c
HMRS-B SF's
MC − Data
$\Delta\sigma*BR(W^{\pm}\gamma)$ (pb)
1.0
0.5
0.0
−0.5
−1.0
No
Sft
Nom
Hrd

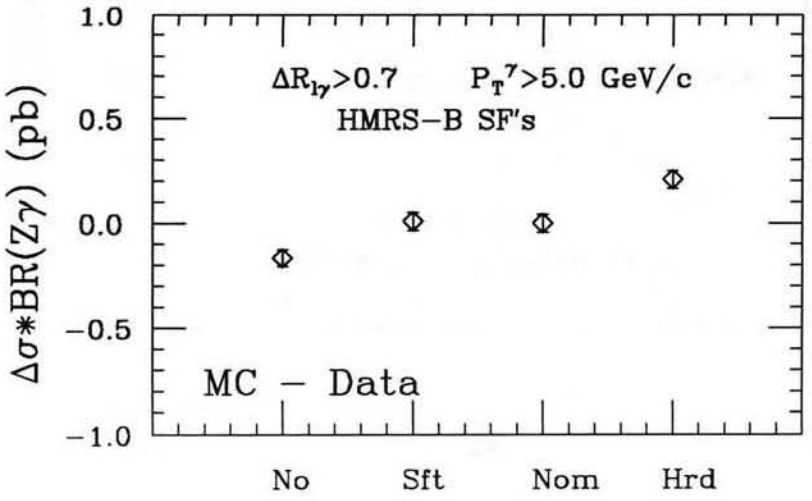
Electron $Z^0\gamma$
$\Delta R_{l\gamma}>0.7$ $P_T^{\gamma}>5.0$ GeV/c
HMRS-B SF's
MC − Data
$\Delta\sigma*BR(Z\gamma)$ (pb)
1.0
0.5
0.0
−0.5
−1.0
No
Sft
Nom
Hrd

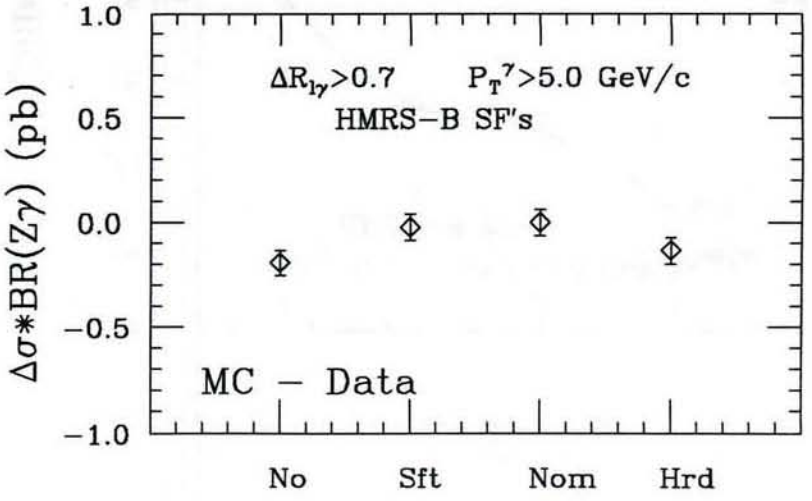
Muon $Z^0\gamma$
$\Delta R_{l\gamma}>0.7$ $P_T^{\gamma}>5.0$ GeV/c
HMRS-B SF's
MC − Data
$\Delta\sigma*BR(Z\gamma)$ (pb)
1.0
0.5
0.0
−0.5
−1.0
No
Sft
Nom
Hrd

Fig 17

Electron $W^{\pm}\gamma$

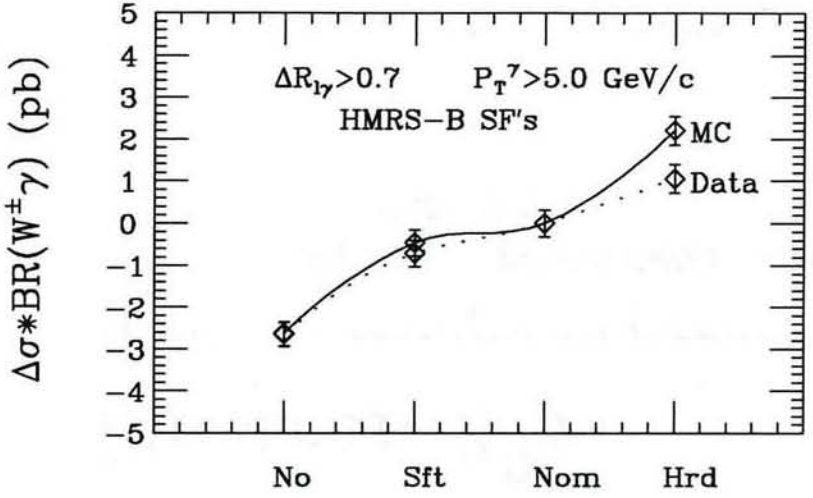

Muon $W^{\pm}\gamma$

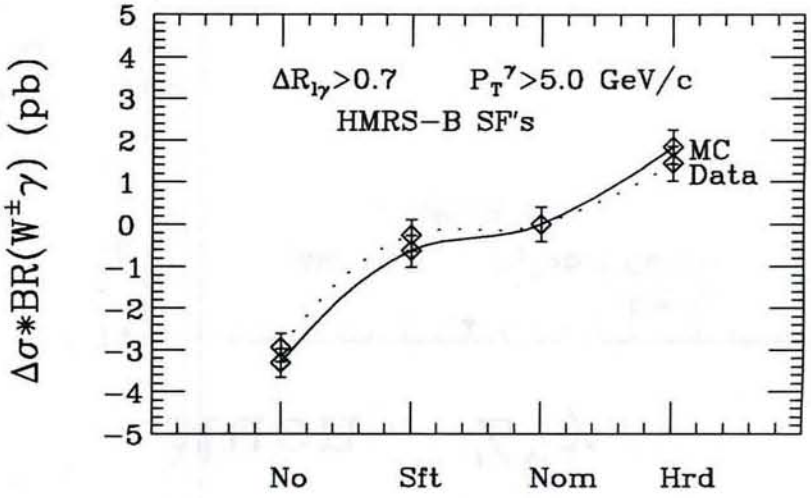

Electron $Z^0\gamma$

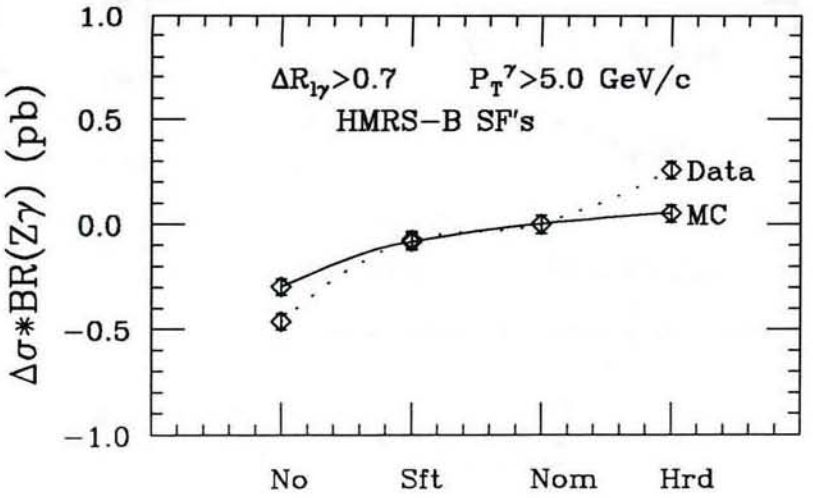

Muon $Z^0\gamma$

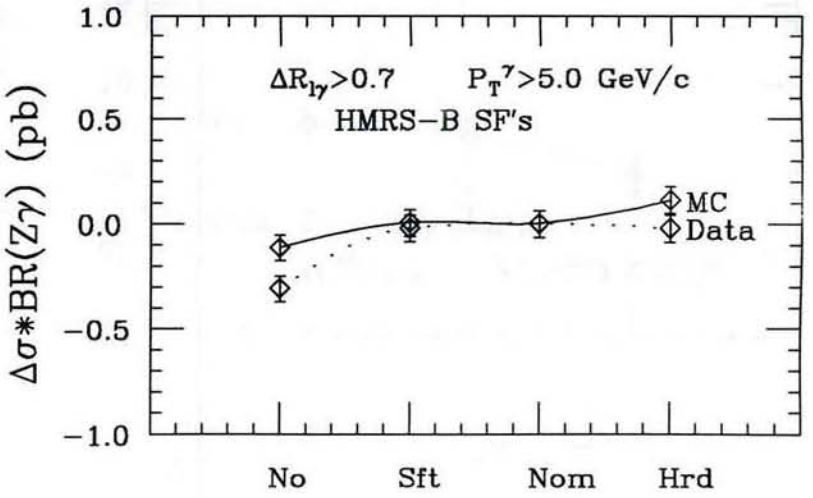

Fig 17c

Electron $W^{\pm}\gamma$

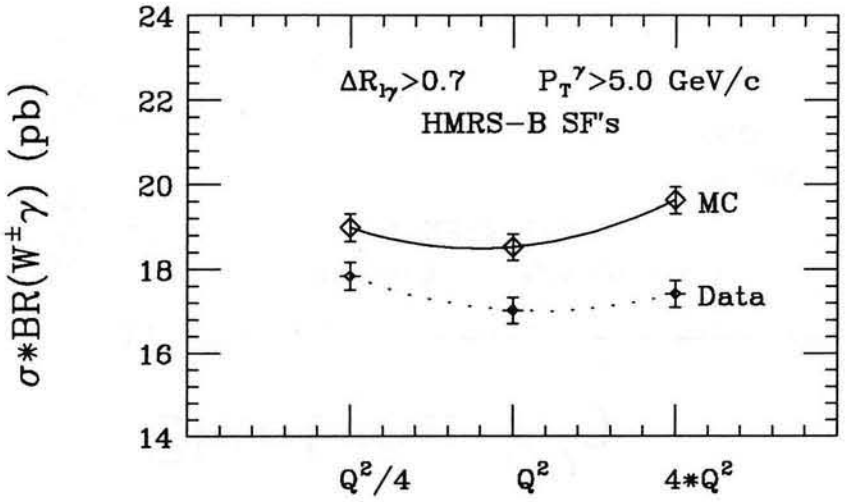

Muon $W^{\pm}\gamma$

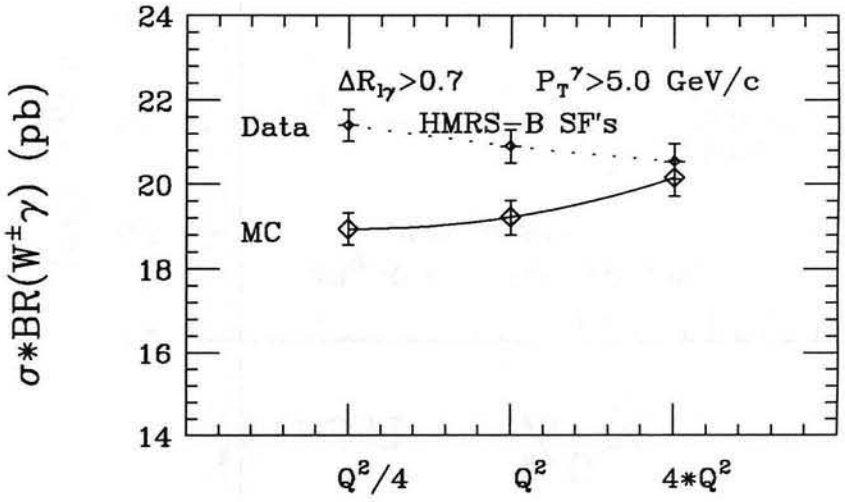

Electron $Z^0\gamma$

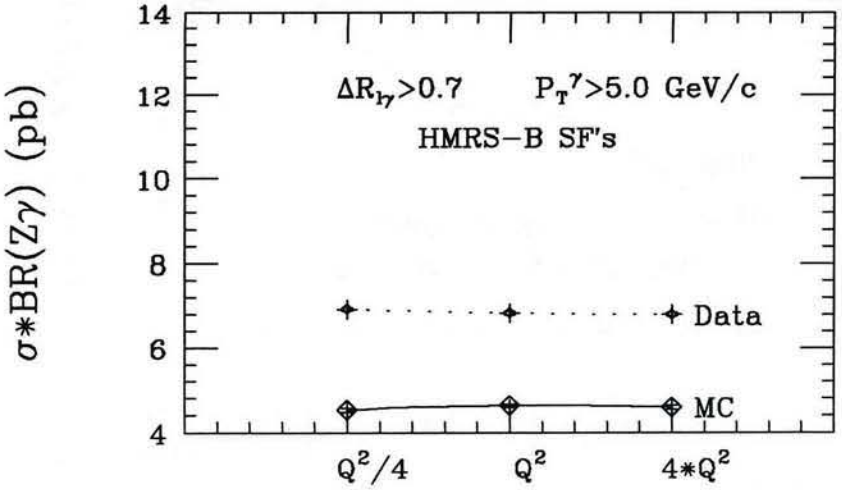

Muon $Z^0\gamma$

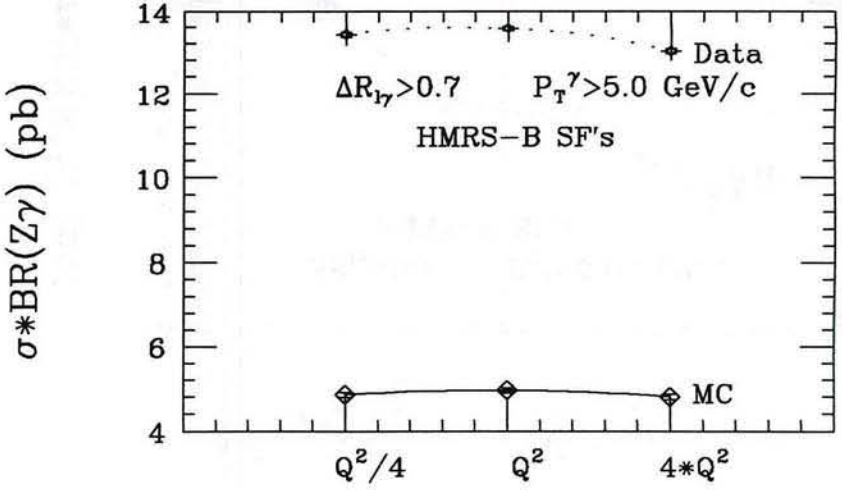

Fig 18

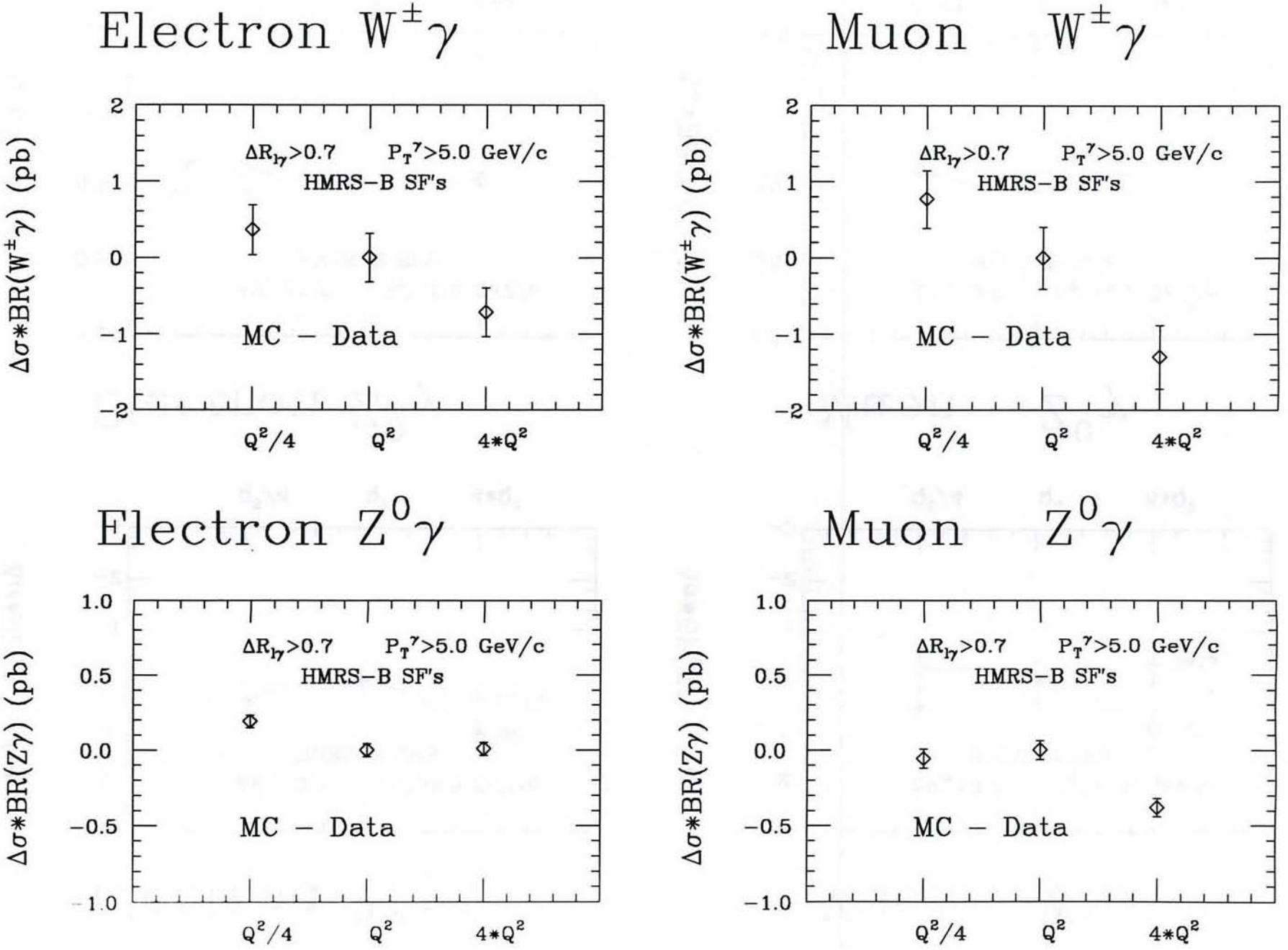
Electron $W^{\pm}\gamma$
Muon $W^{\pm}\gamma$
Electron $Z^0\gamma$
Muon $Z^0\gamma$
$\Delta\sigma*BR(W^{\pm}\gamma)$ (pb)
$\Delta\sigma*BR(Z\gamma)$ (pb)
$\Delta R_{l\gamma}>0.7$ $P_T^{\gamma}>5.0$ GeV/c
HMRS-B SF's
MC − Data
$Q^2/4$
Q^2
$4*Q^2$

Fig 18b

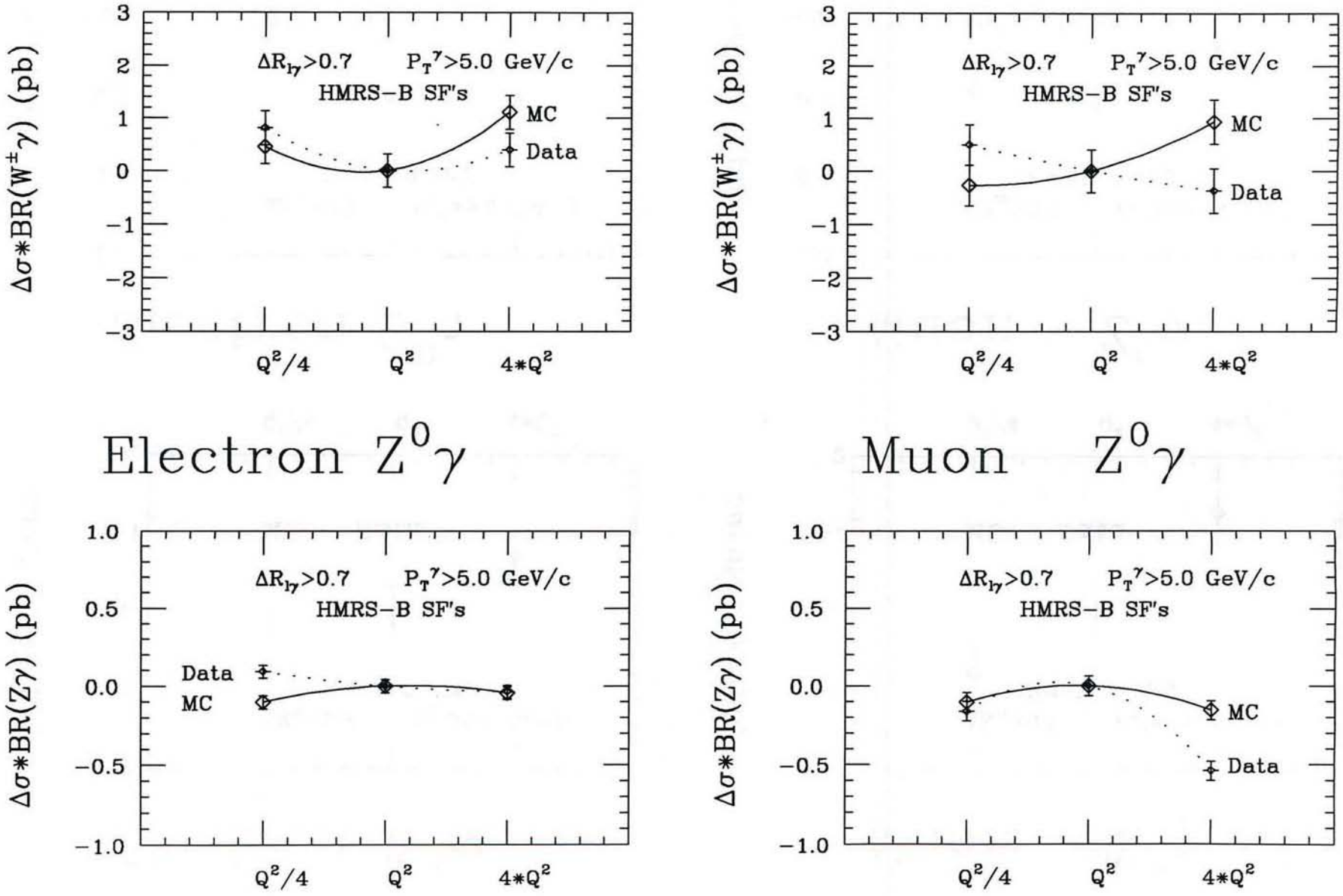
Electron $W^{\pm}\gamma$
Muon $W^{\pm}\gamma$
Electron $Z^0\gamma$
Muon $Z^0\gamma$
$\Delta\sigma*BR(W^{\pm}\gamma)$ (pb)
$\Delta\sigma*BR(Z\gamma)$ (pb)
$\Delta R_{l\gamma}>0.7$ $P_T^{\gamma}>5.0$ GeV/c
HMRS-B SF's
MC
Data
$Q^2/4$
Q^2
$4*Q^2$

Fig 18c

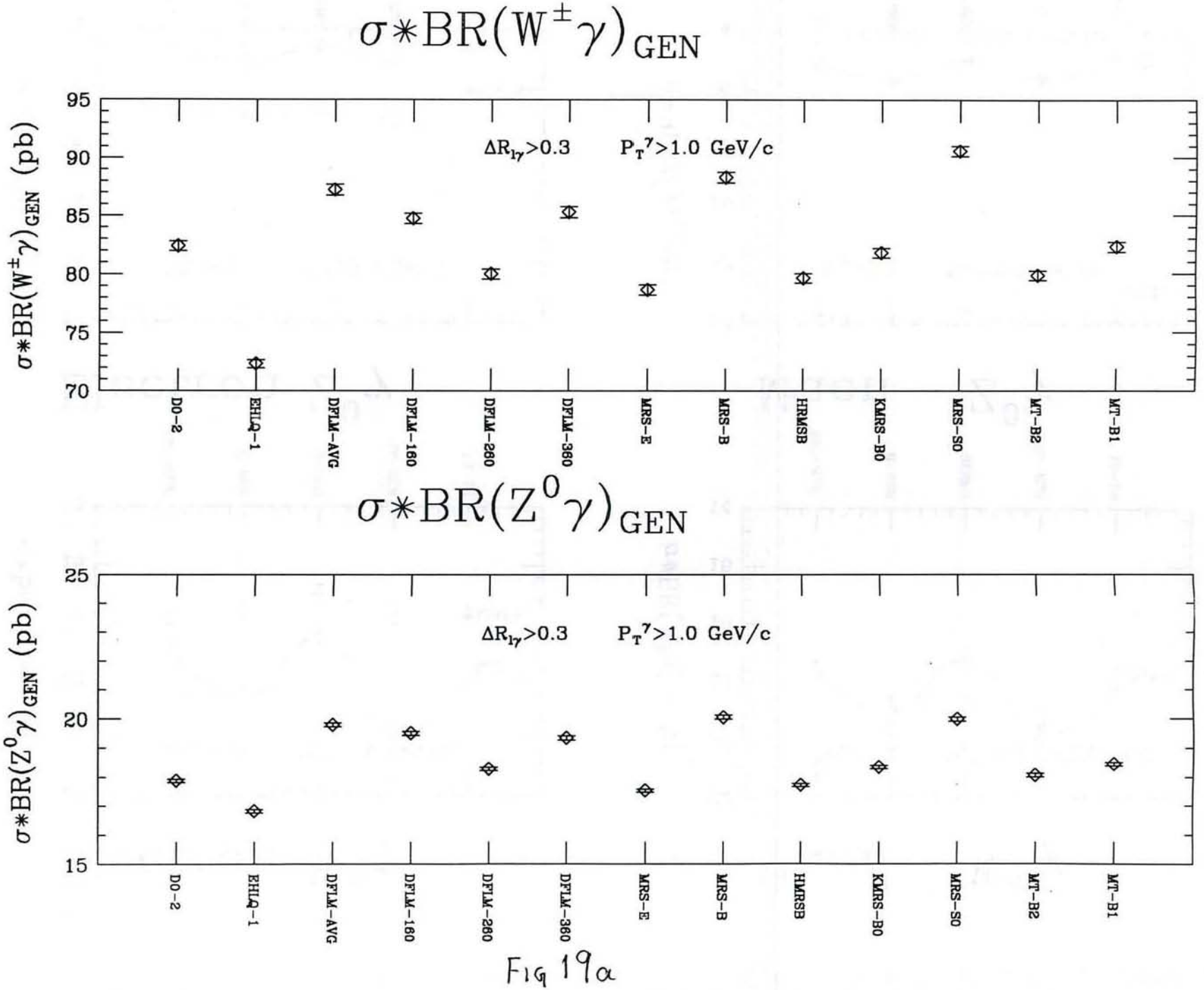
$\sigma * BR(W^{\pm}\gamma)_{GEN}$
$\sigma * BR(W^{\pm}\gamma)_{GEN}$ (pb)
95
90
85
80
75
70
$\Delta R_{l\gamma} > 0.3$
$P_T^{\gamma} > 1.0$ GeV/c
DO-2
EHLQ-1
DFLM-AVG
DFLM-160
DFLM-200
DFLM-300
MRS-E
MRS-B
HMRSB
KMRS-B0
MRS-S0
MT-B2
MT-B1
$\sigma * BR(Z^0\gamma)_{GEN}$
$\sigma * BR(Z^0\gamma)_{GEN}$ (pb)
25
20
15
$\Delta R_{l\gamma} > 0.3$
$P_T^{\gamma} > 1.0$ GeV/c
DO-2
EHLQ-1
DFLM-AVG
DFLM-160
DFLM-200
DFLM-300
MRS-E
MRS-B
HMRSB
KMRS-B0
MRS-S0
MT-B2
MT-B1

Fig 19a

Electron $W^{\pm}\gamma$

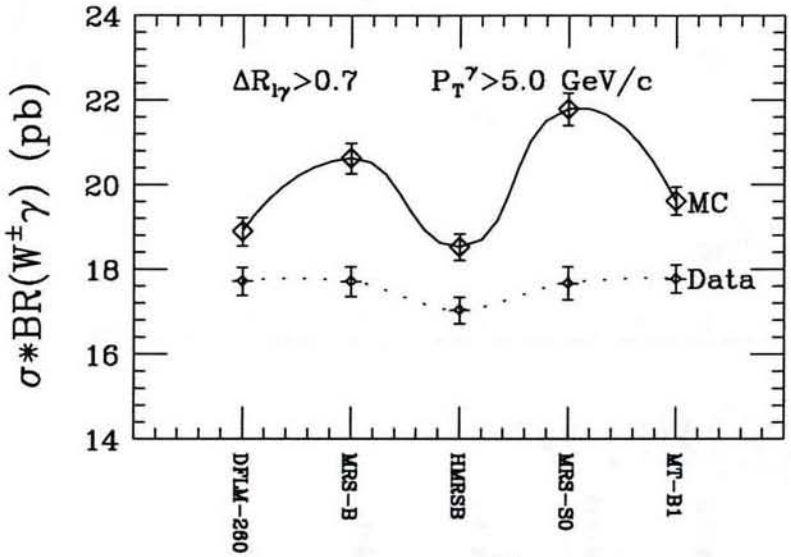

Muon $W^{\pm}\gamma$

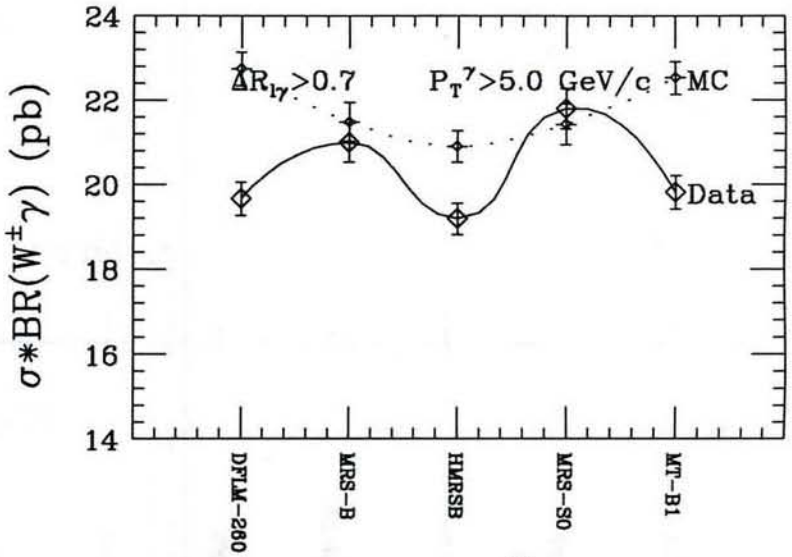

Electron $Z^0\gamma$

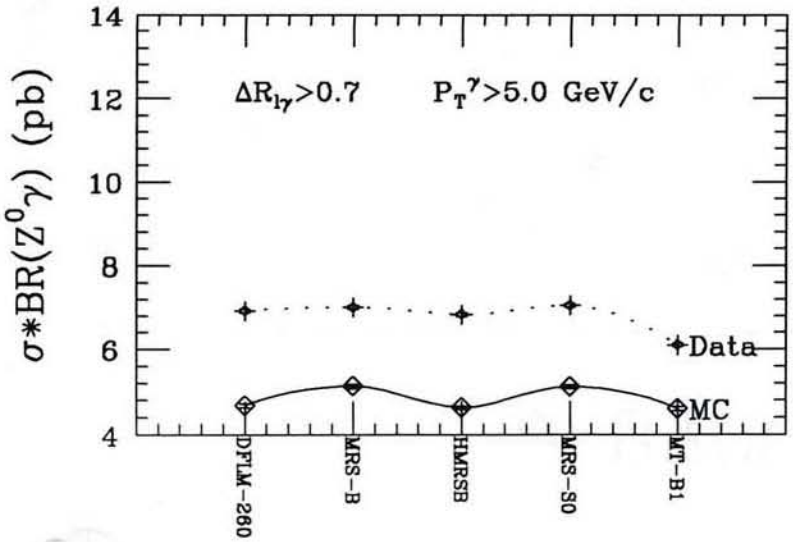

Muon $Z^0\gamma$

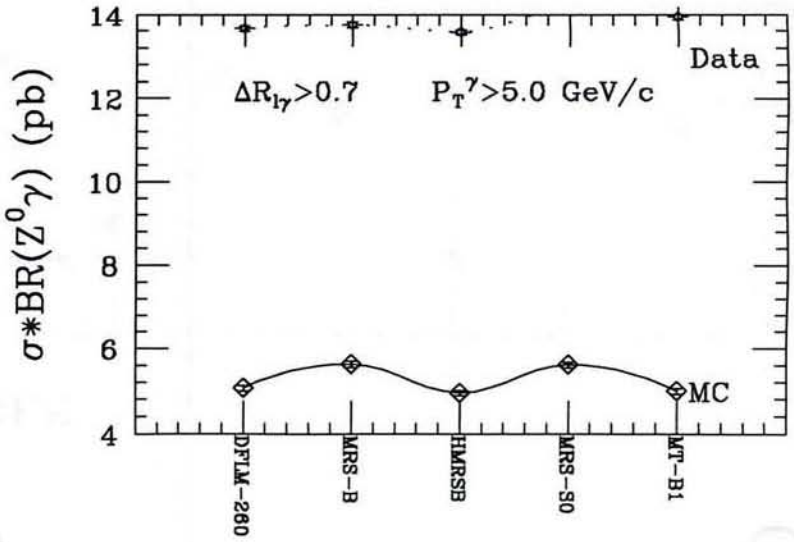

Fig

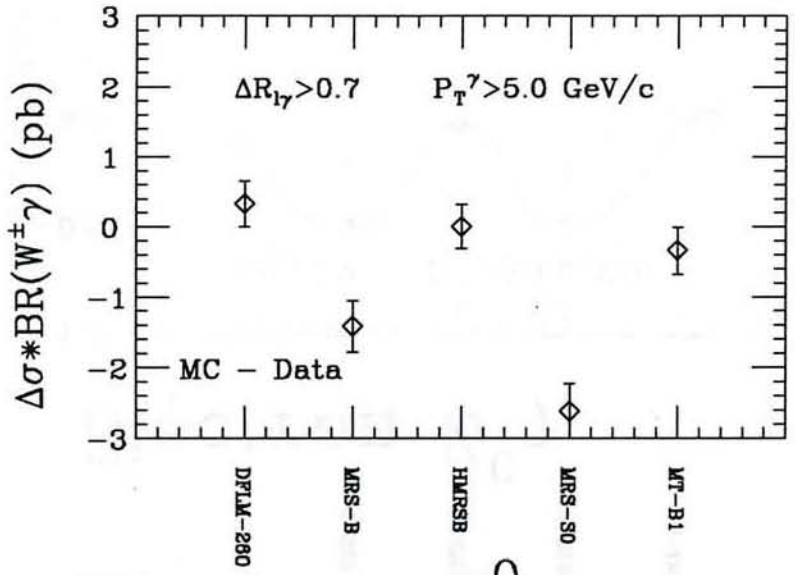
Electron $W^{\pm}\gamma$
$\Delta\sigma*BR(W^{\pm}\gamma)$ (pb)
$\Delta R_{l\gamma}>0.7$
$P_T^{\gamma}>5.0$ GeV/c
MC − Data
DFLM-260
MRS-B
HMRSB
MRS-S0
MT-B1

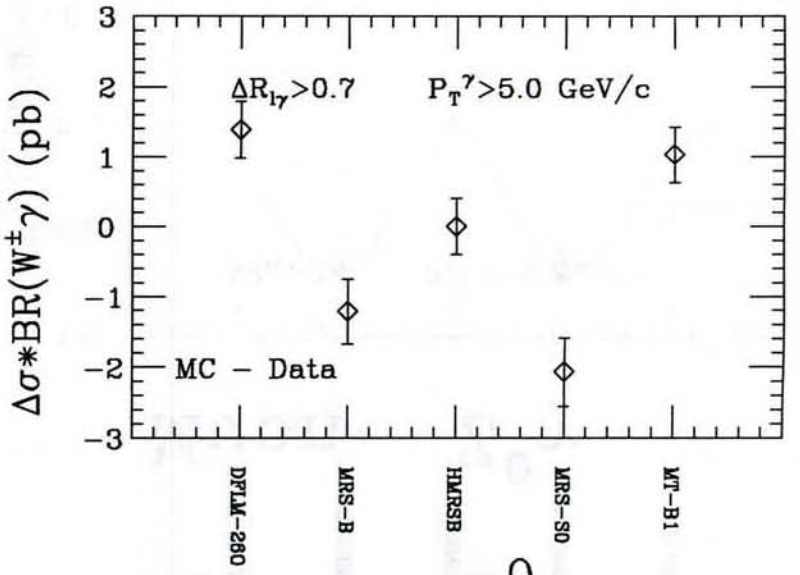
Muon $W^{\pm}\gamma$
$\Delta\sigma*BR(W^{\pm}\gamma)$ (pb)
$\Delta R_{l\gamma}>0.7$
$P_T^{\gamma}>5.0$ GeV/c
MC − Data
DFLM-260
MRS-B
HMRSB
MRS-S0
MT-B1

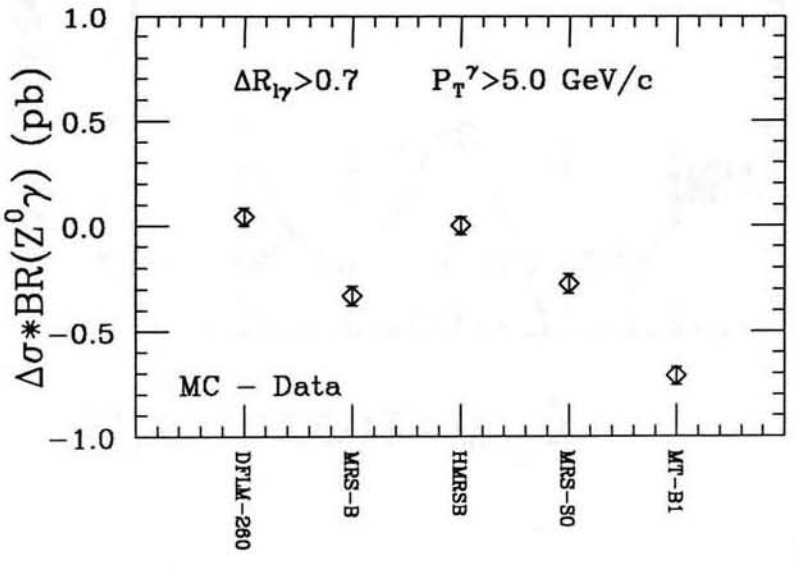
Electron $Z^0\gamma$
$\Delta\sigma*BR(Z^0\gamma)$ (pb)
$\Delta R_{l\gamma}>0.7$
$P_T^{\gamma}>5.0$ GeV/c
MC − Data
DFLM-260
MRS-B
HMRSB
MRS-S0
MT-B1

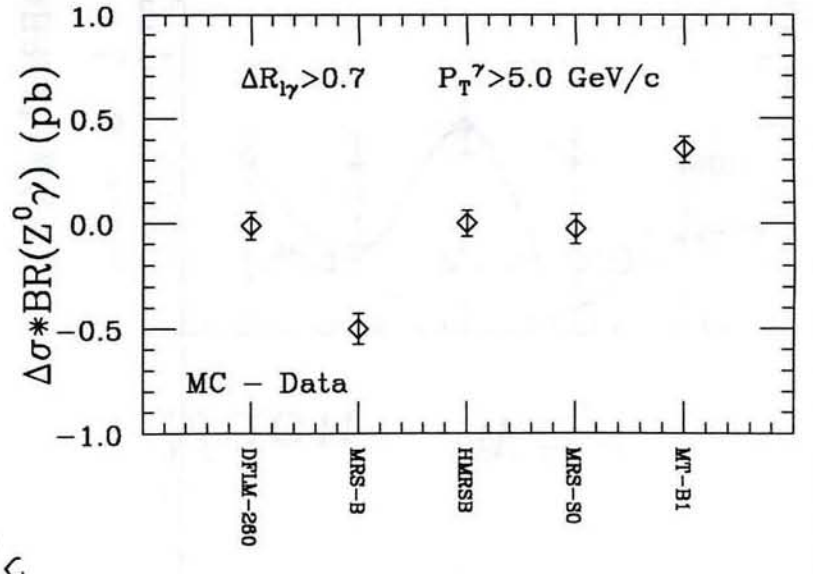
Muon $Z^0\gamma$
$\Delta\sigma*BR(Z^0\gamma)$ (pb)
$\Delta R_{l\gamma}>0.7$
$P_T^{\gamma}>5.0$ GeV/c
MC − Data
DFLM-260
MRS-B
HMRSB
MRS-S0
MT-B1

Fig 19c

Electron $W^{\pm}\gamma$

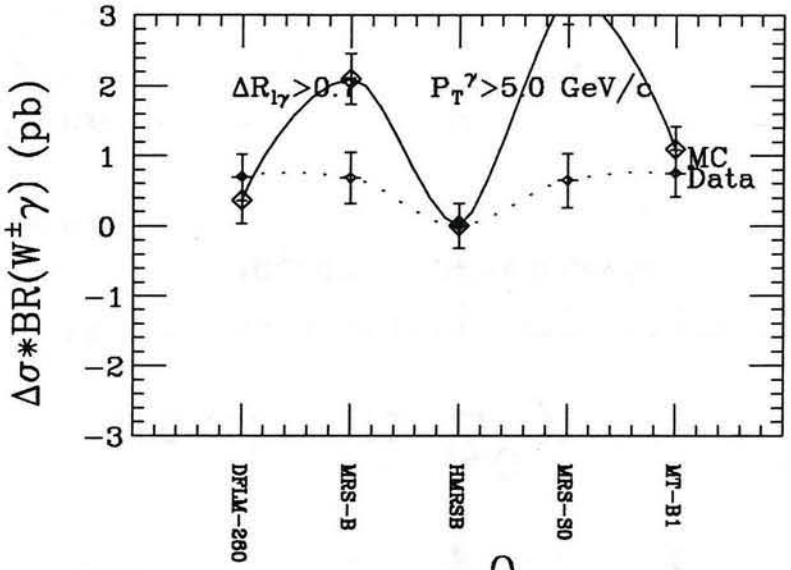

Muon $W^{\pm}\gamma$

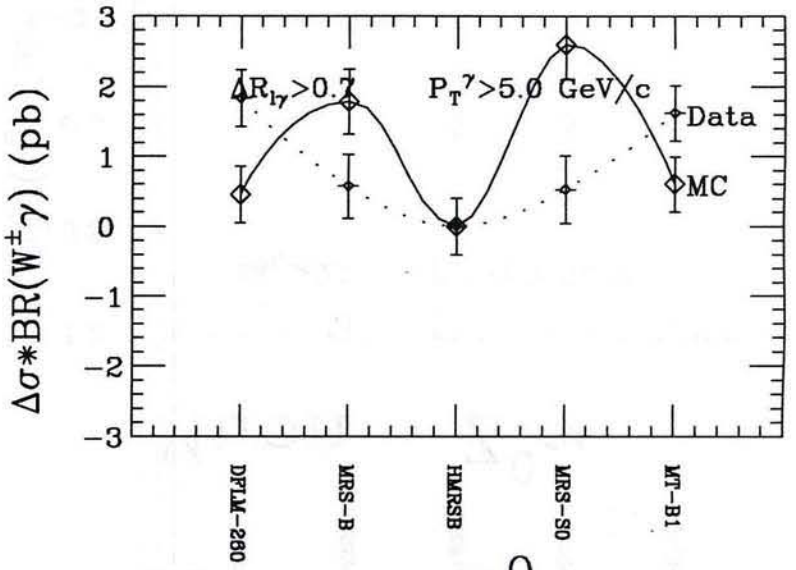

Electron $Z^0\gamma$

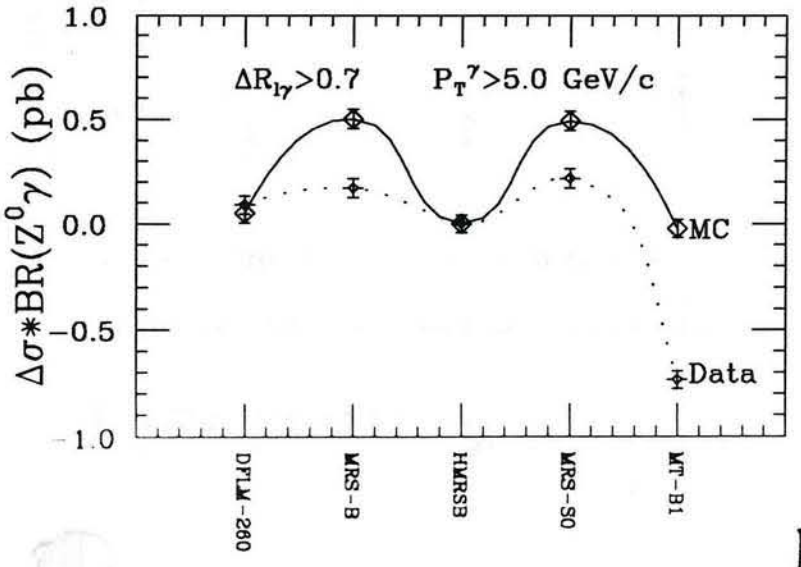

Muon $Z^0\gamma$

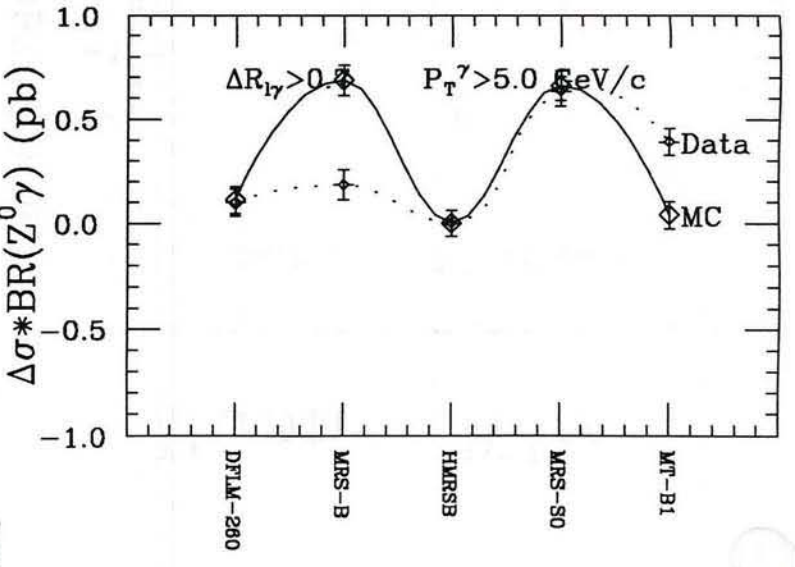

Figure

W/Z Cross Section Ratios

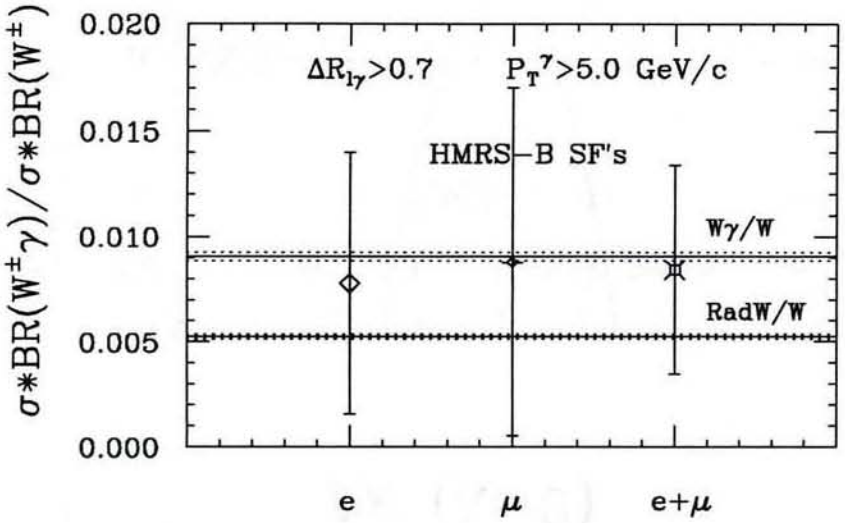

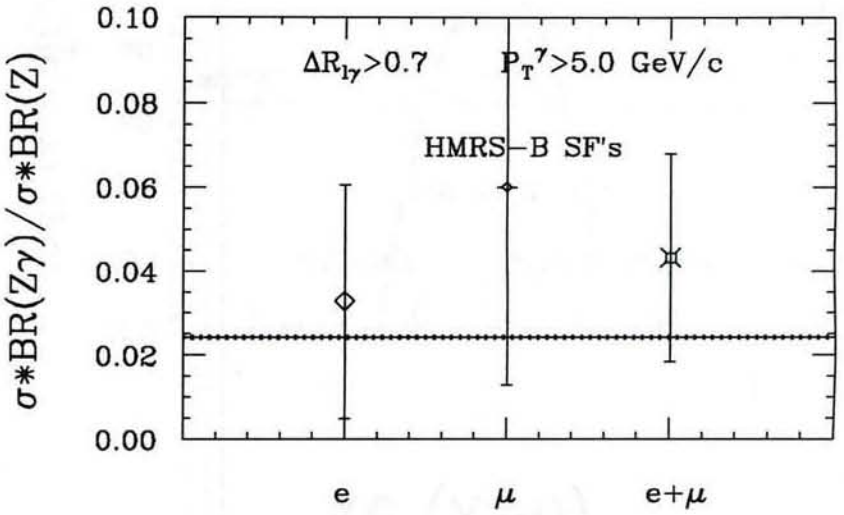

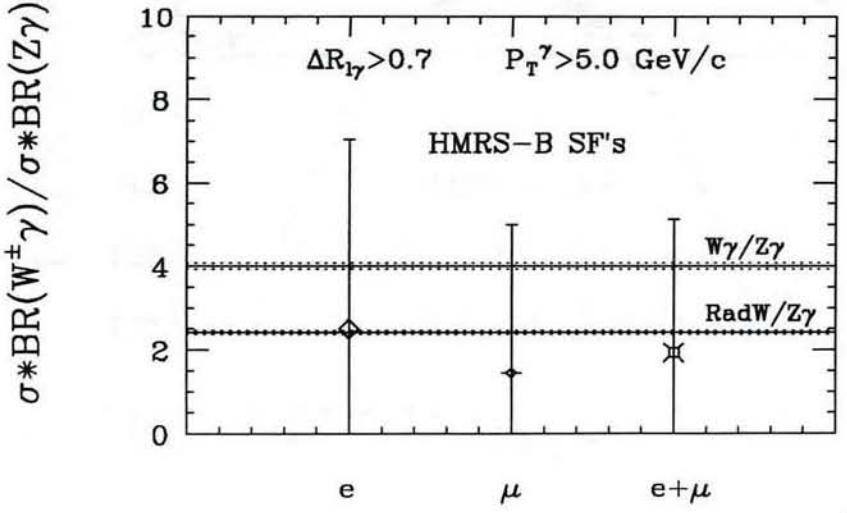

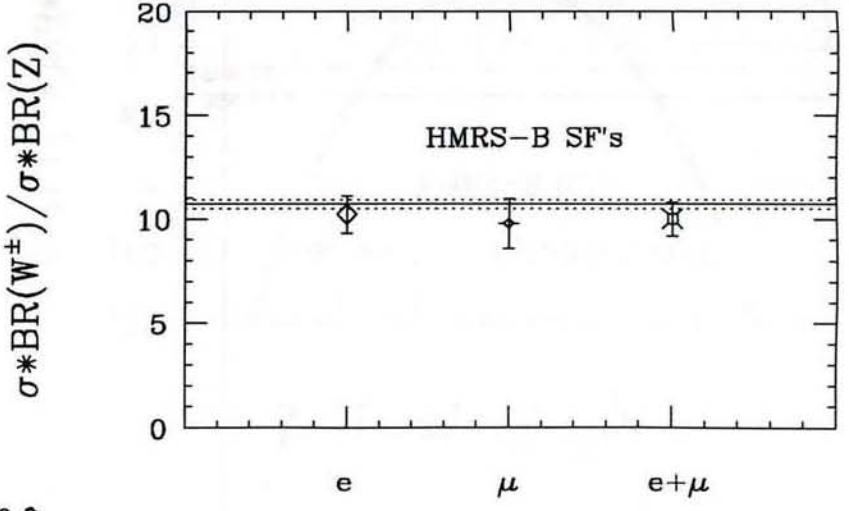

Fig 20

Electron $W^{\pm}\gamma$

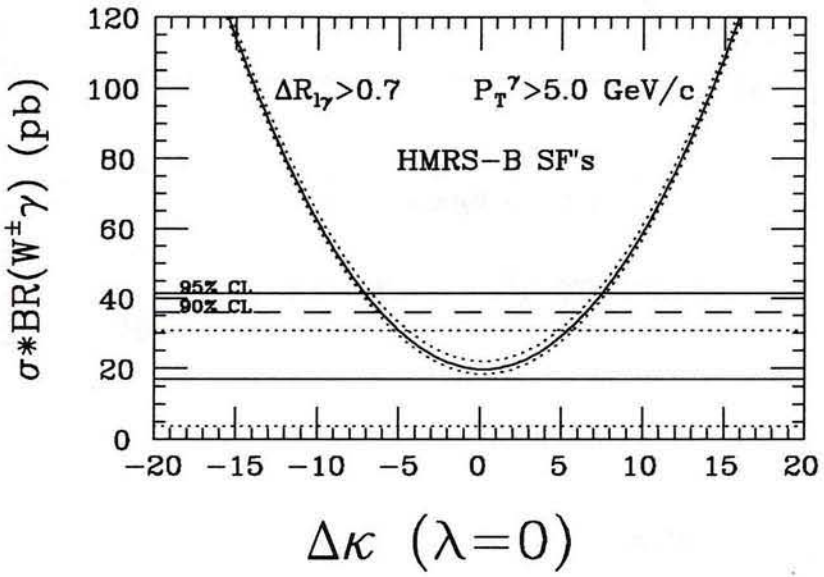

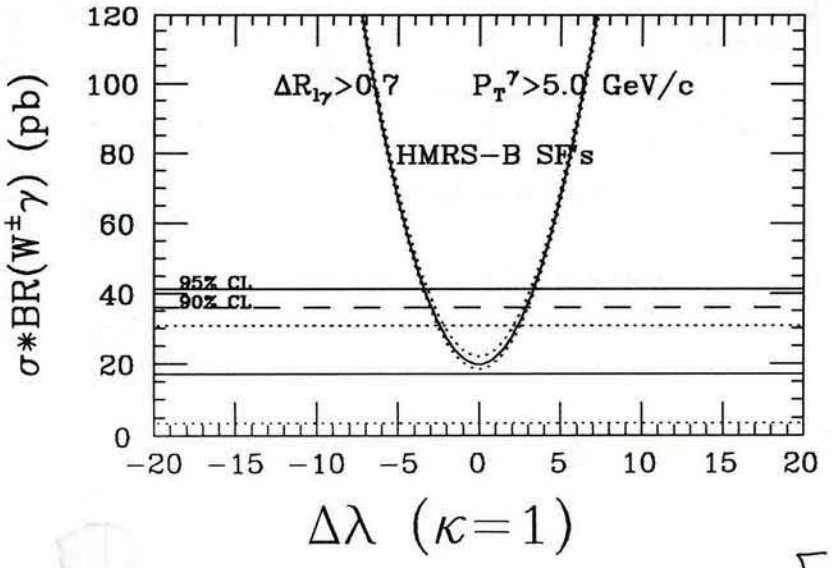

Muon $W^{\pm}\gamma$

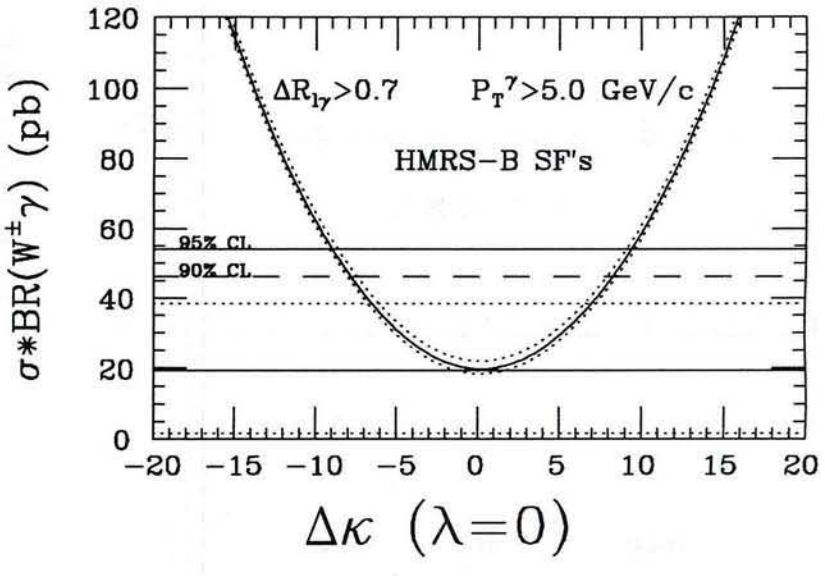

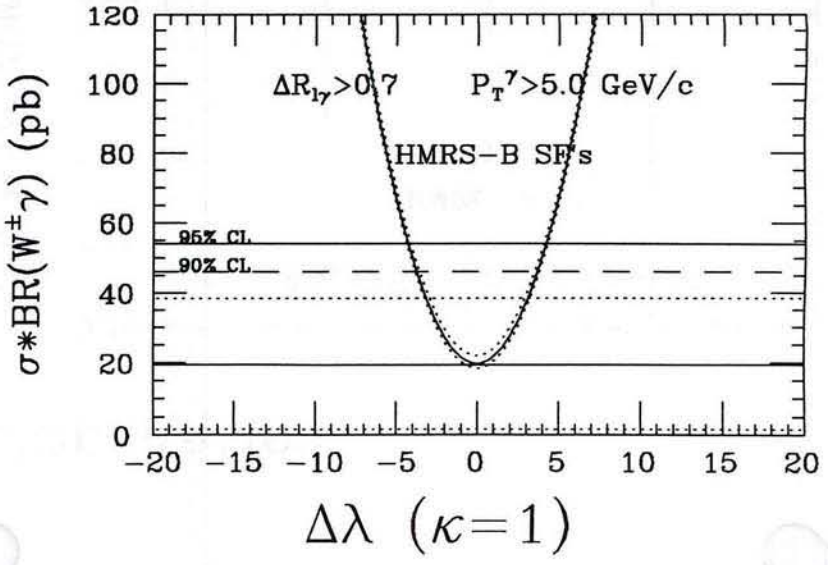

Fig 2

Combined e+μ $W^{\pm}\gamma$

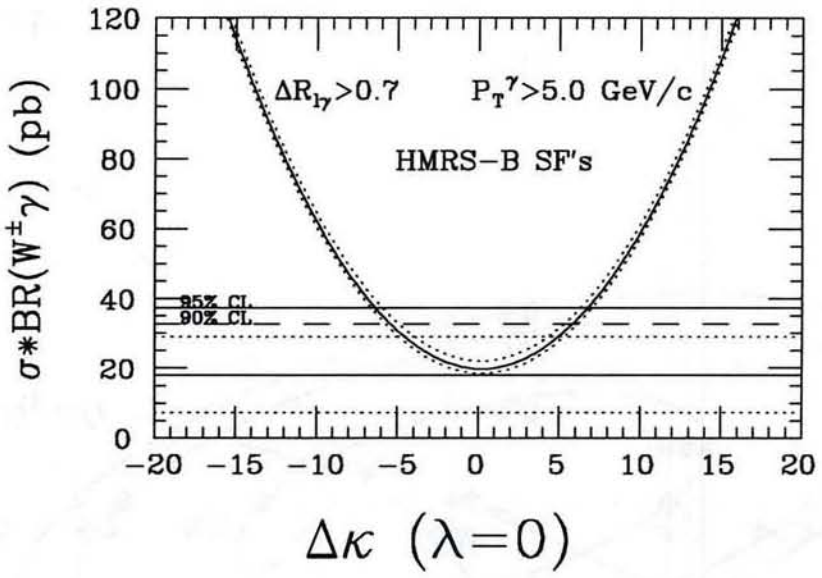

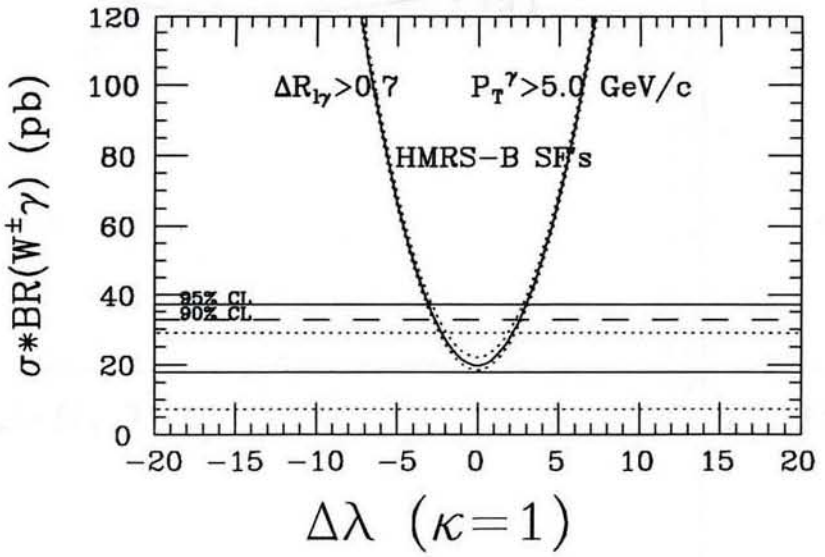

Fig 21b

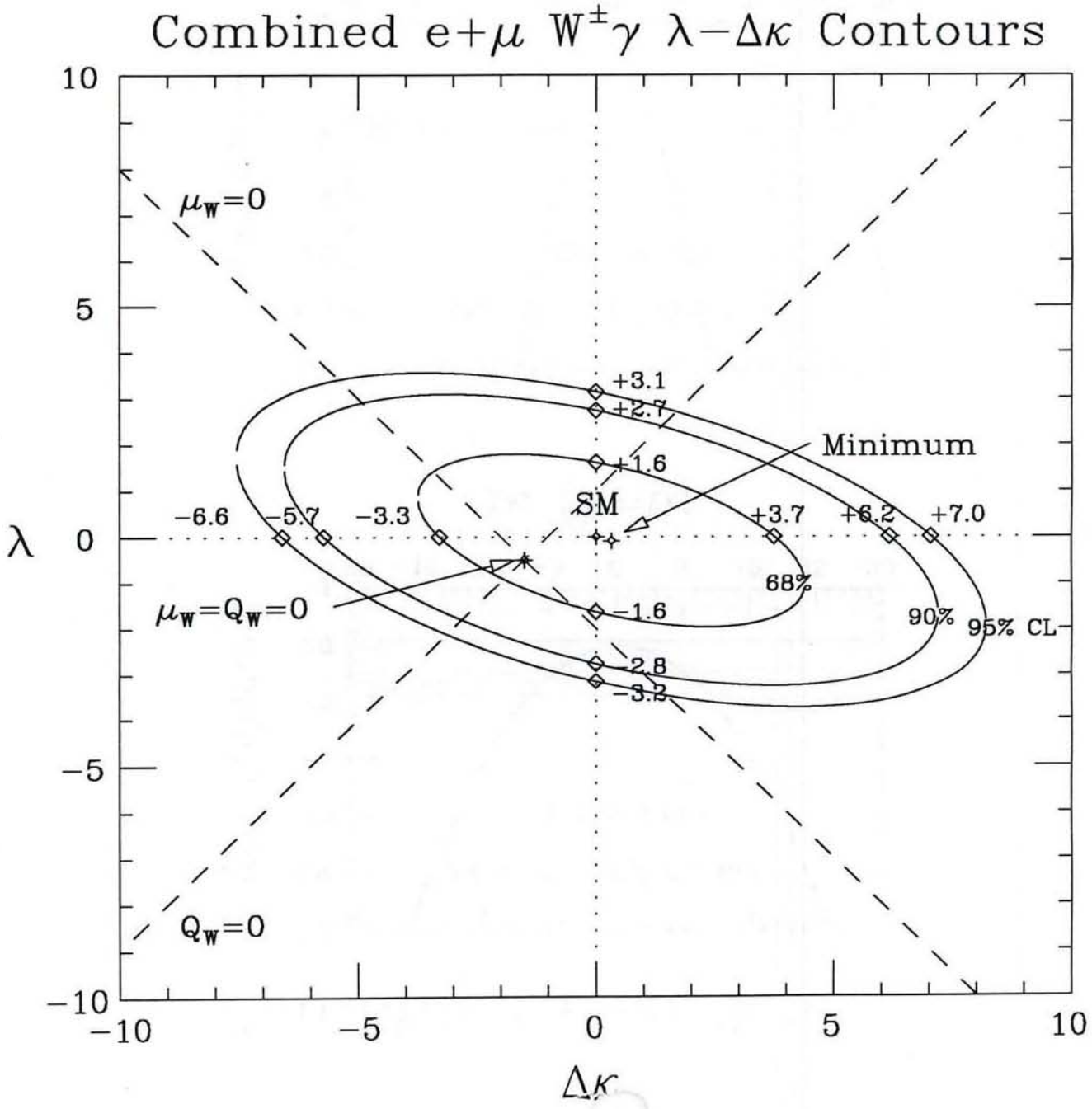
Combined e+μ W±γ λ−Δκ Contours
10
5
0
−5
−10
λ
−10
−5
0
5
10
Δκ
μW=0
QW=0
μW=QW=0
SM
Minimum
+3.1
+2.7
+1.6
−1.6
−2.8
−3.2
−6.6
−5.7
−3.3
+3.7
+6.2
+7.0
68%
90%
95% CL

FIG 2

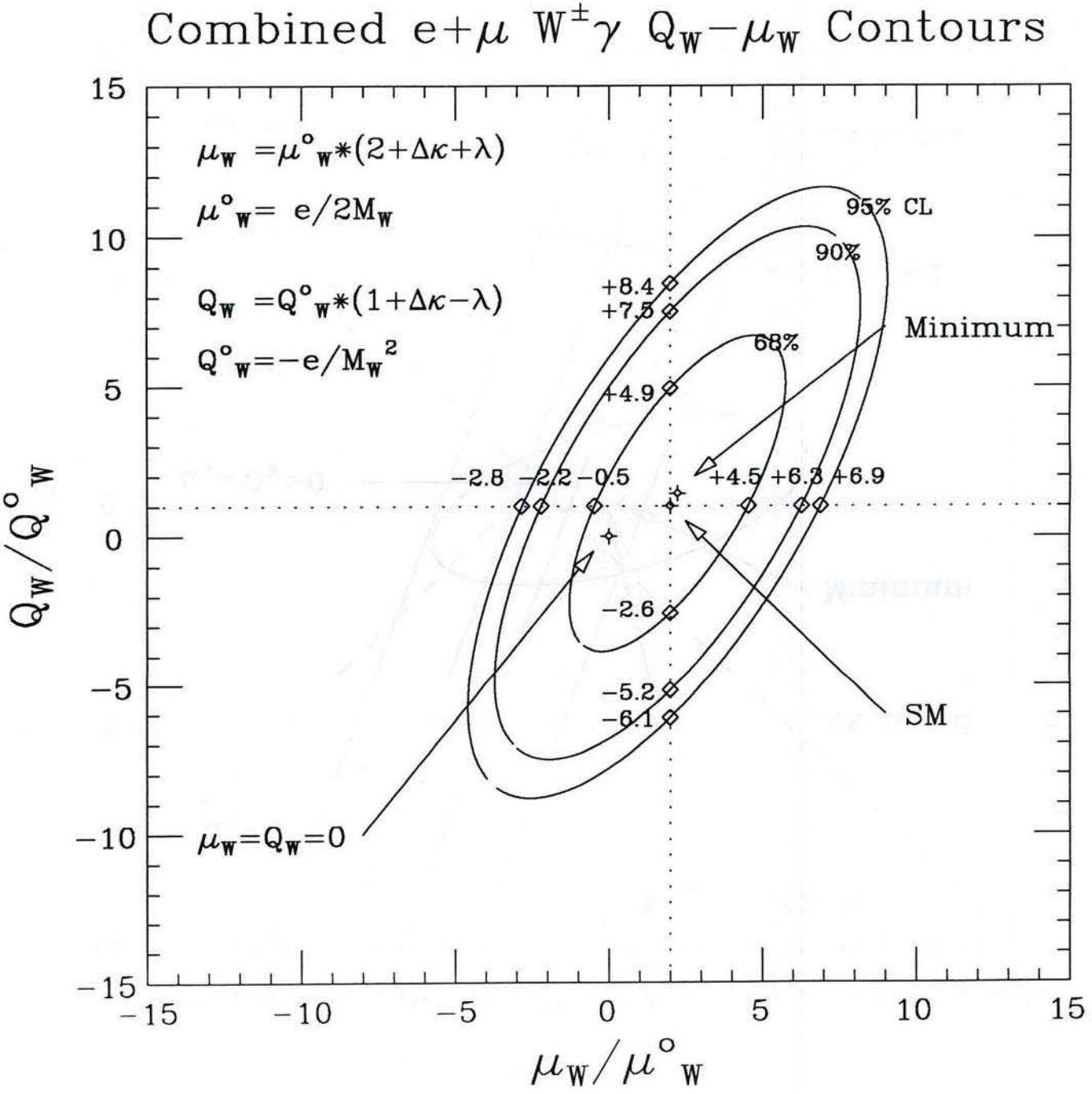
Combined e+μ W±γ Q_W−μ_W Contours
μ_W =μ°_W*(2+Δκ+λ)
μ°_W= e/2M_W
Q_W =Q°_W*(1+Δκ−λ)
Q°_W=−e/M_W²
95% CL
90%
68%
Minimum
SM
+8.4
+7.5
+4.9
−2.8
−2.2
−0.5
+4.5
+6.3
+6.9
−2.6
−5.2
−6.1
μ_W=Q_W=0
15
10
5
0
−5
−10
−15
−15
−10
−5
0
5
10
15
Q_W/Q°_W
μ_W/μ°_W

FIG 23

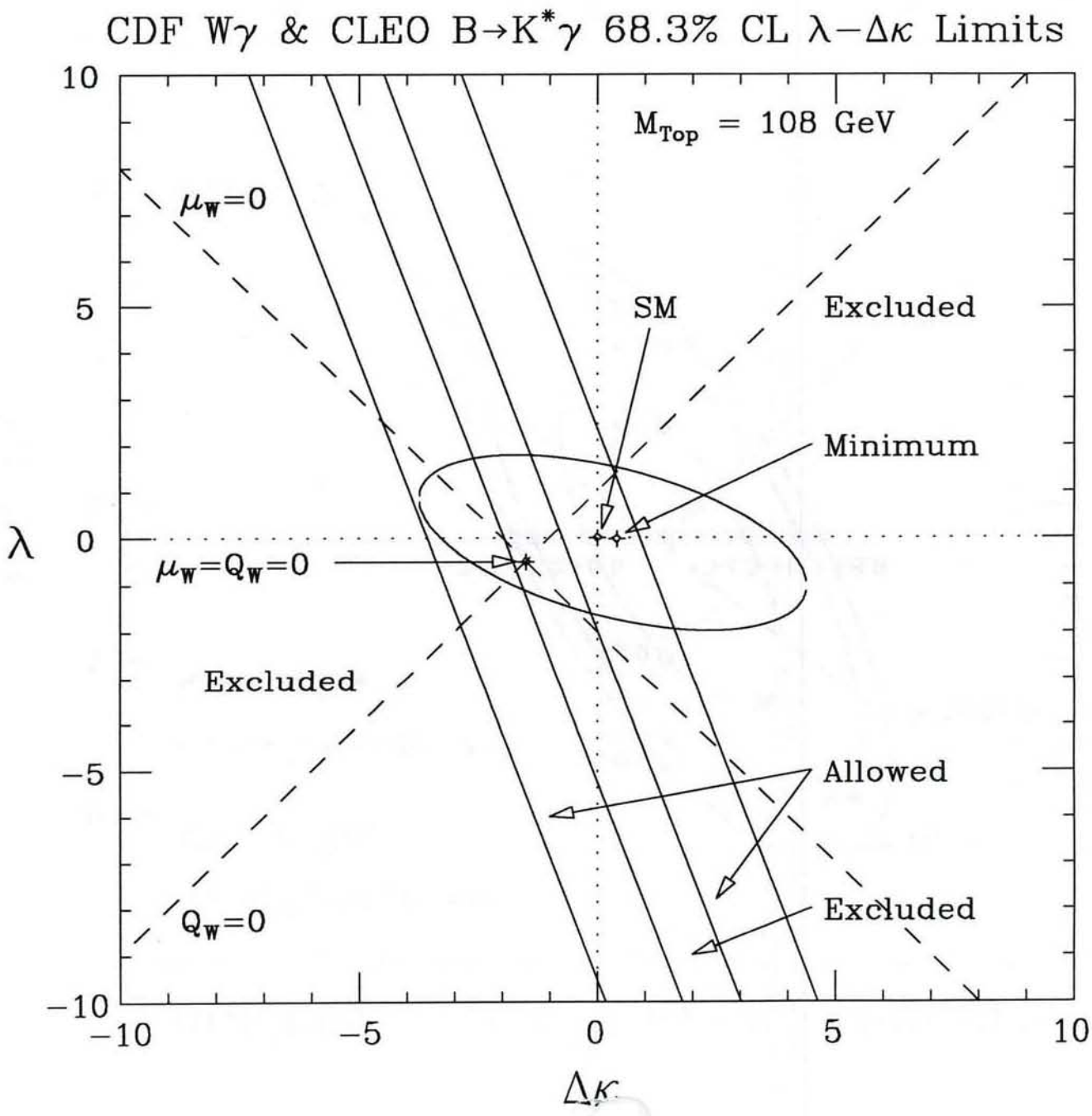
CDF Wγ & CLEO B→K*γ 68.3% CL λ−Δκ Limits
M_Top = 108 GeV
μ_W=0
SM
Excluded
Minimum
λ
μ_W=Q_W=0
Excluded
Allowed
Excluded
Q_W=0
10
5
0
−5
−10
−10
−5
0
5
10
Δκ

Fig 2

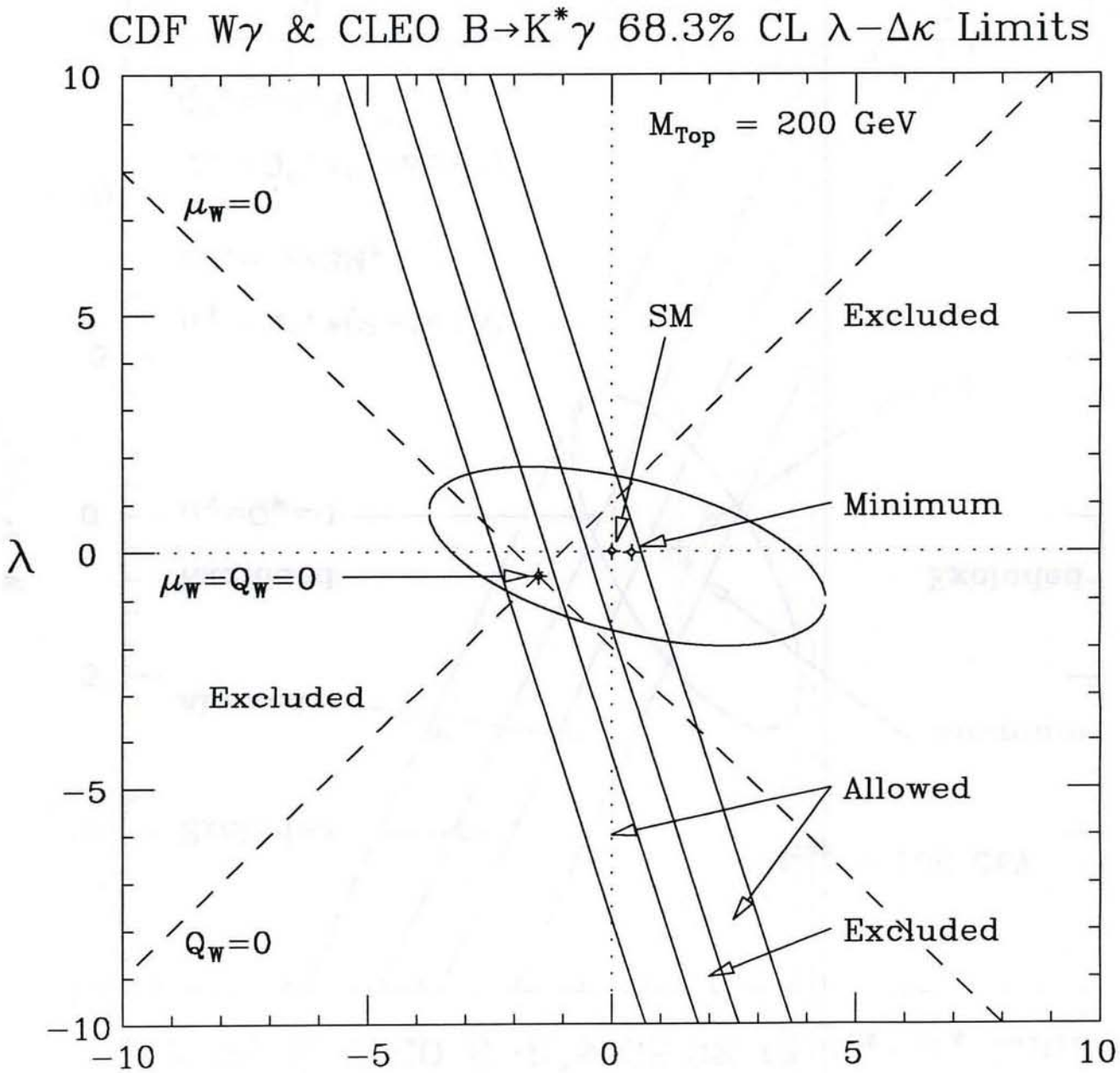
CDF Wγ & CLEO B→K*γ 68.3% CL λ−Δκ Limits
M_Top = 200 GeV
μ_W=0
SM
Excluded
Minimum
μ_W=Q_W=0
Excluded
Allowed
Excluded
Q_W=0
λ
Δκ
10
5
0
−5
−10
−10
−5
0
5
10

Fig 246

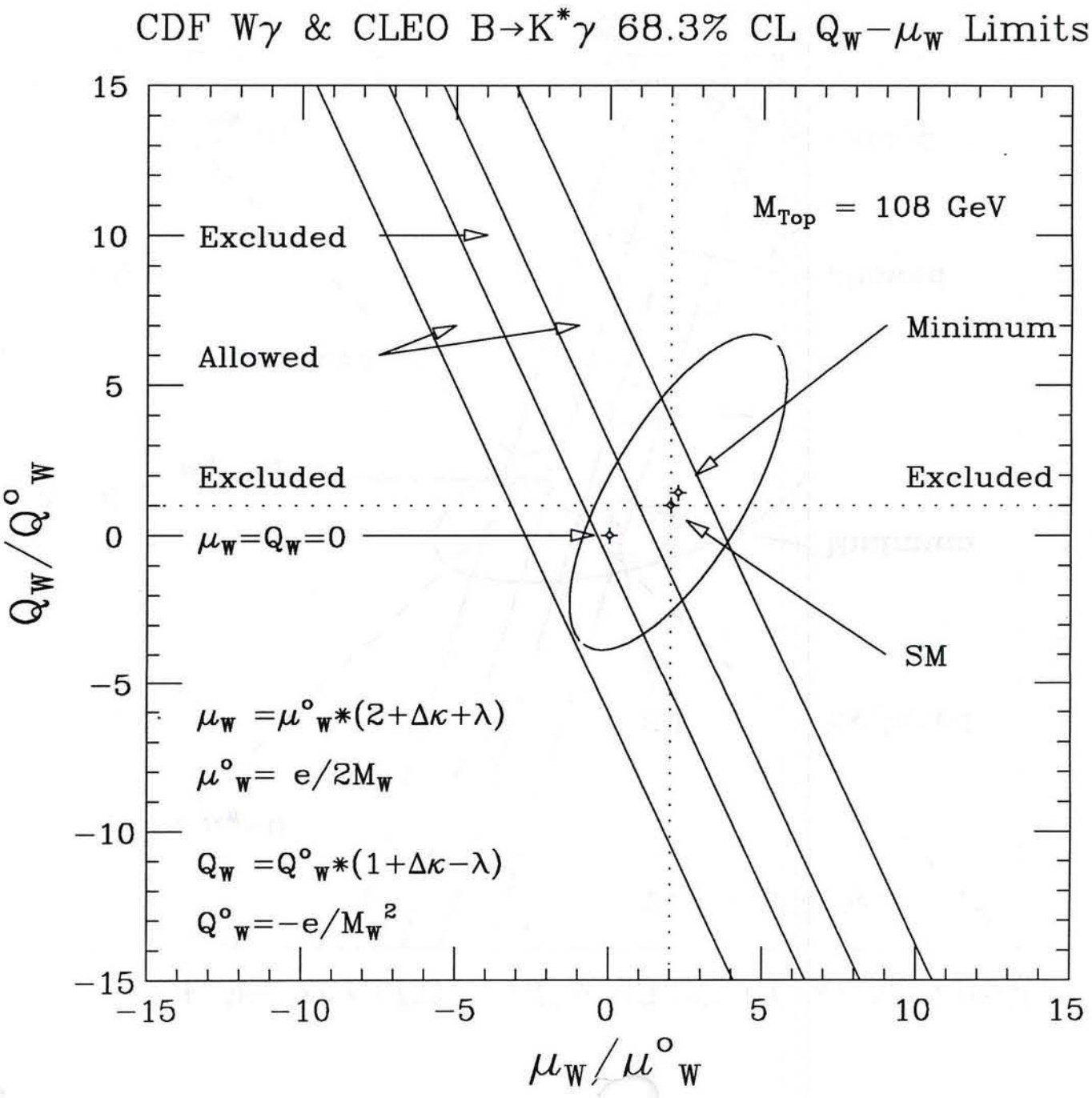
CDF Wγ & CLEO B→K*γ 68.3% CL Q_W−μ_W Limits
M_Top = 108 GeV
Excluded
Allowed
Excluded
μ_W=Q_W=0
Minimum
Excluded
SM
μ_W =μ°_W*(2+Δκ+λ)
μ°_W= e/2M_W
Q_W =Q°_W*(1+Δκ−λ)
Q°_W=−e/M_W²
Q_W/Q°_W
μ_W/μ°_W
15
10
5
0
−5
−10
−15
−15
−10
−5
0
5
10
15

Fig 25a

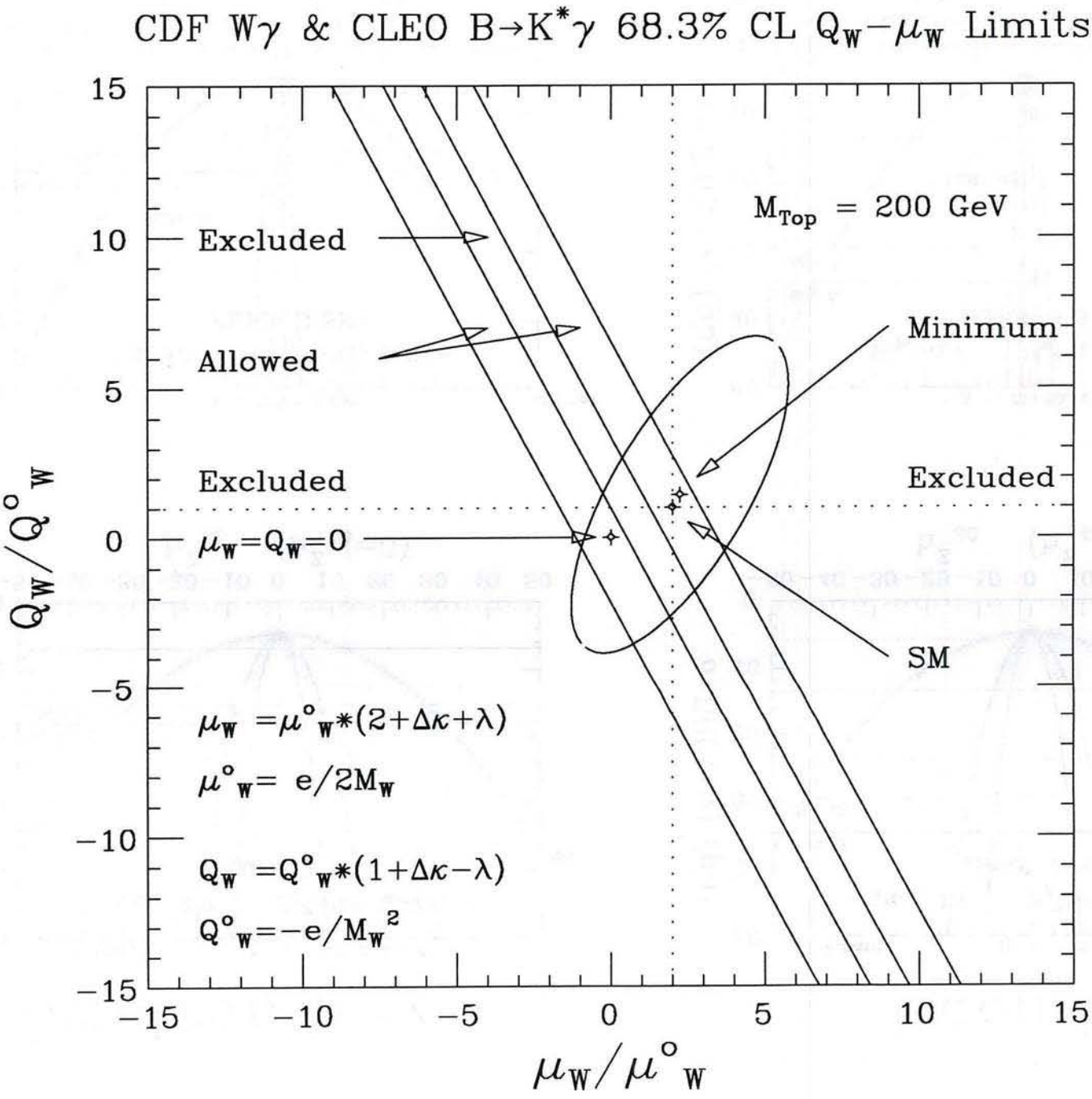
CDF Wγ & CLEO B→K*γ 68.3% CL $Q_W-\mu_W$ Limits
M_{Top} = 200 GeV
Excluded
Allowed
Excluded
Minimum
Excluded
SM
$\mu_W=Q_W=0$
$\mu_W = \mu^\circ_W*(2+\Delta\kappa+\lambda)$
$\mu^\circ_W = e/2M_W$
$Q_W = Q^\circ_W*(1+\Delta\kappa-\lambda)$
$Q^\circ_W = -e/M_W^2$
Q_W/Q°_W
μ_W/μ°_W
15
10
5
0
−5
−10
−15
−15
−10
−5
0
5
10
15

Fig 256

Electron Z+γ

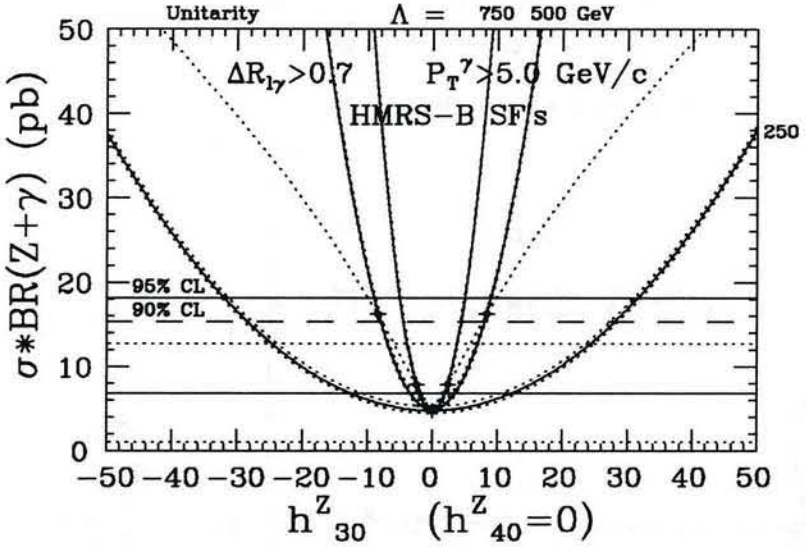

Muon Z+γ

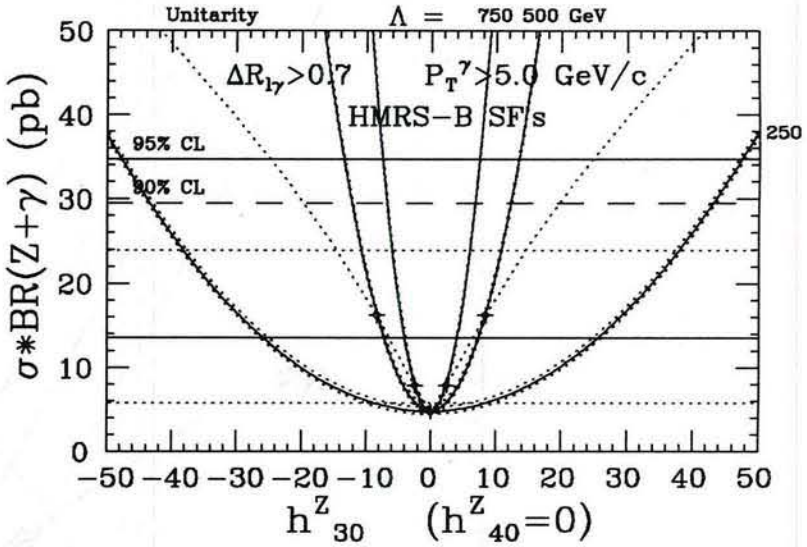

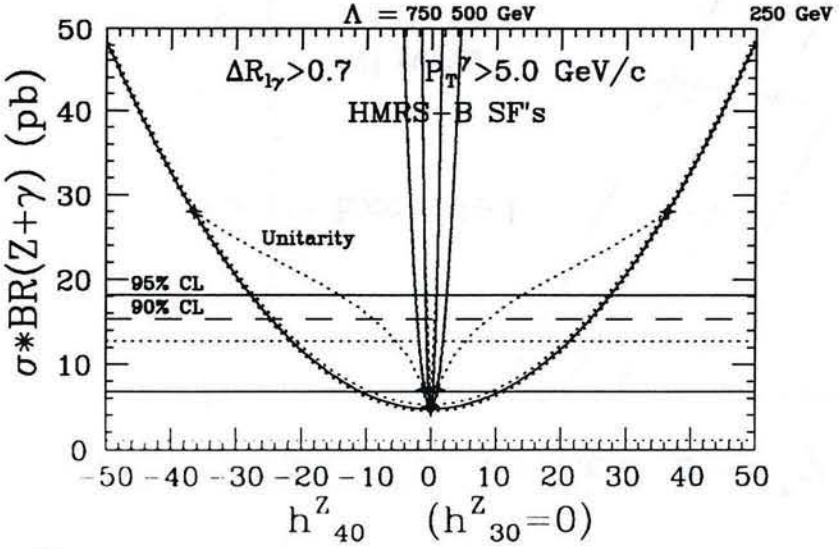

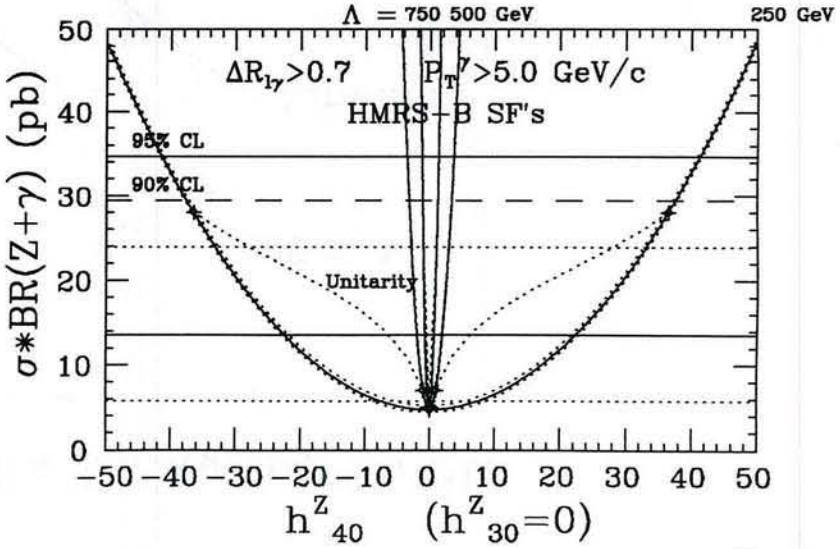

Fig a

Combined e+μ Z+γ

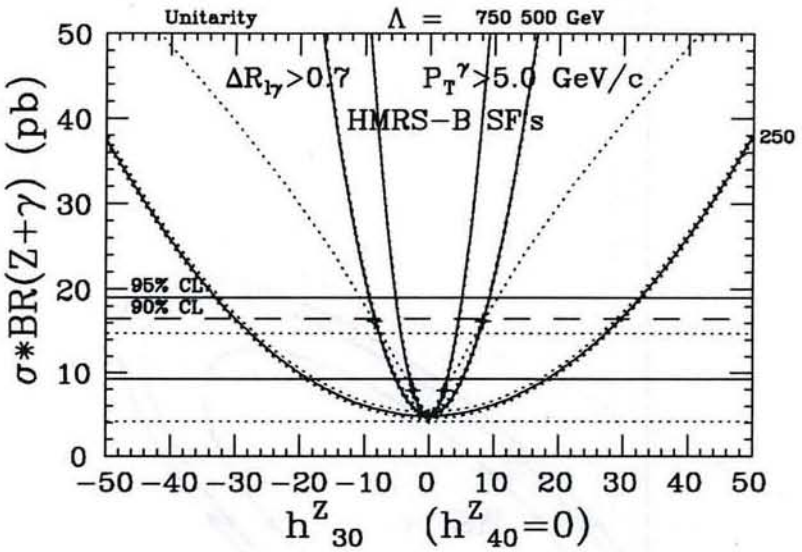

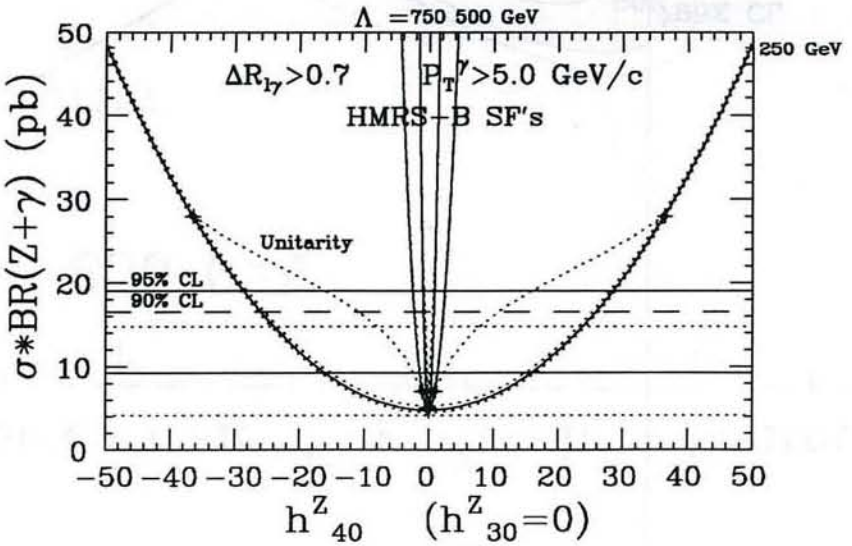

Fig 26b

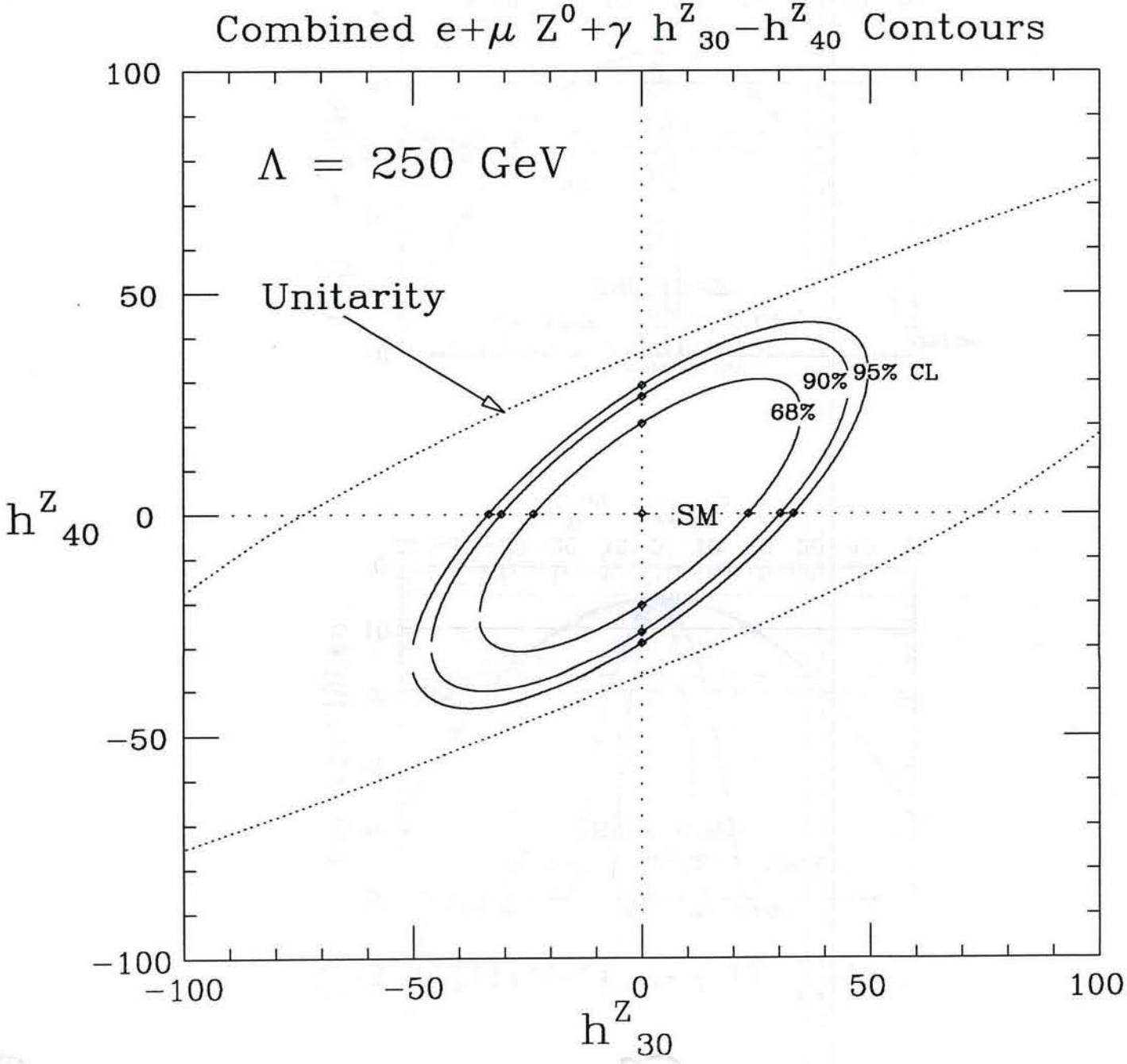
Combined e+μ Z⁰+γ h^Z_30−h^Z_40 Contours
Λ = 250 GeV
Unitarity
90%
95% CL
68%
SM
100
50
0
−50
−100
−100
−50
0
50
100
h^Z_40
h^Z_30

Fig. 7a

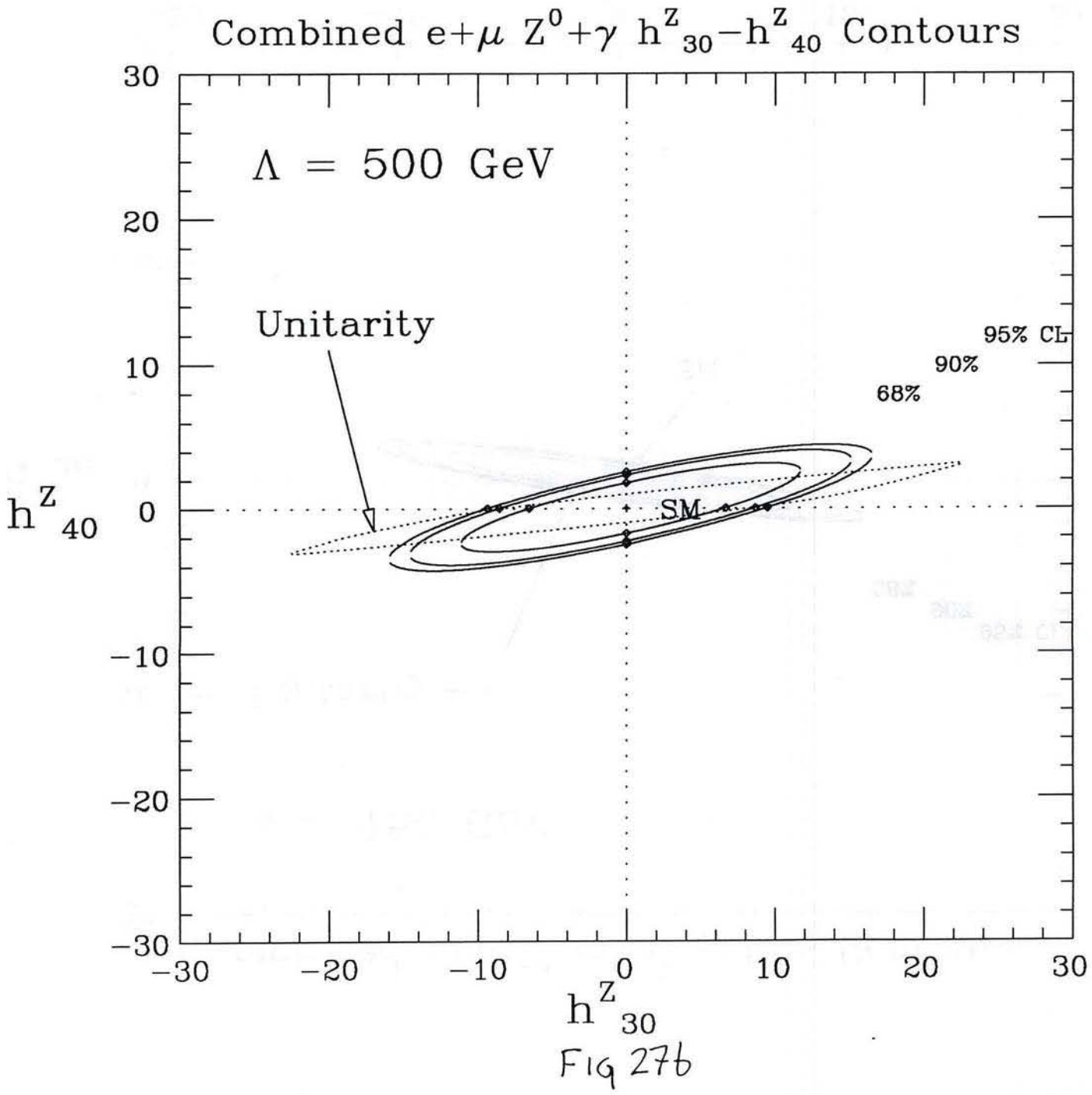
Combined e+μ Z⁰+γ h^Z_30−h^Z_40 Contours
Λ = 500 GeV
Unitarity
95% CL
90%
68%
SM
h^Z_40
h^Z_30
30
20
10
0
−10
−20
−30
−30
−20
−10
0
10
20
30

Fig 27b

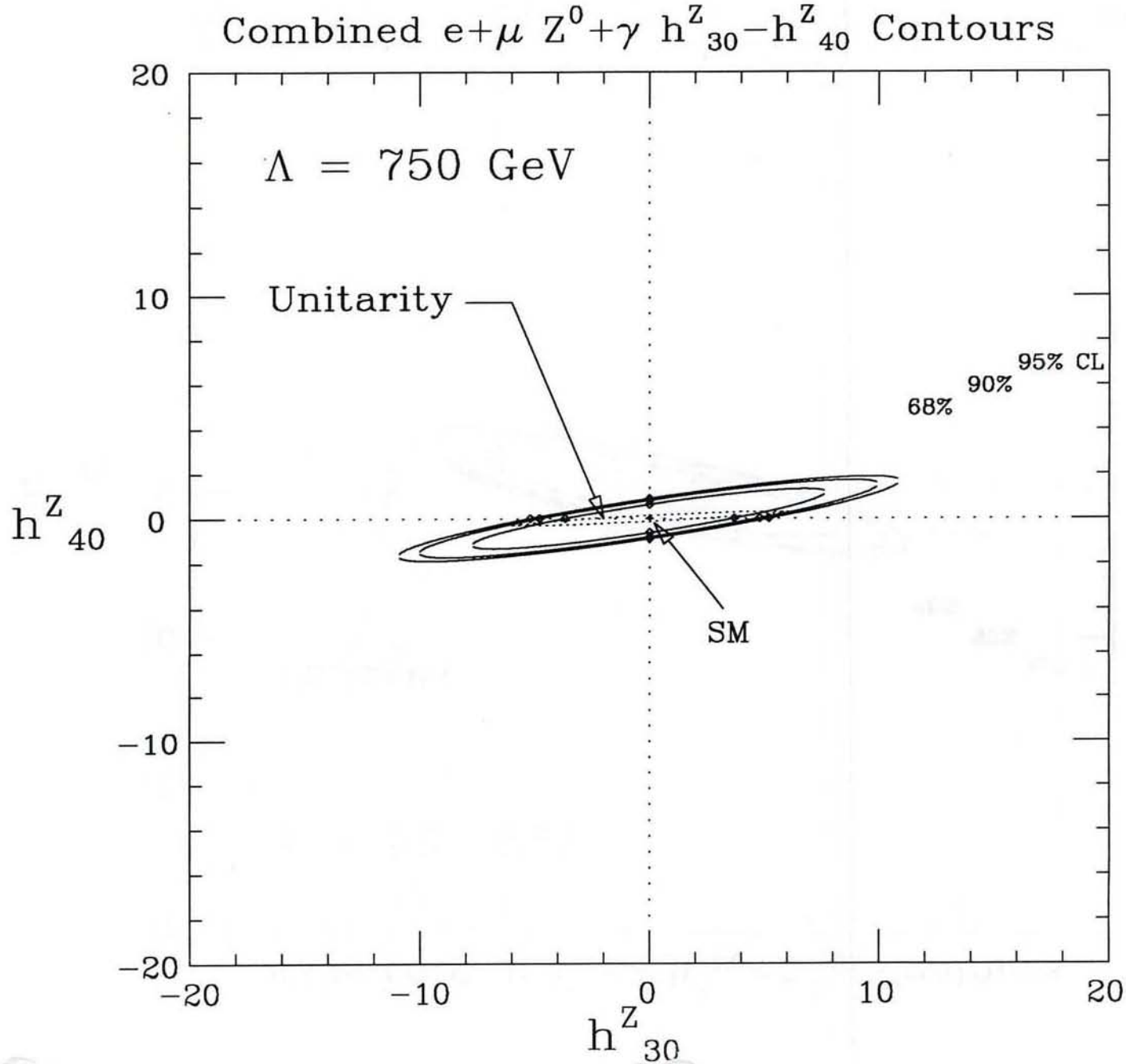
Combined e+μ Z⁰+γ h^Z_30−h^Z_40 Contours
Λ = 750 GeV
Unitarity
95% CL
90%
68%
SM
h^Z_40
h^Z_30
20
10
0
−10
−20
−20
−10
0
10
20

Fig 2.c